POLITECNICO
MILANO 1863

Department of mechanical engineering

Doctoral programme in mechanical engineering

Development of tools and systems for the protection of workers from foot-transmitted whole-body vibration

Doctoral dissertation of:
Pietro Marzaroli

Supervisor: ***Prof. Marco Tarabini***

Tutor: ***Prof. Federico Cheli***

The chair of the doctoral program: ***Prof. Daniele Rocchi***

2019 – PhD. Cycle XXXII

Abstract

Several workers are exposed to mechanical vibration and the harmful effect of the exposure is well documented in literature. The induced vibrations to the extremities of the limbs may cause neurovascular problems, namely, Raynaud syndrome, even resulting in disabilities. These problems have been linked to higher frequencies than the ones affecting the human body as a whole. Therefore, the first part of this dissertation describes the mechanical design and development of the actuators system able to generate the triaxial vibration needed to characterize the response of the standing human subject from 1 to 80 Hz. The machine is based on the architecture of the linear delta robot with vertical actuators. Once the machine was optimized for the defining dimensions, the appropriate actuators were selected, and custom components were drawn to be produced. The tests done on the machine after its realization confirm that it can generate pseudo-random noise up to 80 Hz across the three mutually perpendicular spatial axes simultaneously. The average root-mean squared error between the modulus of the spectrum of generated signal and the signal measured directly on the platform is 6,9 mm/s^2 across the three axes, and it is 5,5 mm/s^2 when a person is standing on the platform, i.e. lower than 1% of the imposed acceleration. A generalized mathematic method to directly link the design parameters of a linear delta robot with its kinematic performances was developed.

The second part of this dissertation describes the development of a planar lumped parameters mechanical model of the foot-ankle system. Given that the data regarding the response of the human foot to multiaxial vibration are not available yet, the model was validated with the objective of reproducing the transmissibility of vertical vibration from the ground to five different positions on the foot. The model also reproduced the apparent mass of a standing person subjected to vertical whole-body vibrations. Results evidenced that the model reproduces the transmissibility with errors that are small in comparison with the inter- and intra-subject variability.

Keywords: Whole Body Vibration, Foot-Transmitted Vibration, Parallel Robot, Mathematical Lumped Parameter Model

INDEX

FIGURE INDEX

TABLE INDEX

Chapter I

1 Introduction

Mechanical vibration is a physical phenomenon to which the human body is often subjected. The adverse effects of vibrations on workers have been largely documented in the literature, although some studies suggest that the controlled exposure to mechanical stimuli may have beneficial effects on the health, like improving physical performance of both athletes [1], [2] and of people unfit for regular physical activity [3]-[5]. This topic however is still under discussion. In fact, the effects presented are temporary, and other studies show that it does not have effect on the actual athletic performance [6], but it does increase the muscle fatigue [7]. This chapter focuses on describing the problems that may arise from vibration exposure and the techniques used to prevent or reduce the risk of developing them.

1.1 Effect of mechanical vibration on the human body

Mechanical vibration leads to occupational hazards in different work sectors. The effect that this risk factor has on the human body is dependent upon the body part that is directly interacting with the vibration. Human vibration is usually classified into three main categories. Whole-body vibration (WBV), which can be identified when the worker is sitting on a vibrating seat, has been classically studied for drivers and pilots. Bovenzi et al. conducted a systematic research that suggested that up to 7% of all workers in Europe, United States, and Canada are regularly exposed to WBV [8]. However, there are also situations in which the vibration is entering the body through the hands, and it is mostly related to the use of hand-held power tools. This condition is called hand-arm vibration (HAV). Additionally, there are other situations in which vibration is transmitted through the foot, and it is most common for workers standing on heavy machinery. This condition takes the name of foot-transmitted vibration (FTV). ISO 2631-1:1997 [9] contains the guidelines for computing the vibration exposure for WBV and FTV: the danger for the worker is quantified starting from the three components of the acceleration vector measured at the interface between the vibrating surface and the human body. Acceleration signals are then filtered through proper frequency weighting curves, which are different in accordance with the direction and position of the human body (standing, seated or recumbent). The acceleration level is obtained by computing the RMS of the filtered signals and choosing the worst axis or the vector sum of the three mutually perpendicular components. The vibration exposure is computed by combining the vibration level and the time of exposure; the

resulting value is then compared to the thresholds, commonly referred to as Exposure Action Value and Exposure Limit Value. Equivalently, the acceleration level can be compared to time-dependent thresholds, as shown in Figure 1.

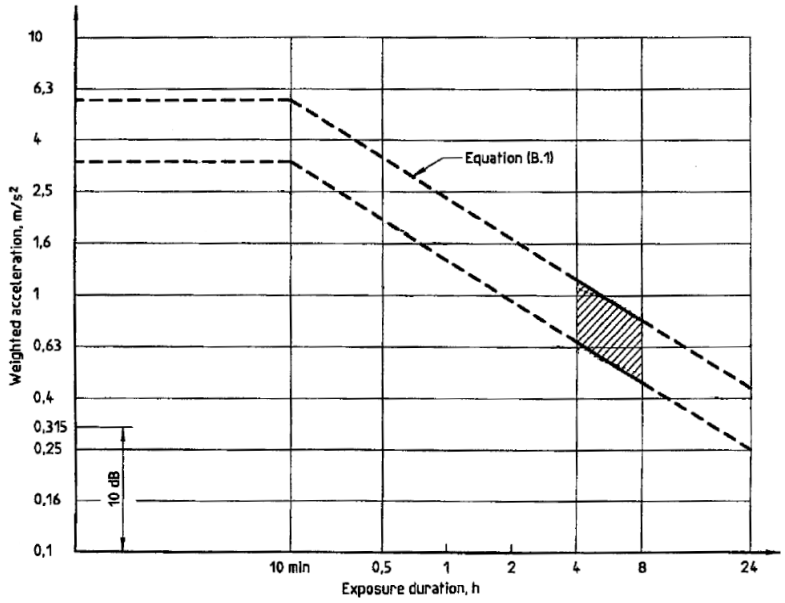

Figure 1: Exposure Action Value and Exposure Limit Value, as a function of duration exposure, as proposed by ISO 2631-1:1997

The standard does not provide limits for vibration exposure, but it is meant to provide a method to quantify and compare the dose of vibration to which workers of different field and conditions are exposed. The Parliament and Commission of the European Community defined the limits in 2002 [10], The results of such directive are shown in the document “minimum health and safety requirements” for the exposure of workers to the risks arising from vibration [11].

1.1.1 Whole Body Vibration

Most literature studies are focused on WBV, as it is the most common and widespread. The negative effects of acute exposure WBV on the workers includes increased heart rate, hyperventilation, headache, loss of balance, motion sickness, muscle fatigue, impaired of speech and vision [12]. Prolonged exposure to WVB is thought to be linked to musculoskeletal disorders. In particular, scientific literature reviews suggest that there is enough evidence to link exposure to WBV and an increased risk of developing low-back pain and sciatica [13], [14]. Extreme cases have been linked to fatigue failures at the endplates of the lumbar vertebrae [15]. Burström et al. [16] conducted a systematic review of the scientific literature concerning the link between whole-body vibration and the risk of low back pain and sciatica. The authors systematically searched in different databases,

obtaining more than 300 articles; more than 20 studies matched the inclusion criteria and were included in the meta-analysis. WBV exposure was associated with increased prevalence of low back pain and sciatica.

Drivers are by far the category more exposed to WBV. Bongers et al. [17] conducted a questionnaire survey on Dutch helicopter pilots, with the objective of linking musculoskeletal diseases to this job. The test group included 133 people, while 228 people composed the control group. It was found that an increased time of daily exposure to vibration was linked to a higher prevalence of transient back pain, while chronic back pain was more linked to a cumulative flight time higher than 2000 h, even though the vibration exposure measured on helicopter seats did not exceed the recommended dose. Lynne et al. [18] measured the vibration exposure on quad bike seats and used the exposure measured to validate a predictive statistical model based on self-reported data. 130 livestock farmers from south New Zealand took part in the study. It was found that the parameters that have the highest influence on the vibration exposure are the age of the subject, the type of the suspensions of the machine and the number of driving hours per day. Young people using quad bikes with rigid axels for a longer time per day were in fact found to be exposed to a dose of vibration higher than the recommended value, thus they are more at risk of developing musculoskeletal diseases. Zeng et al. [19] conducted a similar study, and tried to validate a statistical model that could predict the vibration exposure of Canadian Prairie farmers on the basis of self-reported parameters. 87 measurements were made for the model validation, and it was found a median vibration exposure of 0,72 m/s^2, which is above the Exposure Limit Value for a work shift with a duration of 8 h. In fact, more than 79% of the participants reported discomfort while driving. The predictors that were found to be the most relevant are linked to the characteristics of the machine (production year, horsepower, transmission) or to the discomfort experienced while driving (jerk/jolt frequency and seat bottom-out frequency). Bibhuti et al. [20] conducted a questionnaire study on drivers of heavy-machinery working in an open-pit mine in western India. 46 employees with more than five years of occupational exposure to WBV were randomly selected to participate at the study and 20 workers from the same mine, but not subjected to occupational WBV were selected as the control group. The questionnaire showed that low-back pain was the musculoskeletal disorder with the highest prevalence and highly significant association with WBV exposure, as it was reported by 83% of the workers exposed to WBV and by only 21% of the people belonging to the control group. Burström et al. [21] conducted another questionnaire study on miners working in four different open-pit mines, located in the Artic, in four different countries: Finland, Norway, Russia and Sweden. The objective of the questionnaire

was to find evidence that the prevalence of musculoskeletal diseases is higher among vehicle operators with respect to other workers, due to the higher exposure to WBV. In total, 1323 workers answered took part in the study. 49% of the participants reported to have been subjected to low-back pain during the 12 months previous the questionnaire and the reported prevalence of neck pain was 40%. The authors could not find a significant difference between drivers and non-drivers; however, this could be due do other risks factors to which mineworkers are exposed.

1.1.2 Hand-Arm Vibration

A great number of workers use every day hand held vibrating tools and are therefore exposed to vibration transmitted through the hands and arms. Some examples of the fields most involved in this issue are dentistry [22], quarry [23], forestry [24] and construction [25]. Mechanical vibration transmitted through the hands can cause further problems in respect to the ones that are linked to WBV. Acute exposure of the arms and hands in fact, can result in a reduced blood flow to the body parts [26], resulting in numbness and increased sensitivity to cold [27]. Bovenzi conducted an overview of the scientific literature [28] on the subject and concluded that there is evidence to clearly support the link between hand-arm vibration and vibration-induced white fingers (VWF). Nilsson et al. [29] also conducted a systematic review of the scientific literature. Out of 4335 abstract, they selected 52 articles for further analysis. Based on those articles, the authors concluded that there is evidence to prove that hand-arm vibration increases the risk of developing vibration-induced white fingers, neuro-sensory injuries and carpal tunnel syndrome. ISO 5349-1:2001 [30] contains the guidelines to assess the risk associated with hand-arm vibration; however some authors are casting some doubts on the frequency weighting curves contained in this directive. For example, Tominaga [31], with reference to data available in literature, proposed a new prediction model for the risk arising from hand-arm vibration. This model contain different frequency-weighting curves in respect to the ones proposed by the standard, giving more weight to the higher frequencies, and has proven to be more reliable. This shows how properly tuned frequency weighting curves can affect the effectiveness of model for predicting the risks induced by mechanical vibration.

1.1.3 Foot Transmitted Vibration

While the effects of HAV have been subjects of many studies, the effects of vibration on the feet is not as well documented. Thompson et al. [32] report the case of a miner being subjected to occupational exposure to FTV, derived from drilling and bolting the platforms on which he was standing and operating scissor lifts and load-haul-dump vehicles. The worker was affected by blanching in the toes and cold intolerance for the 3 years prior to the examination and was diagnosed with occupational-induced Raynaud's phenomenon. Leduc et al. [33] monitored the vibration

exposure of miners from Norther Ohio: seven subjects were recruited, each subject operating a single machine. It was found that two workers were subjected to a vibration exposure exceeding the Exposure Limit Value, and one worker was subjected to a vibration exposure exceeding the Exposure Action Value. Two of those workers were diagnosed with vibration-induced white feet in conjunction with vibration induced white hands. All other workers reported discomfort at the lower limbs. Eger et al. [34] monitored the vibration exposure of 27 miners in Northern Ohio. None of the workers were found to be subjected to a dose of vibration exposure exceeding the Exposure Action Value. However, seven of the workers were diagnosed with vibration-induced white feet. The authors explain this mismatch with the fact that the affected workers are exposed to a vibration with a dominant frequency of 40 Hz, which is damped according to the weighting curves of ISO 2631-1:1997 [9]. While these frequency-weighting curves may be accurate to compute the risk to which the whole body is exposed, they cannot be used to assess the risk associated with the peripheral parts of the limbs. In fact, Goggins et al. [24] measured the vibration transmissibility along the vertical direction of 24 standing subjects, at 24 locations on the foot, in the frequency range from 10 Hz to 200 Hz. The results show that the vibration transmissibility is not uniform. For instance, the vibration transmissibility measured at the ankle has a resonance peak in the frequency range of 16-39 Hz; the one measured at the mid foot in the frequency range of 51-84 Hz and finally the toes has a peak in the vibration transmissibility in the frequency range of 99-147 Hz. For this reason, new tools must be developed to better model and assess this kind of risk.

1.2 Modelling the Human response to vibration

Different models to describe the response of the human body have been proposed and validated. Nikooyan et al. [35] proposed categorizing the models by two primary criteria; either their elements or the technique used to create the model.

When classifying models by their elements, passive models are created by fixing the values of the parameters of the model. However, passive elements may not be accurate to describe the overall response of the human body, which is indeed composed of active elements. Zadpoor et al. [36] modelled the human response to vibration during running and found that the human response to vibration is different from what would be expected when taking into account the effect of stiffness and damping of shoe insoles. For this reason, they proposed a model in which the muscular activity is described through changing parameters, whose value is obtained through an optimization process to minimize the vibration transmissibility to the head. In both passive and active models, the values of the parameters are never a function of time.

Musculoskeletal models require the complete description of the anatomy of the body parts to be considered and can provide detailed information about the load to which each anatomical region is subjected. Given the high computational cost associated with musculoskeletal models, this technique is better suited when the focus is only on specific districts and not the whole body.

An additional way to model of the response of the human body to vibration is through the Finite Element Method (FEM). This method allows modelling the different anatomical features and assigning to each of them their correct mechanical properties [37]. It has proven to be useful in the field of hand-arm vibration. For example, Pattnaik [38] proposed different models of the response of the fingers to vibration. Among these models, the one created through the FEM was able to demonstrate that at increasing frequency, the energy of vibration is dissipated closer to the point of contact between the finger and the vibrating surface. Another example is proposed by Hua et al. [39], in which they presented a multi-scale model. The larger scale was composed by a 2-D model of the finger tip and was used to compute the mechanical fields induced by acute vibration exposure. The smaller scale was used to model the capillary and the surrounding tissue and was used to compute the long-term effect of vibration exposure, in particular the growth of the tissue. As proposed by Noel [40], FEM models can also solve more complex problems, taking into account all three dimensions. He created, in fact, a 3-D model of the finger, and validated it with experimental data, to gain insight of the energy dispersion inside the different tissues, according to the excitation frequency.

Lumped parameters models rely on a set of springs, dampers and masses linked together with kinematic constraints. The elements used to compose the models do not need to represent an anatomical region and can be purely theoretical, with the objective of reproducing the overall response of the body to vibration. In an attempt to create a model which accurately represents the human response to vertical vibrations, Matsumoto and Griffin [41] compared six different passive lumped parameters models whose parameters were optimized to represent the response to vibration of the whole body of a standing person, in the frequency range of 0,5 Hz to 20 Hz. Two of the models were composed of a single degree of freedom, while the other four were composed of two degrees of freedom. The results show that two-degrees-of-freedom models can reliably reproduce the overall response to vibration of a standing person when subjected to vertical vibration. More complex lumped parameters models can be used to represent specific phenomena with a higher detail, or when more dimensions are considered. For example, Nawayseh and Griffin [42] proposed a 3 degrees-of-freedom model that could represent the response to vibration of a seated person when subjected to vertical vibration not only along the vertical direction, but also along the fore-and-aft direction. Subashi et al. [43] proposed two different lumped-parameters models to reproduce the response to

vibration along both the vertical and fore-and-aft directions of a standing person subjected to vertical vibrations in different postures. The two models were composed of five and seven degrees-of-freedom and were able to reproduce with a good accuracy the experimental data.

Because of the versatility of lumped parameter models, they have proven to be useful in many situations, including ergonomic design from car suspensions [44], [45] to power hammers [46], and situations where direct measurement is not a viable option, such as the force exchanged between the regions of the body [47], [48]. In addition, they make it possible to estimate the effects that a change in some parameters can have on the whole system [49], [50]. Their geometry and parameters, however, must be customized when trying to investigate the effect of vibration exposure on specific body parts.

One such customization relates to the representation of the foot-ankle system. Simkin and Leichter [51] propose a simple model of the arch of the foot to gain insight about the relationship between calcaneal inclination and energy storage capability of the foot. As Figure 2 shows, the model is composed of two rigid bars, connected by a hinge at one end, and by a spring at the other end. The model is symmetric in respect to the vertical line passing at the hinge, and the initial inclination of the bars in respect to the horizontal line is assumed representative of the calcaneal inclination. The model reproduced the load-deformation curve measured on human cadaveric feet [52] through an exponential function of the force-deformation function of the spring. However, this model was not able to predict the energy stored in the feet.

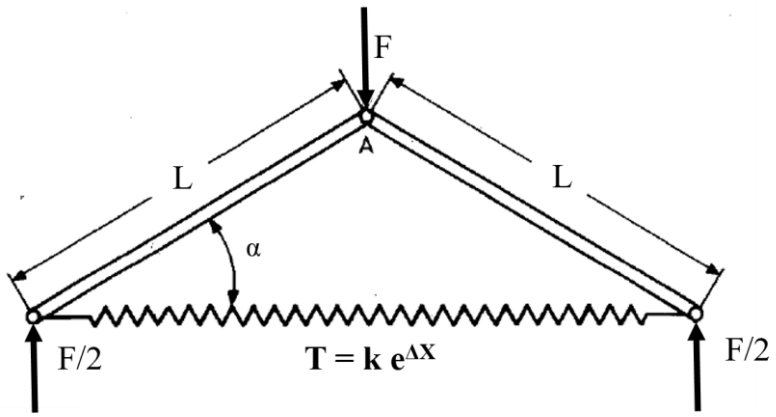

Figure 2: scheme of the lumped parameters model of the arch of the foot proposed by Simkin and Leichter

Gefen proposes another lumped-parameters model, with the objective of estimating the in-vivo elastic properties of the plantar fascia [53]. The structure of this model is similar to the structure of the model previously presented, as it is still composed of two bars hinged together at one end, however the bars of this other model are not of equal length, and the plantar fascia is modelled with an element with

both elastic and viscous properties. The author used x-rays to estimate the deformation of the plantar fascia, and a dynamic foot-ground contact pressure display to measure the force distribution on the foot. The model was then used to compute the force acting on the viscoelastic element based on the pressure distribution at the feet, during the walking stance phase. The mean stiffness of the plantar fascia resulting from this method is $(170\pm45)\cdot10^3$ N/m, which is comparable with the value obtained from direct measurements on specimens extracted from cadavers: $(204\pm50)\cdot10^3$ N/m.

Kim and Voloshin propose another lumped-parameters model, to investigate the effect that surgical release of the fascia has on the load bearing capability of the foot [54]; the model is shown in Figure 3.

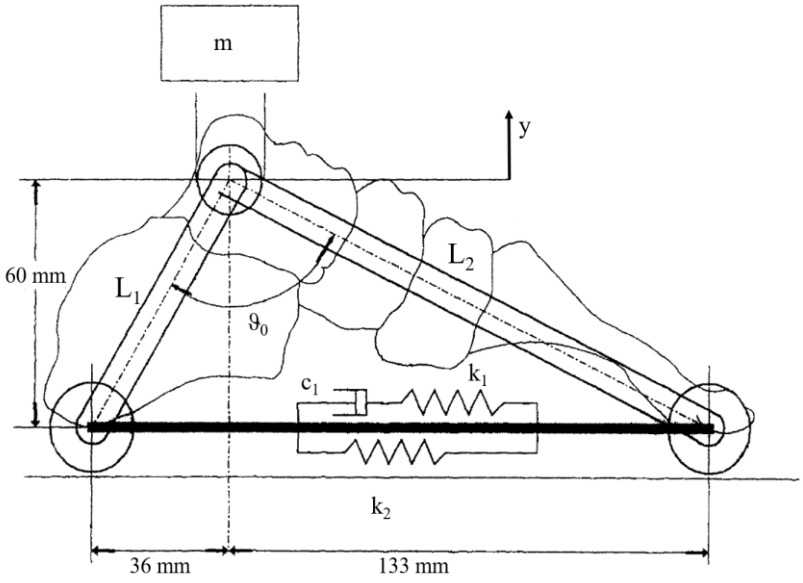

Figure 3: scheme of the lumped parameters model of the arch of the foot proposed by Simkin and Leichter

The model is still composed of two rigid bars, hinged at one end, but it is no more symmetric with respect to the vertical axes. Moreover, the other ends are no more connected by a single viscoelastic element, but by two parallel elements. One is purely elastic, k_2, while the other, representing the fascia, has both elastic and viscous properties, k_1 and c_1, in series. Additionally, one torsional damper and spring element connected to the two bars (not shown in picture) represents the elastic and viscous properties of the ligaments of the foot. One mass, m, connected to the ankle represents the rest body, instead than a force, as in the model previously presented. The parameters of the model have been optimized to fit in a least-squares sense the transmissibility function at the ankle. Such function was measured only using one subject, casting doubts on the generalization of the results; however, the method used would not have been different if the average curve obtained from a high number of

different subjects was used instead. After the fitting process, the authors used the model to compare the static load bearing capability with and without the viscoelastic element representative for the plantar fascia. The authors also used the proposed model to estimate the effect that a different initial angle of the arch of the foot has on the load bearing capabilities of the structure. Results show a linear relationship between a decrease in the height of the ankle joint and a decrease in the load bearing capability of the foot. Authors suggest that this relationship may be linked to the low marching and walking performances of people affected by a flat arch of the feet.

Given the task of representing the different response to vibration of various peripheral portions of the foot, as measured by Goggins et al. [24], a new model, with a higher number of degrees of freedom, needs to be developed.

1.3 Devices for testing the human response to vibration

Beyond the epidemiological studies mentioned above, it is possible to study the mechanical vibrations transmitted to the body through a biomechanical approach. Experimental data can be collected under controlled conditions and the effects and the risk of injury can be studied from the mechanical responses obtained [55]. The quantities mainly used to express the biomechanical response of the human body are the driving point mechanical impedance (DPMI), or apparent mass (AM) and the Transmissibility Function (TF). Both quantities are function of the frequency, and are computed as transfer functions, i.e. ratio between the spectrum of the output signal, and the spectrum of the input signal. The estimation of the AM requires, as input signal, the measurement of the acceleration at the driving point, i.e. the point through which the vibration is transmitted to the body. Figure 4 shows the driving points defined by ISO 2631-1:1997, according to the posture of the subject. The output signal to be measured is the force exchanged between the subject and the driving point. This quantity not only provides information about the biomechanical response of the human body to vibration, but it also relevant in the study of interactions between civil structures and the body.

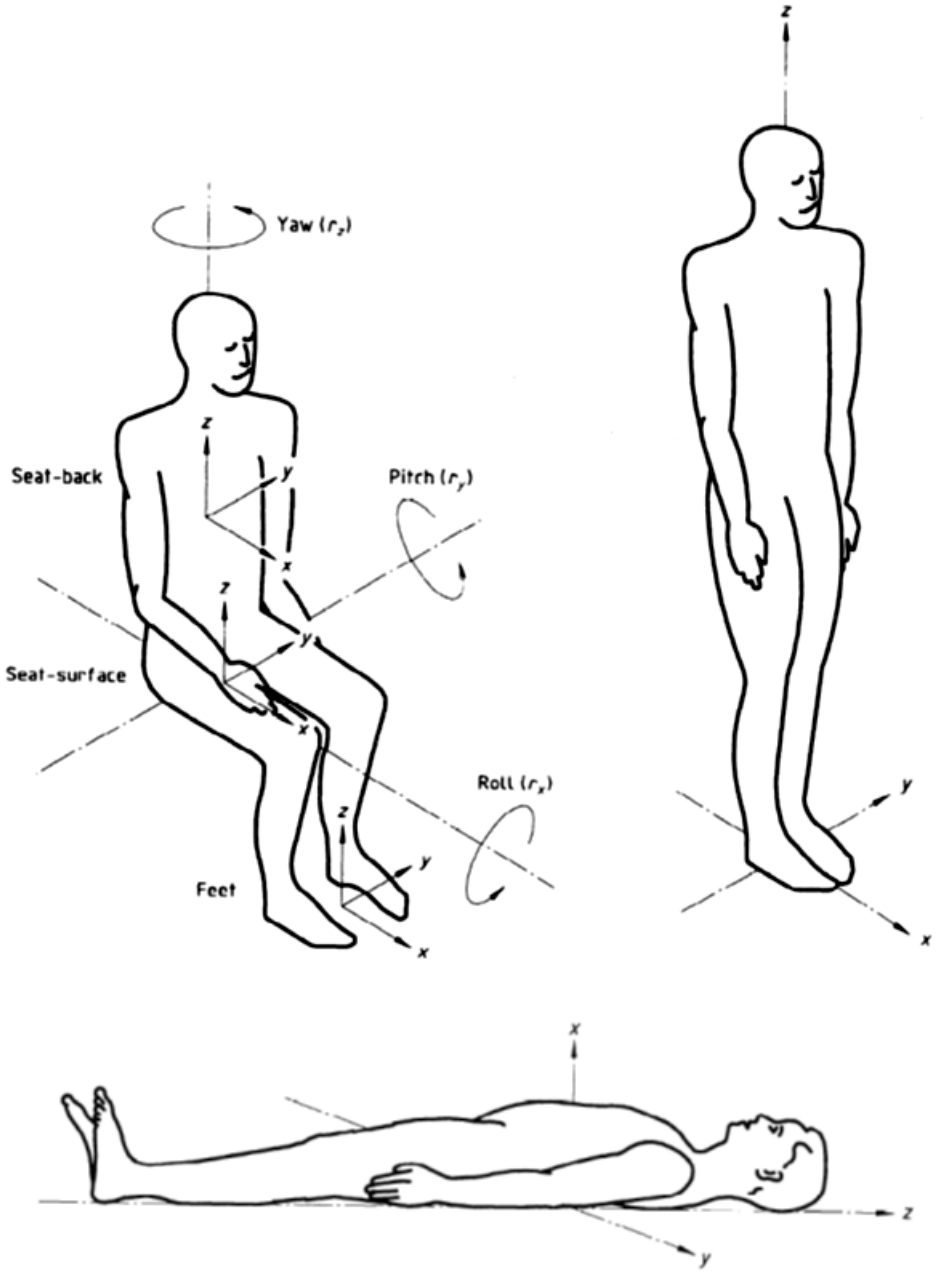

Figure 4: reference systems applied to the human body in different positions (seated, standing and recumbent) as defined by ISO 2631-1:1997

The estimation of the transmissibility function requires the measurement of the acceleration at the driving point, which is the input signal, and at the position of the body at which it is required to measure such quantity. This quantity provides information about how the vibration is transmitted from the driving point to different segments of the body. AM and TF together allow the reconstruction of the resonances of the human body, i.e. the frequencies to which the body is most sensitive to vibrations.

The mechanical signals used as input to experimentally estimate the AM and the TF are generated through machines called shakers. It is possible to classify these machines according to the

degrees of freedom of the vibrating platform and according to the actuation system. Figure 5 shows the visual representation of the classification matrix.

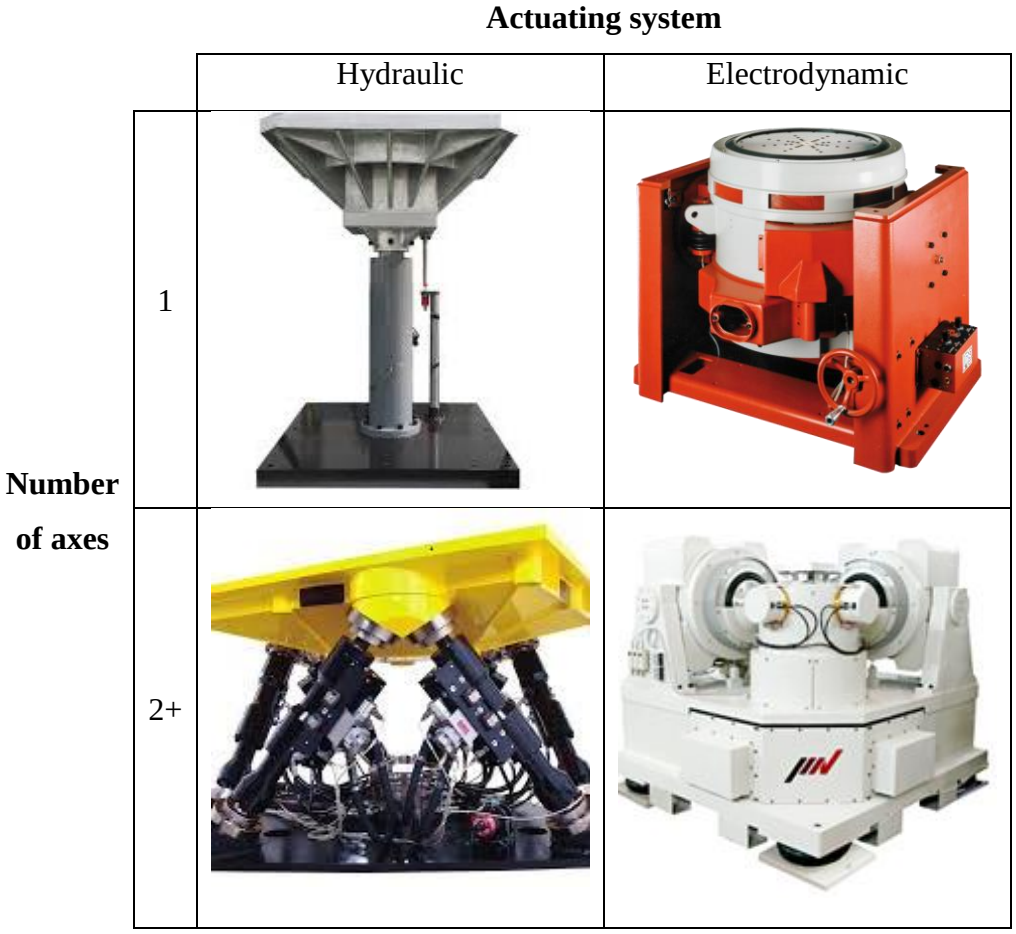

Figure 5: visual representation of the shaker classification matrix

Focusing on the number of degrees of freedom of the vibrating platform, single axis shaker can generate a mechanical stimulus, either sinusoidal, random or deterministic, along one direction at a time. The multiaxial response to vibration of the object of the test is often estimated as the sum of the responses of the object along the three mutually perpendicular spatial direction. This can yield to accurate results only if the linearity hypothesis is met. To obtain satisfactory results even in case of non-linear systems like the human body [56], [57], multiaxial shakers generating mechanical vibrations along two or more perpendicular spatial axes simultaneously have been developed.

Shakers can be divided in two categories depending on the actuation principle, i.e. hydraulic and electrodynamic. The end-effector of the hydraulic shakers is moved through hydraulic actuators, each one controlled by a servo-valve. The end effector of electrodynamic shakers is moved by large electromagnets within the shaker body, that interact with permanent magnets located on the moving part. A signal generator creates the electrical stimulus needed to move the vibrating platform and an

amplifier increase the amplitude of the electric current up to the level required to move the end effector.

The proposed classification groups most of the existing shakers, although some differences still hold between the industrial and academic worlds due to different uses. Team Corporation (11591 Watertank Road, Burlington, WA, USA) is one of various producers which offer a range of state of the art hydraulic shakers that can be used to better understand the differences in design and application. Table 1 contains the performances reached by the machines available in the catalogue of Team Corporation. As it is possible to see, the values of force rating, stroke and admissible payload are positively correlated with the size of the shaker. Instead, greater, heavier structures lead to narrower frequency bandwidth, which reduce the adaptability of the shaker to many testing fields. Figure 6 shows the images of such machines.

Table 1: Machines available in the catalogue of Team Corporation and their performances

Performance Characteristics	Mantis™	CUBE®	Tensor™ (Servo-hydraulics)	Electro-dynamic systems
Degrees of freedom	6	6	6	6
Frequency Bandwidth [Hz]	100	250	700	2000
Maximum Displacement Pk-Pk [mm]	150	100 (vertical) 50 (horizontal)	13	Shaker Dependent
Typical payload [kg]	50 - 2000	25 - 500	5 - 50	Shaker Dependent
Maximum force rating [kN]	315	62	36	Shaker Dependent

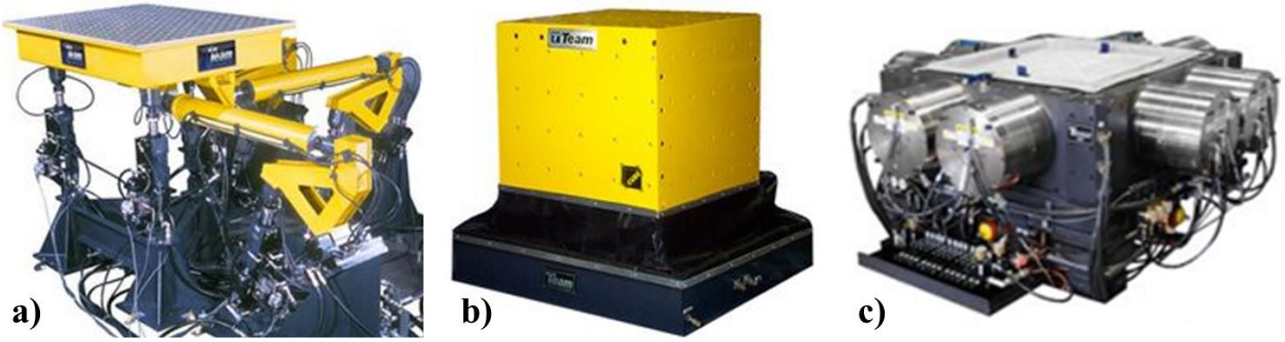

Figure 6: images of the machines produce by Team Corporation. a) Mantis™; b) The Cube™; c) Tensor™

MTS Systems is another example of company that produces hydraulic shakers. The catalogue includes the Multiaxial Simulation Tables (MAST™) family, which are bulky platforms, suitable for testing heavy structures at low or medium frequencies and requiring high forces and stroke length. Among them, the orthogonal platforms can reach up to 50 Hz of excitation; while the hexapod ones provide a bandwidth of 250 Hz. Figure 7 shows an example of a machine belonging to each class.

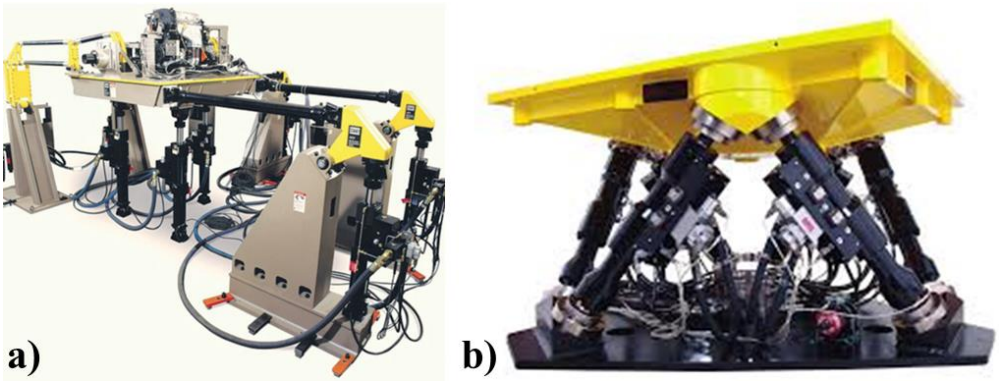

Figure 7: hydraulic shakers produced by MTS Systems belonging to the MAST™ family: a) Orthogonal; b) Hexapod

Electrodynamic shakers are more appropriate than hydraulic shakers for applications where a smaller payload and a smaller stroke is required, as they are more compact, cost-effective and provide also a greater bandwidth of excitation and a faster response in frequency control. An example of commercially available multiaxial electrodynamic shakers is the MA-Series™, developed by Sentek Dynamics (2370 Owen Street Santa Clara, CA, USA). Three electrodynamic shakers, oriented along the three mutually perpendicular spatial axes, provide the motion to the moving platform along the three translational degrees of freedom.

Table 2: Machines of the family MA-Series™ available in the catalogue of Sentek Dynamics and their performances

Machine ID	MA-1000-4H	MA-2000-4H	MA-3000-4H	MA-5000-5H	MA-6000-5H
Sine Force Peak per Axis [kN]	9,8	19,6	29,4	49	58,8
Random Force per Axis [kN]	6,9	13,7	20,6	34,3	41,2
Shock Force Peak per Axis [kN]	14,7	29,4	44,1	73,5	88,2
Max Working Frequency [Hz]	2000	2000	2000	2000	2000
Max Acceleration Sine Peak [m/s²]	68,6	147	176,4	245	294
Max Velocity [m/s]	1	1,1	1,2	1,2	1,2
Max Displacement [mm]	51	51	51	25	25
Max Static Payload [kg]	70	100	150	500	500

IMV Corporation (2-6-10 Takejima, Nishiyodogawa-ku, Osaka, 555-0011, Japan) includes in its catalogue similar equipment, with the TS-Series™, that allow a broad selection of shakers that provide forces from 9 to 95 kN, and up to 1 kHz in bandwidth. Figure 8 shows an example of these machines.

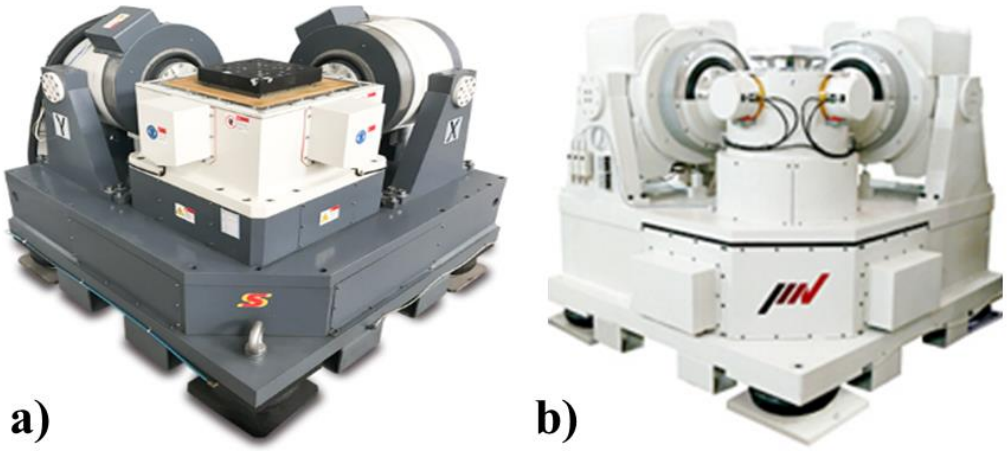

Figure 8: Electrodynamic shakers. a) MA-Series™ produced by Sentek Electronics; b) TS-Series™ produced by IMV Corporation

The machines commercially available are characterized by a poor ratio between working volume and the overall volume, and not all the laboratories own the necessary room to host such a structure. Moreover, the optimal positioning for the shaker would be embedded in the ground to avoid any undesired vibration, thus requiring extensive modification to the pre-existing structure of the laboratory. For these reasons, alternative solutions have been developed to perform the same kind of tests and measurements, optimizing costs and space utilization.

These alternative solutions can be developed based on various robotic architectures, chosen according to specific needs and resources available. Architectures can be divided into two main categories: serial and parallel [58]. Serial manipulators consist of rigid links connected one after the other by various types of joints, typically revolute and prismatic. Parallel manipulators consist of two or more closed-loop kinematic chains in which the end-effector is connected to the fixed base by at least two independent serial kinematic chains. Figure 9 shows an example of the two different architectures.

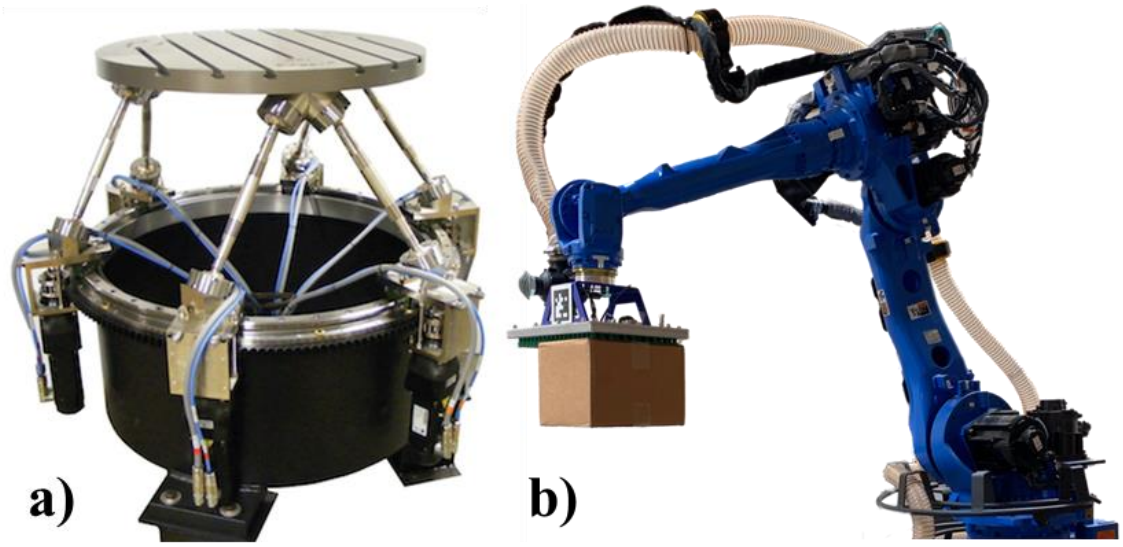

Figure 9: examples of commercial applications for parallel and serial architecture. a) Parallel robot R3000 produced by Mikrolar b) Serial robot PICK™ produced by Boston Dynamics (78 4th Ave, Waltham, MA, USA)

Both architectures offer advantages and disadvantages. Serial manipulators offer a higher ratio between working volume and occupied space. However, the positioning error accumulates at each joint, the maximum force is limited to the force of the weakest actuator in the chain and the overall stiffness is low, due to the cantilever layout. For these reasons, they are more suitable for repetitive tasks over long periods of time, operations in hazardous environments, and precision work with high degree of reliability. Some examples of their applications are welding, painting, polishing, injection

moulding, laser and plasma cutting, assembly, packaging and material handling. Meanwhile, parallel robots ensure higher accuracy [59], because the positioning error of the end effector is the average of the errors at all the joints. Additionally, they provide higher rigidity and actuation force because the load is divided into the parallel chains. However, their kinematic equations are more difficult to obtain, and they have a smaller ratio between workspace and total occupied volume. The current industrial applications of parallel robots lie in domains such as fine positioning devices, simulators, moving platforms, pick and place, machine tools, medical applications and force sensors [60].

The design of parallel robots needs to combine two opposing objectives: the first is to maximize the working volume, while the second is to maximize the performances inside the working volume. Wan et al. [61] conducted a survey on the techniques used to optimize the parallel robots, and identified two main strategies. The first is based on finding the set of design parameter that maximize the working volume, given the constraints on the quality of the transmission, expressed through performance indexes. The second is to find the set of design parameters which leads to a working volume that fits as close as possible the prescribed regular workspace. Both methods however lead to a multi-objective, non-linear optimization problem, with no analytical equations available. This is due to how the performance index are defined. Stamper et al. [62] used a Monte Carlo analysis to maximize only the working volume, showing that this would lead to a delta robot with an ill-conditioned workspace. Liu et al. [63] described through analytical equations the working volume of a linear delta with vertical actuation axes. This allows to directly compute the size of the robot with a cylinder of desired dimensions inscribed into the workspace. As explained before, however, as only the working volume is considered, the performance index distribution across the working volume, computed after the dimensions' selection, is characterized by sub-optimal values. The most commonly used performance indexes are the manipulability and the conditioning number (or its inverse). The manipulability is defined as the product of the singular values of the Jacobian matrix, while the conditioning number is defined as the ratio between the largest and the smallest singular value of the Jacobian matrix. This value is 1 when the two values are equal, i.e. when the velocity ellipsoid is a sphere, and tends to infinity in proximity of a singularity. For this reason, the inverse is most commonly used, thus obtaining an index comprised between 0 and 1 [64]. Different authors proposed algorithms to estimate the optimal solution. Courteille et al. [65] proposed new indexes for the dimension synthesis of a classical delta robot, based on the stiffness matrix instead than on the Jacobian matrix. The indexes defined could not be computed through analytical equations, so a genetic algorithm was used for the optimization process. The total mass of the robot was set as an optimization boundary, while solutions that would lead to a workspace lower than the one desired

were discarded. Giberti et al. [66] also proposed a linear delta robot with vertical actuators to manipulate the three translational degrees of freedom of the platform of a 3-D printer. The authors fixed the size of the moving platform, as it was constrained by the size of the payload, and used a genetic algorithm to optimize the other design parameters: length of the links, size of the base of the robot, and angular distance between the actuators. The objective of the optimization was to maximize the working volume, while the maximum force and transmission factors, who are function of the Jacobian matrix, were constrained. Additional constraints were set on the maximum joint angle and on the boundaries of the size of the design parameters. Stock and Miller [67] proposed an exhaustive search minimization algorithm to synthetize the dimensions of a linear delta with horizontal parallel actuators. The authors focused on two performance indexes. The first is the integral average of the inverse of the conditioning number, across the vertical cross section of working volume of the delta robot, normalized by the surface of the cross section of working volume itself. The second is the space utilization, computed as the ratio between the area of the cross section of the working volume and the area of smallest regular rectangle containing both the cross section of the working volume and the actuators. The objective function was defined as the weighted sum of the two indexes, and it was numerically computed for all the values allowed for the optimization variables, after a discretization process. Given the properties of the two architectures, the parallel configuration was considered most advantageous for studying the mechanical response of the human body to vibration. Given the low computational efficiency of the methods previously reported in literature for optimizing the kinematic of parallel robots, a new approach, based on the inverse of the manipulability number, has been developed for this application.

Chapter II

2 Design of the linear delta shaker

The parallel robot was designed to support a standing person and generate mechanical vibration independently along the three mutually perpendicular spatial axes in the frequency range of 0.5 Hz to 30 Hz, reaching acceleration values of 5 m/s^2 with a maximum displacement of ±20 mm along the axis composing the horizontal plane and ±30 mm along the vertical axis.

Parallel configurations can generate three translational degrees of freedom using different layout. The classic delta robot [68] is composed of three rotational motors; each of them is connected to the end effector through a rigid link and an articulated parallelogram. All the elements are connected though revolute joints. Figure 10 shows the kinematic scheme of the delta robot as proposed by Clavel in the original patent [69].

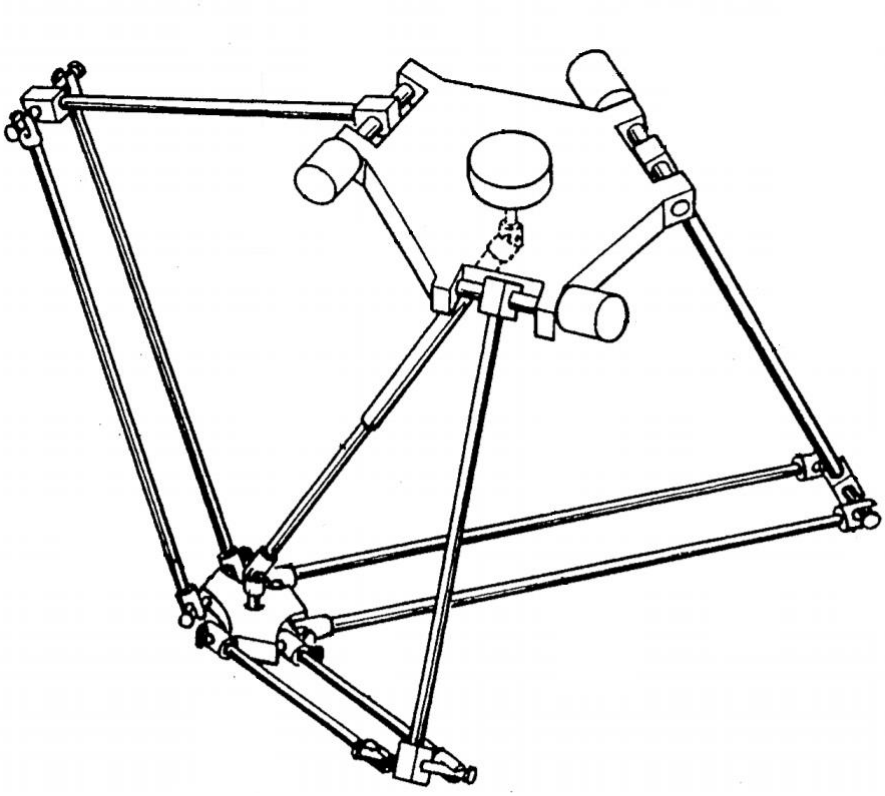

Figure 10: kinematic scheme of the original delta robot proposed by Clavel

The linear delta with vertical actuator [70] is composed of three linear actuators laying in the vertical axis, each of them connected to the moving platform through an articulated parallelogram. This

solution allows a larger travel space (theoretically infinite) along the vertical direction and a stiffer structure; for these reasons, this arrangement was selected for the shaker described in this work.

The first step in the design process was to obtain the dimensions of the kinematic of the machine. This step requires the definition of an optimization process, based on the inverse and direct kinematic, and on the Jacobian Matrix of the robot. The actuators were then selected through the creation of a multibody model of the machine, that allowed to estimate the forces at the various joints. The third step was the drawing of all the machine components. The dimensioning of the custom part was performed with the aid of a finite elements model, to ensure that the machine can reach the bandwidth performances required.

2.1 Kinematic of a linear delta robot

2.1.1 Selection of the dimensions of the linear delta shaker

The selection of the defining dimensions of the linear delta robot was the first step of the design, as shown in [71]. Dimensions are the radius of the base, i.e. the distance between the centre of the robot and the actuation axes, the length of the links, and the radius of the moving platform, i.e. distance between the centre of the moving platform and the centre of the rotational joints connecting the links to the platform. With reference to Figure 11, dimensions are the moduli of the vectors $\underline{s}_i$, $\underline{l}_i$ and $\underline{b}_i$. The size of the radius of the moving platform was set in advance equal to 250 mm, as it should be wide enough to host safely a person standing on it.

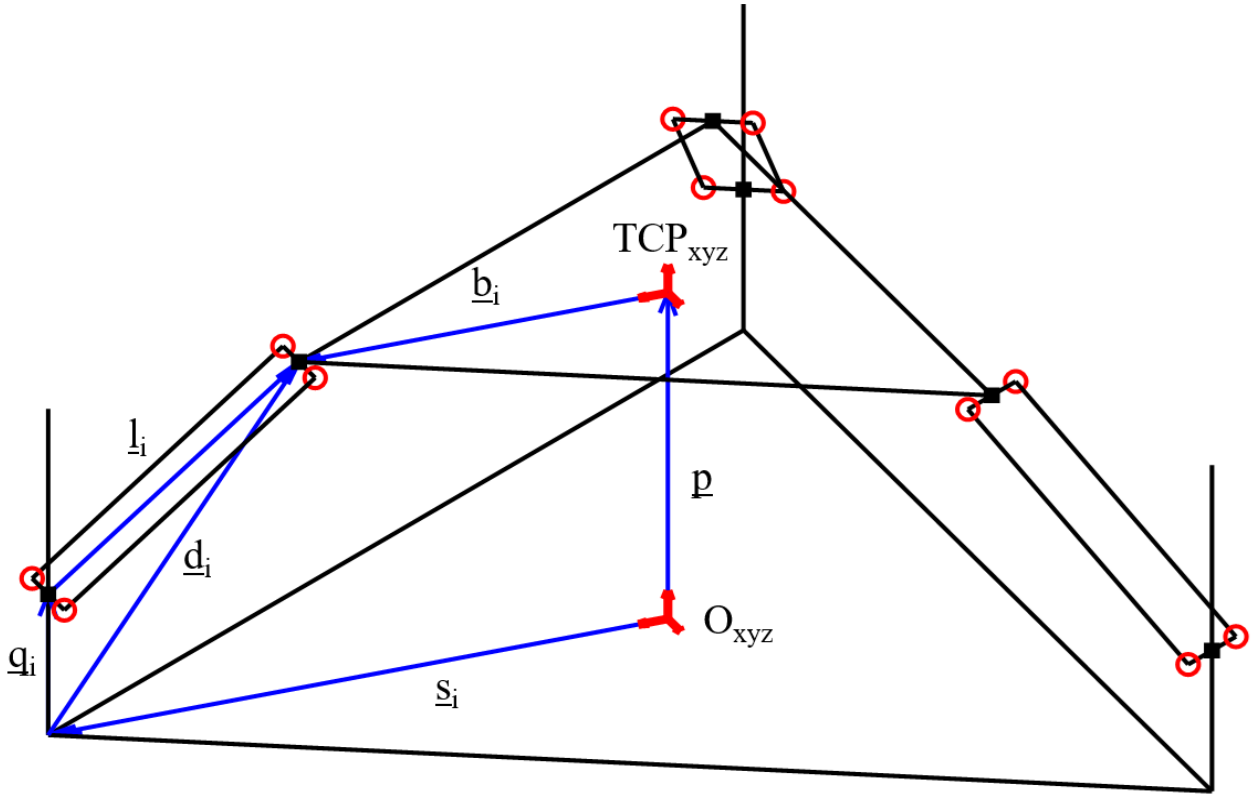

Figure 11: Kinematic scheme of a linear delta robot with vertical linear axes

The parameters were selected using an optimization procedure. Since the requirements fix the working volume, the objective of the optimization is to minimize the dimensions of the robot, while maintaining a good manipulability inside the working volume. The inverse of the conditioning number has been selected to represent the manipulability. This index is defined as the ratio between the smallest and the largest singular value of the Jacobian Matrix of the robot.

To obtain the Jacobian Matrix, the inverse and direct kinematic equations must first be computed. The following demonstrations are derived from ref. [72] and are included for the sake of completeness.

The point and vectors used to describe the kinematic of the delta robot, which are shown in Figure 11, are defined as follows:

- Reference coordinate system: O_{xyz}
- Unit vectors of the reference coordinate system O_{xyz}: $(\hat{x}_o \quad \hat{y}_o \quad \hat{z}_o)$
- Reference system integral with the moving platform: TCP_{xyz}. It must be noted that, due to the linear delta kinematic constraints, this reference system is always parallel to O_{xyz}.
- Unit vectors of the moving platform coordinate system TCP_{xyz}: $(\hat{x}_{TCP} \quad \hat{y}_{TCP} \quad \hat{z}_{TCP})$
- Position vector of TCP_{xyz}: $\underline{p}$

- Components of $\underline{p}$ along the reference coordinates system O_{xyz}:

$$\begin{Bmatrix} p_x \\ p_y \\ p_z \end{Bmatrix}$$

- Linear actuator and joint index: i
- Distance between O_{xyz} and the projection of the linear actuators along the plane defined by $(\hat{x}_o \quad \hat{y}_o)$: s
- Position vector of the projection of the i-th linear actuator along the plane $(\hat{x}_o \quad \hat{y}_o)$: $\underline{s}_i$. Given the radial symmetry of the linear delta, its components are:

$$\begin{Bmatrix} s\cos\left(\frac{2\pi}{3}(\mathrm{i}-1)\right) \\ s\sin\left(\frac{2\pi}{3}(\mathrm{i}-1)\right) \\ 0 \end{Bmatrix}$$

- Distance between TCP_{xyz} and the joints attached to the platform: b
- Position vector of the i-th joint attached to the platform in the reference system TCP_{xyz}: $\underline{b}_i$. As stated before, its components can be immediately computed:

$$\begin{Bmatrix} b\cos\left(\frac{2\pi}{3}(\mathrm{i}-1)\right) \\ b\sin\left(\frac{2\pi}{3}(\mathrm{i}-1)\right) \\ 0 \end{Bmatrix}$$

- Vector of the distance between the position of the i-th linear actuator end and its projection along the plane $(\hat{x}_o \quad \hat{y}_o)$: $\underline{q}_i$. Its components are defined as:

$$\begin{Bmatrix} 0 \\ 0 \\ q_i \end{Bmatrix}$$

- Length of the linear delta links: l
- Vector connecting the joint of the i-th linear actuator to the i-th joint of the moving platform: $\underline{l}_i$
- Unit vector of $\underline{l}_i$: $\hat{v}_i$
- Vector connecting the projection of the i-th linear actuator on the plane $(\hat{x}_o \quad \hat{y}_o)$ and the i-th joint of the moving platform: $\underline{d}_i$

With reference to Figure 11, it is possible to write the following equations:

$$\underline{l}_i = \underline{d}_i - \underline{q}_i \tag{2.1}$$

$$\underline{d}_i = \underline{p} + \underline{b}_i - \underline{s}_i \tag{2.2}$$

The inverse kinematic of the delta shaker can now be obtained. By computing the square of both terms of equation 2.1, it is possible to write:

$$\underline{l}_i^T \cdot \underline{l}_i = \left(\underline{d}_i - \underline{q}_i\right)^T \cdot \left(\underline{d}_i - \underline{q}_i\right) \tag{2.3}$$

Which can be written as:

$$\underline{l}_i^T \cdot \underline{l}_i = \underline{d}_i^T \cdot \underline{d}_i - \underline{q}_i^T \cdot \underline{d}_i - \underline{d}_i^T \cdot \underline{q}_i + \underline{q}_i^T \cdot \underline{q}_i \tag{2.4}$$

Given the definitions of the vectors $\underline{q}_i$ e $\underline{l}_i$, it is possible to obtain the following quadratic equation with the unknown q_i:

$$q_i^2 - 2\underline{d}_i^T \cdot \hat{z}_o \cdot q_i + \underline{d}_i^T \cdot \underline{d}_i - l^2 = 0 \tag{2.5}$$

From the previous equation 2.5 it is possible to compute q_i as a function of $\underline{d}_i$. Given the position of the platform in respect of the links of the delta, the negative solution is taken.

$$q_i = \underline{d}_i^T \cdot \hat{z}_o - \sqrt{\underline{d}_i^T \cdot \left(\hat{z}_o \cdot \hat{z}_o^T - I\right) \cdot \underline{d}_i + l^2} \tag{2.6}$$

It is now possible to substitute the term $\underline{d}_i$ with the terms provided by equation 2.2. The relationship can be further simplified given the fact that the vectors $\underline{b}_i$ e $\underline{s}_i$ are defined without components along $\hat{z}_o$. In this way, it is possible to compute each q_i as a function of $\underline{p}$:

$$q_i = p_z - \sqrt{\left(\underline{p} + \underline{b}_i - \underline{s}_i\right)^T \cdot \left(\hat{z}_o \cdot \hat{z}_o^T - I\right) \cdot \left(\underline{p} + \underline{b}_i - \underline{s}_i\right) + l^2} \tag{2.7}$$

The direct kinematic can be computed too. The first step is to compute the squares of both terms of equation 2.1, and to substitute $\underline{d}_i$ with the terms provided by equation 2.2:

$$\underline{l}_i^T \cdot \underline{l}_i = \left(\underline{p} + \underline{b}_i - \underline{s}_i\right)^T \cdot \left(\underline{p} + \underline{b}_i - \underline{s}_i\right) - 2\left(\underline{p} + \underline{b}_i - \underline{s}_i\right)^T \cdot \underline{q}_i + \underline{q}_i^T \cdot \underline{q}_i \tag{2.8}$$

Given the symmetry of the delta, the modules of the vectors $\underline{l}_i$, $\underline{b}_i$ e $\underline{s}_i$ are known and equal for each i, hence it is possible to write:

$$p^2 + b^2 + s^2 - l^2 + 2\underline{p}^T \cdot \underline{b}_i - 2\underline{p}^T \cdot \underline{s}_i - 2\underline{b}_i^T \cdot \underline{s}_i - 2\underline{p}^T \cdot \hat{z}_o \cdot q_i - 2\underline{b}_i^T \cdot \hat{z}_o \cdot q_i + 2\underline{s}_i^T \cdot \hat{z}_o \cdot q_i + q_i^2 = 0 \tag{2.9}$$

By substituting in equation 2.9 the definitions of $\underline{b}_i$ ed $\underline{s}_i$ the following equation can be computed:

$$p_x^2 + p_y^2 + p_z^2 - (b-s)^2 - l^2 + q_i^2 - 2p_z q_i + 2p_x(b-s)\cos\left(\frac{2\pi}{3}(i-1)\right) + 2p_y(b-s)\sin\left(\frac{2\pi}{3}(i-1)\right) = 0 \quad (2.10)$$

By multiplying by 2 equation 2.10 for i = 1 and subtracting the same equation computed for i = 2 and i = 3, it is possible to obtain:

$$6p_x(b-s) + 2q_1^2 - q_2^2 - q_3^2 - 2p_z(2q_1 - q_2 - q_3) = 0 \quad (2.11)$$

Then, by subtracting the members of equation 2.10 computed for i = 2 from the members of the same equation computed for i = 3 the following relationship can be obtained:

$$2\sqrt{3}p_y(b-s) + q_2^2 - q_3^2 - 2p_z(q_2 - q_3) = 0 \quad (2.12)$$

The two previous equations 2.11 and 2.12 establish a linear relationship between p_x and p_z; and between p_y and p_z. So, by substituting p_x e p_y in equation 2.10 computed for i = 1, with the functions of p_z defined before, it is possible to write a quadratic equation with the unknown of p_z. Such equation has the following parameters:

$$\alpha p_z^2 + \beta p_z + \gamma = 0 \quad (2.13)$$

$$\alpha = \frac{(2q_1 - q_2 - q_3)^2 + 3(q_2 - q_3)^2}{9(b-s)^2} + 1 \quad (2.14)$$

$$\beta = \frac{3(q_2 - q_3)(q_3^2 - q_2^2) - (2q_1 - q_2 - q_3)(2q_1^2 - q_2^2 - q_3^2)}{9(b-s)^2} + \frac{2(2q_1 - q_2 - q_3)}{3} - 2q_1 \quad (2.15)$$

$$\gamma = \frac{3(q_2^2 - q_3^2)^2 + (2q_1^2 - q_2^2 - q_3^2)^2}{36(b-s)^2} - \frac{2q_1^2 - q_2^2 - q_3^2}{3} + (b-s)^2 + q_1^2 - l^2 \quad (2.16)$$

Therefore, from equation 2.13 it is possible to compute p_z. Given the geometry of the delta, only the positive solution is relevant. Then, from equation 2.11 and equation 2.12 it is possible to compute the other two components of the vector $\underline{p}$.

The index used for the optimization of the kinematic of the delta shaker is computed starting from the Jacobian matrix, therefore the relationship between the speed of the actuators and the speed of the

moving platform must be established. The first step is to compute the derivative of equation 2.4 in respect to time. By considering that l is constant in time, it is possible to write:

$$\dot{\underline{d}}_i^T \cdot \underline{d}_i + \underline{d}_i^T \cdot \dot{\underline{d}}_i + \dot{\underline{q}}_i^T \cdot \underline{q}_i + \underline{q}_i^T \cdot \dot{\underline{q}}_i - \dot{\underline{q}}_i^T \cdot \underline{d}_i - \underline{q}_i^T \cdot \dot{\underline{d}}_i - \dot{\underline{d}}_i^T \cdot \underline{q}_i - \underline{d}_i^T \cdot \dot{\underline{q}}_i = 0 \tag{2.17}$$

The previous equation (17) can be written as follows:

$$\left(\underline{d}_i - q_i \hat{z}_o\right)^T \left(\dot{\underline{d}}_i - \dot{q}_i \hat{z}_o\right) = 0 \tag{2.18}$$

The first factor of equation 2.18 is equal to the vector $\underline{l}_i$, according to equation 2.1; while $\dot{\underline{d}}_i$ is equal to $\dot{\underline{p}}$ according to equation 2.2, because the other terms are constant in time. So, by dividing both terms by the length of the links of the delta, the following relationship can be established:

$$\hat{v}_i^T \cdot \dot{\underline{p}} - \dot{q}_i \hat{v}_i^T \cdot \hat{z}_o = 0 \tag{2.19}$$

The previous equation 2.19 is valid for each of the three links, so it is possible to write it in the matrix form:

$$\begin{bmatrix} v_1^z & 0 & 0 \\ 0 & v_2^z & 0 \\ 0 & 0 & v_3^z \end{bmatrix} \begin{Bmatrix} \dot{q}_1 \\ q_2 \\ q_3 \end{Bmatrix} = \begin{bmatrix} v_1^x & v_1^y & v_1^z \\ v_2^x & v_2^y & v_2^z \\ v_3^x & v_3^y & v_3^z \end{bmatrix} \begin{Bmatrix} \dot{p}_x \\ p_y \\ p_z \end{Bmatrix} \tag{2.20}$$

Where the components along the three axes of the three unit vectors $\hat{v}_i$ can be easily computed from the kinematic chain of each link, expressed by equation 2.1 and equation 2.2. Considering the definitions of the vectors, given the geometry of the delta, it is possible to obtain:

$$\hat{v}_i = \frac{1}{l} \begin{Bmatrix} p_x + (b-s)\cos\left(\frac{2\pi}{3}(\mathrm{i}-1)\right) \\ p_y + (b-s)\sin\left(\frac{2\pi}{3}(\mathrm{i}-1)\right) \\ p_z - q_i \end{Bmatrix} \tag{2.21}$$

From equations 2.20 and 2.21 the so-called Jacobian matrix, J can be computed. Equation 2.22 shows the formula to compute such matrix.

$$J = \begin{bmatrix} \frac{P_x + D}{\sqrt{L^2 - \left[(P_x + D)^2 + (P_y)^2\right]}} & \frac{P_y}{\sqrt{L^2 - \left[(P_x + D)^2 + (P_y)^2\right]}} & 1 \\ \frac{P_x - D/2}{\sqrt{L^2 - \left[(P_x - D/2)^2 + \left(P_y + \sqrt{3}\cdot D/2\right)^2\right]}} & \frac{P_y + \sqrt{3}\cdot D/2}{\sqrt{L^2 - \left[(P_x - D/2)^2 + \left(P_y + \sqrt{3}\cdot D/2\right)^2\right]}} & 1 \\ \frac{P_x - D/2}{\sqrt{L^2 - \left[(P_x - D/2)^2 + \left(P_y - \sqrt{3}\cdot D/2\right)^2\right]}} & \frac{P_y - \sqrt{3}\cdot D/2}{\sqrt{L^2 - \left[(P_x - D/2)^2 + \left(P_y - \sqrt{3}\cdot D/2\right)^2\right]}} & 1 \end{bmatrix} \tag{2.22}$$

It is not possible to obtain a direct equation which links the inverse of the conditioning number of a linear delta robot with vertical actuation axes to the independent variables. For this reason, it was decided to follow a numerical process. Moreover, the inverse of the conditioning number is a function of the position of the moving platform along the horizontal plane, not only of the sizes of the delta shaker, as equation 2.22 shows. Therefore, a single value cannot represent a given set of sizes, and both the minimum and the maximum values assumed by the inverse of the conditioning number inside the required working volume were considered: C_{min} and C_{MAX}. Figure 12 shows the algorithm for the optimization process.

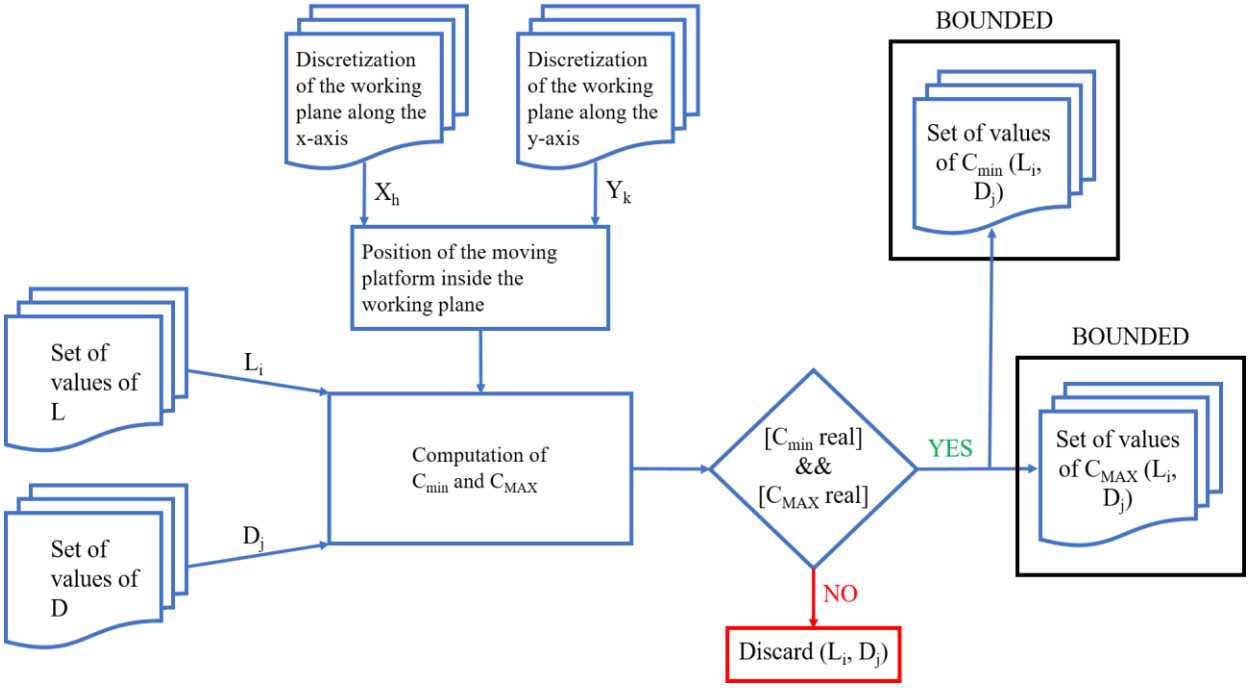

Figure 12: block diagram of the numerical optimization algorithm used to compute the defining dimensions of the linear delta robot with vertical actuation axes.

Two sets of values for the optimization variables were created. The length of the links assumed values between 150 mm and 250 mm, with a step of 5 mm. The radius of the base platform assumed values between 250 mm and 500 mm, with a step of 10 mm. The set of values of D was created by subtracting the radius of the platform, i.e. 250 mm, from the set of values of the radius of the base platform. The working area along the horizontal plane was discretized along both axes with a step of 1 mm. The position of the centre of the moving platform along the vertical direction was not considered, since the Jacobian Matrix does not depend on that variable. For all the combinations of values of D and L, the inverse of the conditioning number was computed at all the discretized points of the horizontal plane, as in [67]. If the inverse of the conditioning number computed for a given pair of optimization

variable assumed an imaginary value inside the working volume that pair of values was discarded, as in [65]. Out of all the remaining couples of values, it was selected the one which yields to smaller dimensions, provided that the maximum inverse of the conditioning number inside the working volume must be higher than 0,9 and the minimum must be higher than 0,55. The algorithm described was implemented in a MATLAB (MathWorks Inc., 1 Apple Hill Drive, Natick, MA 01760-2098) script. The two conditions are satisfied by the length of the links equal to 215 mm coupled with a radius of the base platform equal to 420 mm. With this couple of values, the minimum and maximum inverse of the conditioning number inside the horizontal plane of the desired working volume are 0,55 and 0,91 respectively.

2.1.2 Optimal proportions of the linear delta shaker according to the conditioning number

As explained, when optimizing the dimensions of a parallel robot, two opposing objectives must be achieved: compact size and kinematic performance [62]. This optimization is most often not performed with efficient analytical methods. Instead, genetic algorithms like in [65], or even extensive search methods, like in [67] and this dissertation, are used. These methods are most often slow and require great computational power. Moreover, there is the possibility to converge to a local optimum. However, they are the only choice, because the analytical equations of the performance indexes used to compute the function to be optimized have not been computed yet. Merlet [73] states, "The definition of the condition number makes clear that we cannot calculate its analytical form as a function of the pose parameters except for very simple robot". As defined by Olds [64], the inverse of the conditioning number is the ratio between the minimum and the maximum singular value of the Jacobian matrix, "J". In a square matrix, the singular values can be computed as the squared root of the eigenvalues of the matrix itself multiplied by its conjugate transposed, J^*, as shown in the following equation 2.23:

$$\sigma_i = \sqrt{\lambda_i} \tag{2.23}$$

where σ_i is the i-th singular value of J and λ_i is the i-th eigenvector of $J^* \cdot J$. Given that J is a 3x3 matrix, the index i changes from 1 to 3. Given that the Jacobian matrix is strictly Real, i.e. the three different radicands, shown in equation 2.23, are greater than 0, it is possible to transpose the matrix of J^T, and multiply J by it, and obtain equation 2.24:

$$J^T \cdot J = \begin{bmatrix} a_{11}^2 + a_{21}^2 + a_{31}^2 & a_{11} \cdot a_{12} + a_{21} \cdot a_{22} + a_{31} \cdot a_{32} & a_{11} + a_{21} + a_{31} \\ a_{11} \cdot a_{12} + a_{21} \cdot a_{22} + a_{31} \cdot a_{32} & a_{12}^2 + a_{22}^2 + a_{32}^2 & a_{12} + a_{22} + a_{32} \\ a_{11} + a_{21} + a_{31} & a_{12} + a_{22} + a_{32} & 3 \end{bmatrix} \quad (2.24)$$

Where a_{mn} is the element of the J matrix at raw m, column n. It is then theoretically possible to analytically compute the equation of the eigenvalues of the matrix shown in equation 2.24. The eigenvalues are the three roots x_i, i = 1,2,3 of a polynome of 3rd degree, that can be computed with this set of equations 2.25 – 2.30:

$$p = c - {b^2}/{3} \quad (2.25)$$

$$q = 2\left({b}/{3}\right)^3 - {b \cdot c}/{3} + d \quad (2.26)$$

$$\Delta = \left({q}/{2}\right)^2 + \left({p}/{3}\right)^3 \quad (2.27)$$

$$\Theta = \tan^{-1}\left(-2\frac{\sqrt{\Delta}}{q}\right) \quad (2.28)$$

$$y_i = 2\sqrt{-\frac{p}{3}} \cdot \cos\left(\frac{\Theta + 2\pi \cdot (i-1)}{3}\right) \quad (2.29)$$

$$x_i = y_i - {b}/{3} \quad (2.30)$$

Where b, c and d are the coefficients of the 2nd, 3rd, and 4th term of the polynomial, in order of power. The coefficient of the cubic term is supposed to be 1. Equation 2.28 is true only if the three roots of the polynomial are real. The resulting equation for three singular values of the Jacobian matrix will not be shown here due to not interrupt the dissertation, however the MATLAB code to compute them will be provided in Annex 2. Equation 2.29 clearly shows that it is impossible to know in advance which of the three singular values will be the highest and the lowest, therefore it is not possible to obtain a direct equation to compute the inverse of the conditioning number. It is however possible to obtain the direct equation for the manipulability of the robot, which is the product of those values.

Considering a linear delta robot with only two vertical actuators, lying in one plane, so with two degrees of freedom, its Jacobian matrix will be a square 2X2 matrix. It is then possible to compute

its singular values, as explained before. In this case, however, the computation of the two roots is straightforward, and it is possible to know in advance the smaller root, therefore it is possible to obtain a direct equation for the inverse of the conditioning number. As before the equation will not be provided directly, however the MATLAB code to compute it is provided in Annex 3.

Even if it possible to obtain direct equations to compute some of the kinematic performance indexes of parallel robots, such equations are valid only inside the working volume of the robot and can be cumbersome to use them. For this reason, the aim of this chapter is to propose a method through which it is possible to obtain simple approximate equations of the inverse of the conditioning number of the linear delta robot with vertical actuators, given a workspace with a square cross section in the horizontal plane. It will be shown that such equations can be used as direct functions for boundaries in an optimization process involving multiple objectives, or to directly obtain the proportions of a linear delta robot with vertical actuators given the requirements on the kinematic performances.

2.1.2.1 Method

As it is not possible to obtain a function to compute the inverse of the conditioning number of a linear delta robot with vertical actuators, it must be numerically computed for a given set of dimensions and a position in the horizontal plane. Equation 2.22 shows that the relevant dimensions are D, i.e. the difference between the radius of the circumference of the actuators and the radius of the moving platform, and L, i.e. the length of the links of the robot. The method here described was implemented through a dedicated MATLAB R2018a script. Figure 13 shows the block diagram of such method.

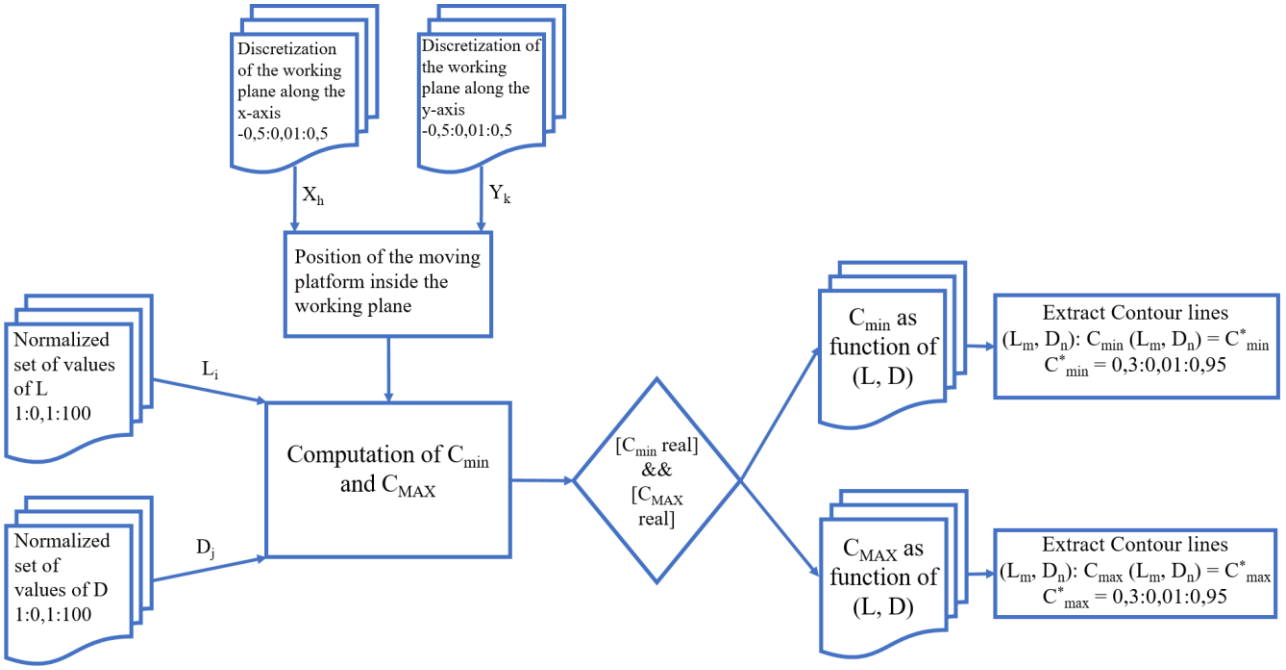

Figure 13: block diagram of the algorithm used to extract the data to estimate a direct mathematical link between the inverse of the conditioning number and the kinematic dimensions of a linear delta robot with vertical actuators

The first step was to create a set of dimensions and compute the maximum and minimum inverse of the conditioning number inside the working volume for all the combinations of dimensions, as it was done for the design of the kinematic of the linear delta shaker. In this case, however, all the dimensions are normalized. Through this normalization the proportions of the kinematic of the linear delta with vertical actuators will be the output of this method. This is possible since all the parameters belong to the same physical quantity, length. The horizontal section of the working volume is defined as a square with a side of 1. It is described as a grid of values ranging from -0,5 to 0,5 with a step of 0,01. Both L and D are defined in a set ranging from 1 to 100 with a step of 0,1. If a combination of L and D led to an imaginary inverse of conditioning number inside the working volume, then the value assigned to all conditioning numbers inside the working surface for that combination was set to 0.

The two surfaces, describing the minimum and the maximum inverse of the conditioning number inside the working volume as a function of L and D, are respectively called S_{min} and S_{max}. Then, the contour lines of these two surfaces obtained have been computed. Given that it is known a priori that the inverse of the conditioning number belongs to the interval [0, 1] by definition, the contour lines have been computed for the values from 0,3 to 0,95 with a step of 0,01. Values at the extremities of the interval are not considered as extremely low values would lead to poor

performances, while high values would lead to a very large robot compared to the working volume, as discussed previously.

The second step was to fit the contour lines with a family of curves described by simple equations, expressing L as a function of D. Preliminary results show that all of the contour lines of S_{max} have a minimum close to the origin of the axes. This is explained by the fact that the maximum of the inverse of the conditioning number is reached at the centre of the working volume, thus even robots with small dimensions in comparison to the size of the working volume can reach high kinematic performances at that point, given the correct proportions between the dimensions. For this reason, each contour line of S_{max} was fitted with two straight lines, shown in equations 2.31 and 2.32.

$$L = m_{inf} \cdot D + q_{inf} \tag{2.31}$$

$$L = m_{sup} \cdot D + q_{sup} \tag{2.32}$$

For each contour line obtained, first the median of all its points have been computed, both in the D and L dimension, then the straight line passing by the origin of the axis and the median point was computed and used to divide the points below and over it. Each of these two groups of points have been fitted with a different straight line, using the least-squared method. To ensure the best asymptotic fit, only the 750 points furthest from the origin have been used to fit each straight line and obtain its parameters: m_{inf} and q_{inf} for the points below the median line, and m_{sup} and q_{sup} for the points above the median line.

The contour lines of S_{min}, however, show a minimum whose distance from the origin of the axes increases as the defining value of the contour line increases. This is explained by the fact that the minimum inverse conditioning number inside the working volume is reached at the borders of horizontal cross section of the working volume. Therefore, given a fixed size of the working volume, a larger size would lead to a better performance inside the working volume. It is crucial to correctly describe the minimum point, and two different ways have been used to describe the contour lines of the S_{min} and S_{max}. The first was to describe them by using a family of rotated hyperboles. Figure 14 shows an example of a contour line of S_{min} and shows how the different points extracted have been used to fit different parameters.

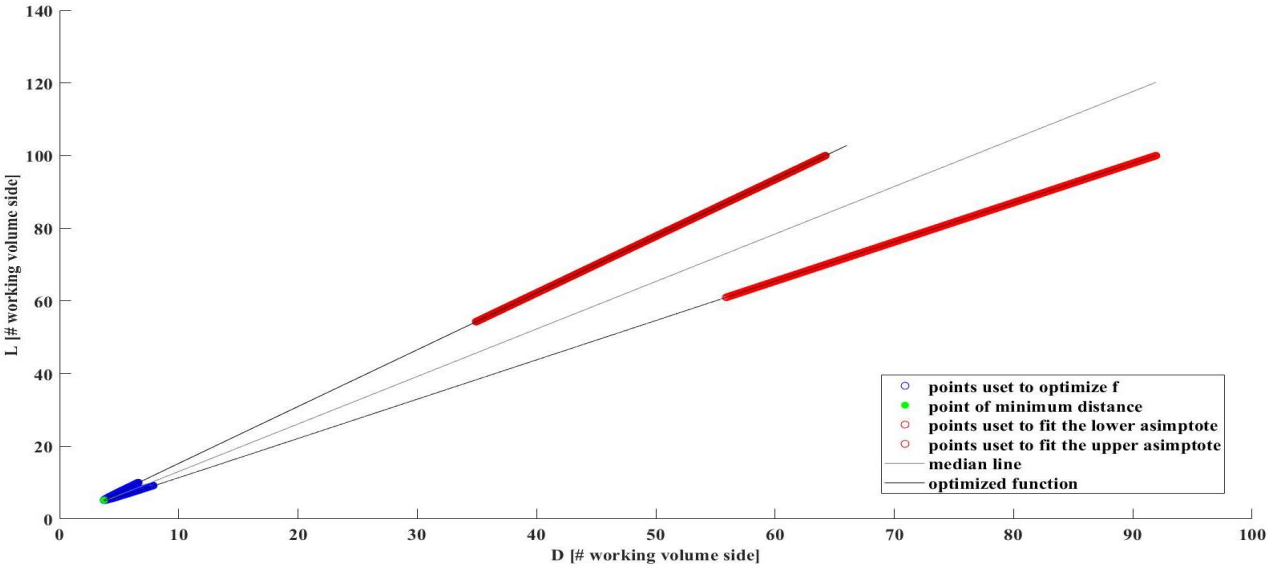

Figure 14: example of the process of fitting the points extracted from the contour lines of the minimum inverse conditioning number inside the working volume with a square horizontal cross section

First, the straight lines fitting the 750 points further from the origin above and below the median line have been computed, as explained before. In Figure 14 these points are shown in two different shades of red. These two lines have been then used as the first guess for the asymptotes of the hyperbole. The points have been then translated and rotated in such a way that they could be fitted with a hyperbole with a vertical asymptote and an oblique asymptote, intersecting at the origin of the axis. Equation 2.33 describe such function.

$$Y = \frac{m \cdot X^2 + f}{X} \tag{2.33}$$

The coordinates of the original intersection between the two fitted lines, DC and LC, have been computed as shown in the system of equations 2.34. The angle between the upper line and the ordinate axis, Ψ, was computed from the angular coefficient of the upper straight line, as shown in equation 2.35.

$$\begin{cases} DC = \dfrac{q_{inf} - q_{sup}}{m_{sup} - m_{inf}} \\ LC = m_{inf} \cdot DC + q_{inf} \end{cases} \tag{2.34}$$

$$\Psi = \frac{\pi}{2} - \tan^{-1}\left(m_{sup}\right) \tag{2.35}$$

The parameters DC, LC and Ψ have then been used as the first guess for the curve fitting, considering only the 160 points closer to the origin of the axis. In Figure 14 these points are shown in blu. Only this small number of points have been considered to focus the fitting process in the neighbourhood of the minimum of the hyperbole, not on the asymptotic branches. The first guess of parameter f was 1. The interior-point algorithm was used to compute the set that optimize the fitting in the least-squared sense. The boundaries of all the parameters was imposed to ±5% of the original value, except for the parameter *f*, that was constrained between 0,1 and 10. The boundaries on the first three parameters were set to be so strict to avoid that the presence of the singularity inside the range of interest during the optimization process, which would have led to a non-convergence of the algorithm. This process was necessary: by rotating the function shown in equation 2.35 in fact, to each abscissa (except for the singularity) correspond two ordinates. This would lead to poor results of the optimization process.
The second way to describe S_{min} focuses on the point closest to the origin of the axis, shown in green in Figure 14, which was extracted from each contour line. These points have been fitted with a straight line, to obtain the proportion of the dimensions of the linear delta shaker with vertical actuators that minimizes the dimensions given a desired minimum of the inverse conditioning number inside a workspace with a square cross section on the horizontal plane.

The third step of the method was to consider the nine parameters previously described as a function of the contour level. Through the trial and error method, different functions have been used to describe the link between each parameter and the level of the associated contour line, i.e. the value of the maximum/minimum conditioning number. The fit was considered acceptable when the Root Mean Squared Error (RMSE) between the points and the fitted function was lower than 0,05. The same procedure was used to fit the distance between the points of minimum of the contour lines of S_{min} and the origin as a function of the value of the minimum conditioning number associated to that contour line.

Finally, information obtained through this method can be used either to obtain direct equations for the constraints on the kinematic performances in an optimization process involving multiple objectives, or to directly compute the proportions of a linear delta shaker with vertical actuators, in the case that the requirements are posed only on the kinematic performances. For both cases, the algorithm proposed is the following.

1) Define the desired kinematic performance inside the working volume, which must have a square cross section in the horizontal plane, in terms of maximum and minimum inverse of conditioning number inside such working volume: C^*_{max} and C^*_{min}.
2) Estimate the parameters of the families of curves used to fit the contour lines.
3) The surface between the two straight lines computed through the parameters $q_{sup\ max}$, $q_{inf\ max}$, $m_{sup\ max}$ and $m_{inf\ max}$ provides the combinations of L and D that leads to $C_{max} \geq C^*_{max}$.
4) The surface inside the hyperbole defined in equation 2.33 is the area in which $C_{min} \geq C^*_{min}$, but not in the reference system defined by L and C. The coordinates must be first rotated of an angle Ψ and then translated by the vector [DC, LC]. Both these parameters can be computed from $q_{sup\ min}$, $q_{inf\ min}$, $m_{sup\ min}$ and $m_{inf\ min}$ as shown in equations 2.34 and 2.35. The parameter m in equation 2.35 is the angular coefficient of the diagonal asymptote of the hyperbole. It can be computed from the estimated parameters through equation 2.36.

$$m = \tan\left(\frac{\pi}{2} - \tan^{-1}\left(m_{\sup min}\right) + \tan^{-1}\left(m_{\inf min}\right)\right) \tag{2.36}$$

2.1.2.2 Results

Figure 15 and Figure 16 show respectively an example of the surface colour-map plot and contour lines example of the maximum and the minimum inverse conditioning number inside the working volume with a square horizontal cross section. The points below the diagonal straight line have a value of 0 due to the surface generation process. Those points, however, would lead to an imaginary inverse of conditioning number for any point of the working volume, as the length of the link would be shorter than the distance between the actuator and the platform, therefore the system would not be feasible.

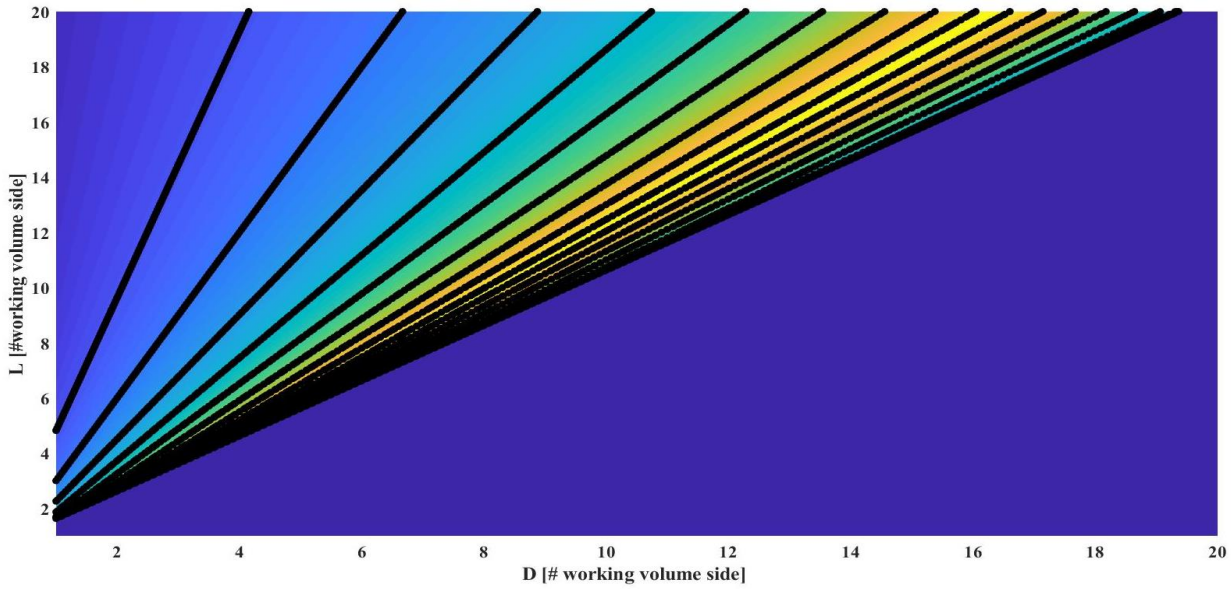

Figure 15: surface colour map plot and contour lines example of the maximum inverse conditioning number inside the working volume with a square horizontal cross section

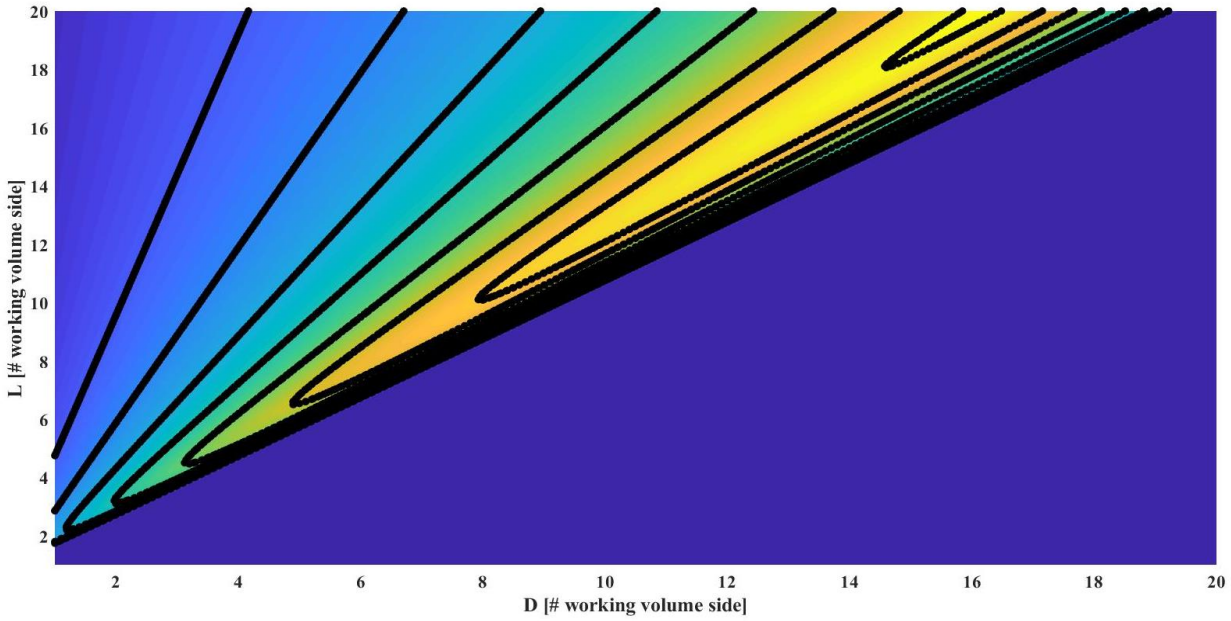

Figure 16: surface colour map plot and contour lines example of the minimum inverse conditioning number inside the working volume with a square horizontal cross section

Figure 17 shows the points extracted from the contour lines of S_{min} with minimum distance from the origin, together with the fitting straight line. To improve the quality of the image, only a set of the minimum distance points was included in the image. Including all the points would have made difficult to see the fitting line, and the image would not have shown significant differences. Equation 2.37 defines the fitting line. The RMSE obtained is equal to 0,10.

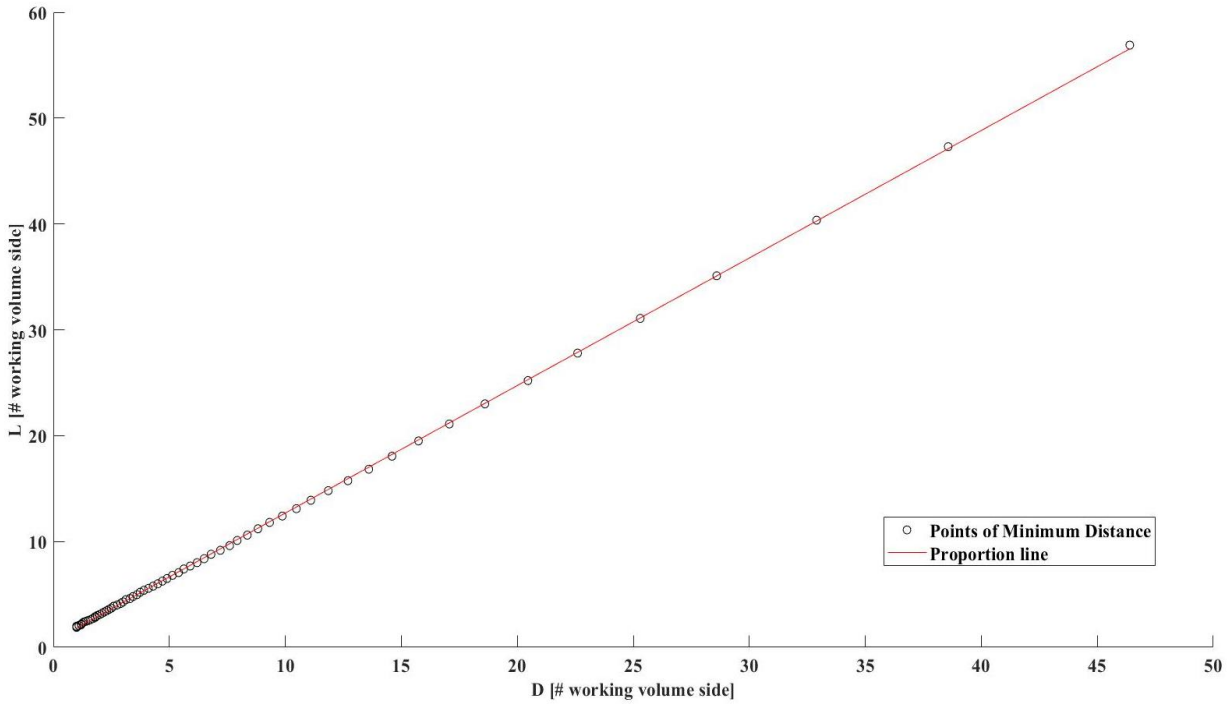

Figure 17: plot of the points extracted from the contour lines of S_{min} with minimum distance from the origin, together with the optimized straight line

$$L = 1{,}205 \cdot D + 0{,}635 \tag{2.37}$$

Figure 18 and Figure 19 show respectively the parameters of the contour line of S_{min} and S_{max} as functions of the associated value of the inverse of the conditioning number. The RMSE obtained through the fitting is given inside each associated plot. For all the parameters it was possible to find a function that leads to an RMSE lower than 0,05 throughout all the points taken into consideration, except for the parameter *f*. For that parameter however the RMSE is equal to 0,018 when considering a minimum conditioning number inside the working volume up to a value of 0,85.

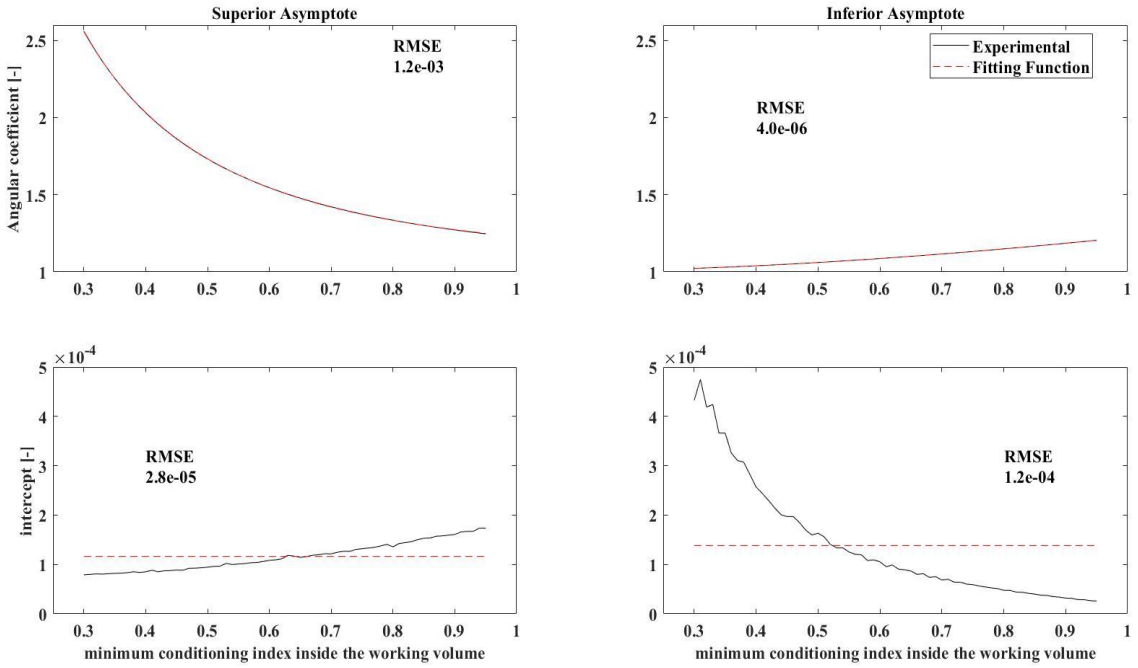

Figure 18: parameters of the contour line of S_{max} as functions of the associated value of the minimum inverse conditioning number inside the working volume

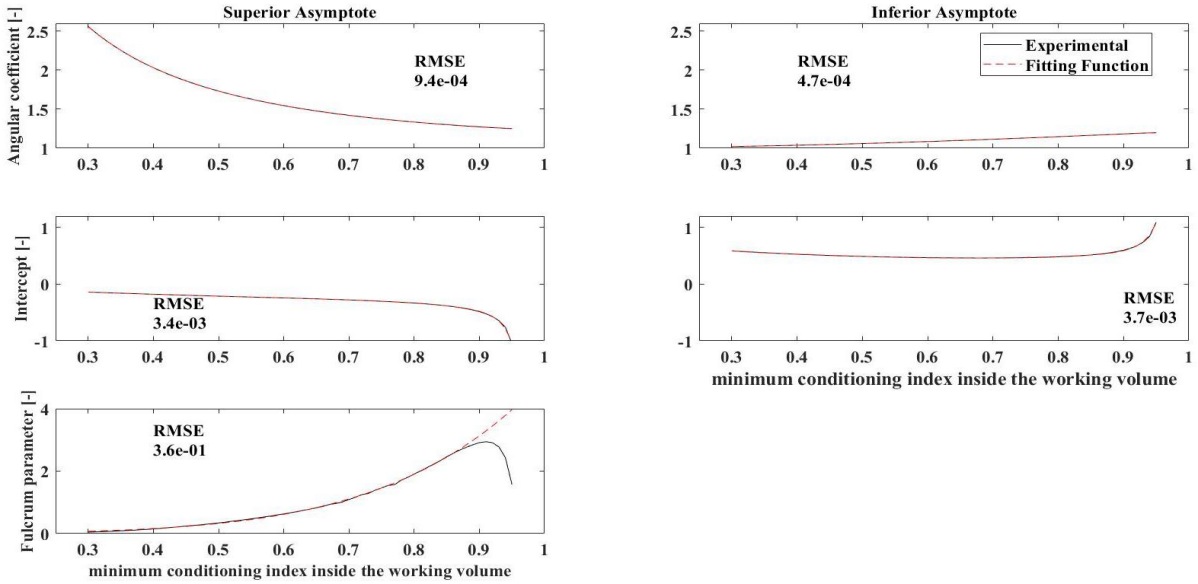

Figure 19: parameters of the contour line of S_{min} as functions of the associated value of the minimum inverse conditioning number inside the working volume

Equations 2.38-2.41 and equations 2.42-2.46 contain respectively the functions used to fit the parameters of the contour line of S_{min} and S_{max} as functions of the associated value of the inverse of the conditioning number.

$$m_{\sup max} = \frac{1{,}868}{e^{2{,}752 \cdot C_{max}} - 1} + 1{,}102 \tag{2.38}$$

$$q_{\sup max} = 1{,}16 \cdot 10^{-4} \tag{2.39}$$

$$m_{\inf max} = -0{,}049 {C_{max}}^3 + 0{,}283 {C_{max}}^2 - 0{,}010 C_{max} + 1{,}001 \tag{2.40}$$

$$q_{\inf max} = 1{,}38 \cdot 10^{-4} \tag{2.41}$$

$$m_{\sup min} = \frac{1{,}912}{e^{2{,}804 \cdot C_{min}} - 1} + 1{,}108 \tag{2.42}$$

$$q_{\sup min} = \frac{\left(7{,}3 \cdot 10^{-5}\right) C_{min}}{(C_{min} - 1)^3} - 0{,}682 {C_{min}}^{0{,}256} - 0{,}251 {C_{min}}^{7{,}756} + 0{,}3612 \tag{2.43}$$

$$m_{\inf min} = -0{,}120 {C_{min}}^3 + 0{,}398 {C_{min}}^2 - 0{,}069 C_{min} + 1{,}001 \tag{2.44}$$

$$q_{\inf min} = \frac{0{,}596}{1 - 2{,}097 {C_{min}}^{38{,}784 C_{min} - 8{,}379}} - 0{,}065 {C_{min}}^{-6{,}534 C_{min} + 2{,}551} \tag{2.45}$$

$$f = (0{,}834 C_{min} + 0{,}431)^{6{,}825} \tag{2.46}$$

Figure 20 shows the abscissa of the points of minimum distance (see Figure 17) as a function of the value of the minimum conditioning number inside the working volume. It was not possible to obtain a function that leads to a fitting of the points with an RMSE lower than 0,05.

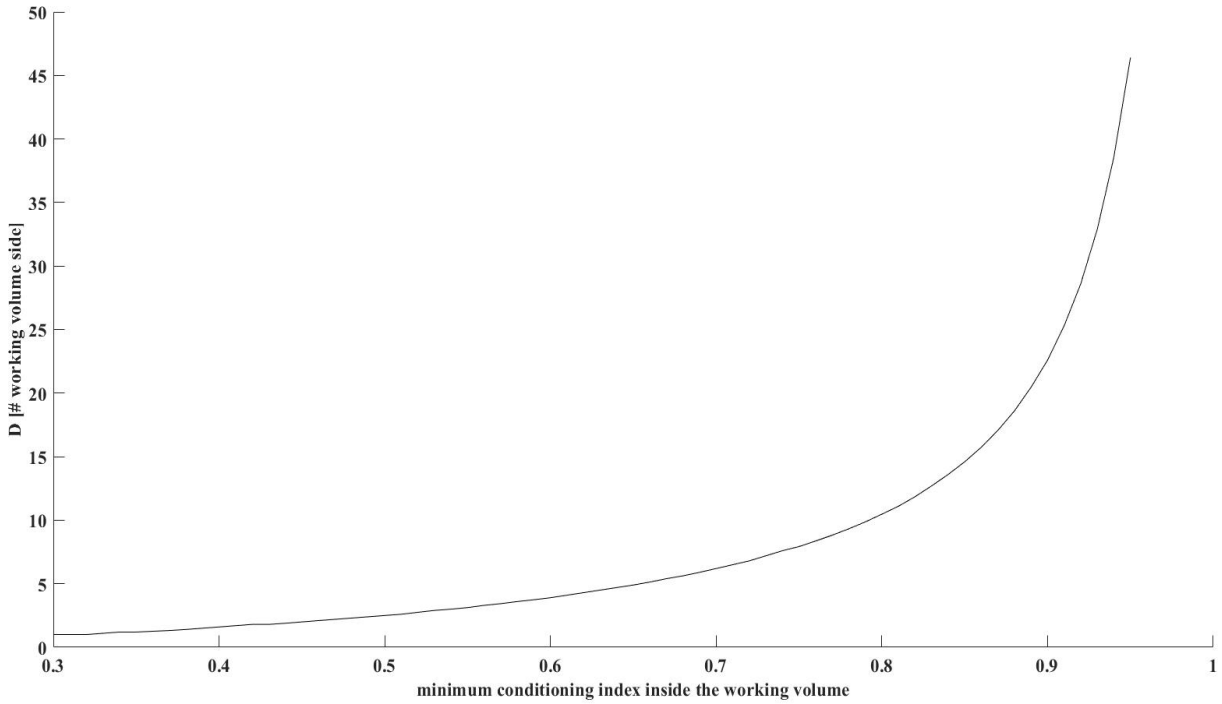

Figure 20: abscissa of the points of minimum distance as a function of the value of the minimum conditioning number inside the working volume

2.1.2.3 Discussion

The results of the fitting process show that it is possible to compute, with an RMSE lower than 0,05; optimized parameters of two family of straight lines that fit the contour lines of surface describing the maximum inverse conditioning number inside the working volume with a square horizontal cross section. Although the fitting of the parameters $q_{sup\ max}$ and $q_{inf\ max}$, in equations 2.38 and 2.41 (Figure 61) do not appear optimal, their RMSE was already lower than 0,05. As a result, the simplest function was chosen. It has been found that the optimized parameter of two families of straight lines can model the contour lines of S_{min} and S_{max}. It is not possible however, to say the same about the parameter *f* as a function of the contour line level itself. In fact, the function used to fit such parameter, shown in equation 2.46, can provide a satisfactory fitting only until a value of minimum inverse conditioning number inside the working volume with a square horizontal cross section equal to 0,85. This does not, however, negate the method proposed. In fact, the trial and error method was used to obtain the fitting functions. With more iterations of such method, it would be possible to obtain a better fitting function. However, a level of 0,85 would already lead to a large size of the design dimensions of the linear delta robot in respect to the working volume, so higher values are not as meaningful. It was decided to show anyway the plot until the 0,95 level to enable the reader to estimate the parameter f directly from the figure, in case high levels of kinematic performances are

required. The interpolation of the abscissa of the points of minimum distance as a function of the value of the minimum conditioning number inside the working volume failed, however it is still possible to obtain useful information from this method, and propose another method, simpler than the one already proposed, to obtain simple constraints for an optimization process. This is due to the fact that all the kinematic performance indexes themselves are not a perfect measure of the overall performances of a robot, as explained by Olds [64]. For this reason, it may not be useful to impose strict boundaries based both on C_{min} and C_{max}, but it would be useful to impose a lower bound only on C_{min}. To do so, given a desired C^*_{min} it is possible to compute $q_{sup\ min}$, $q_{inf\ min,}$ $m_{sup\ min}$ and $m_{inf\ min}$ as before, and it is also possible to estimate D* from Figure 20. Known D*, L* can be computed using equation 16. In this way, the surface between the two straight lines and the lines $D \geq D^*$ and $L \geq L^*$ provides an estimate of the surface in which $C_{min} \geq C^*_{min}$.

Finally, equation 2.37 can be used to simplify the optimization process by effectively deleting one optimization variable. This may be useful when there are no direct constraints on the kinematic performances of the robot, and the interest is on other objective functions. In this case, it is possible to use equation 2.37 to both simplify the optimization process and still take indirectly into account the kinematic performances, as it is defined as the equation for which the coordinates of its points lead to the smallest dimensions given a minimum inverse of conditioning number inside the working volume.

The parameters described are limited by the fact that the section along the horizontal plane of the workspace must be a square. This decision was made for two reasons. The first is to maintain continuity with the selection of the size of the delta shaker, as the method described in this chapter is effectively a generalization of the method described previously. The second reason is that the workspace of most industrial machines able to operate in the three dimensions is defined through the maximum displacement possible along the three perpendicular spatial axes. The method explained to obtain the equations however can be generalized too, being numeric. If needed the same steps can be implemented again with a different definition of the horizontal section of the workspace, in which to compute the inverse of the conditioning number. As already explained, some authors provide evidence that the inverse of the conditioning number is a rough estimate of the kinematic performances of a robot. That index was selected for continuity with what was already done for the design of the shaker, as an example for this method. If other indexes are found to be more accurate, or are more relevant for a given application, this method can be still valid, as it only requires changing one computation. The major limit of this method is the selection of the proper fitting functions of the

parameters defining the family of curves. This process is crucial to the final good fitting of the contour lines, and it is not guaranteed to lead to satisfying results, as it was proven here.

2.2 Dynamic analysis and actuators selection

After the size optimization, it was possible to estimate the forces required for the movement of the platform. To do so, a simplified model of the linear delta robot was created in the multibody dynamic simulation software Adams (MSC Software, 4675 MacArthur Court, Newport Beach, CA 92660). The model included only the moving parts, whose geometries were simplified. A vertical translation joint was used to model the actuation variables, and revolute joints were used to model the connections at the ends of the links. The mass of the moving platform was estimated in 20 kg. An additional mass of 200 kg was added to represent the payload, i.e. a person standing on the platform. This value represents the apparent mass of a person, whose static mass is 100 kg, along the vertical direction at the resonance frequency of 6 Hz [74]. Since the objective of the machine is to generate an excitation signal for the estimation of the full matrix of apparent mass of a standing person, a pseudo-random signal with flat spectrum was selected as the signal kind to be used. The signal was created by summing simple sinusoidal signals with the same amplitude and random phase. The frequency step of the sine waves is equal to the inverse of the desired duration of the signal, so that the numerical computation of the spectrum of the signals would lead to a continuous and flat function. The resulting signal is then divided by its own RMS value and multiplied by the desired effective value. Given the random nature of this signals, 25 different sets of signals were created, each set was composed of a different signal for the three directions of motion. The duration of each signal was 2 s, and the frequencies varied from 0,5 Hz to 30 Hz. The amplitude of each component of the signals was set to 10 m/s^2 divided by the number of harmonics. The signal imposed along the vertical direction was further increased by 50%, as the vertical dimension of the working volume is 50% higher than the horizontal dimensions. Each set of acceleration signals numerically integrated two times to obtain the time histories of the position of the moving platform. This step did not introduce a drift in the time histories of speed and position thank to the way in which the signal was created. In fact, all the harmonics which were summed to compose the signals have a frequency which is an integer multiple of the inverse of the time window. Thus, an integer number of periods is considered, resulting in a signal with average equal to 0. The inverse kinematic of the linear delta robot allowed the computation of the positions of the three linear actuators as a function of time. These values were then fed into the multibody dynamic model, which gave the time histories of the three actuation forces, and of the constraints reactions as output. Table 3 shows the maximum values computed across all three actuators. Such values were used as reference values for the dimensioning of the motor and

reduction of the robot, together with the maximum RMS value of the actuation force, which was 955 N.

Table 3: maximum forces and moments at the joints, computed through the multibody dynamic simulation, across all three actuators

Fx [N]	Fy [N]	Fz [N]	Mx [Nm]	My [Nm]	Mz [Nm]
1916	1908	282	148	181	320

Given the need for a transmission with no backlash, high stiffness and precision, a direct coupling of an electric motor and a preloaded ball screw was selected. The electric motor was selected from the catalogue of Omron Electronics S.p.A. (Shiokoji Horikawa, Shimogyo-ku, Kyoto, Japan), while the ball screw was selected from the catalogue of Rollon S.p.A. (Via Trieste, 26, 20871 Vimercate MB, Italia). The possible couples of motors and transmission that could satisfy the forces computed through the multibody dynamic software were selected through the α-β method, as explained in [72], [75]. The final selection was done by computing which couple could provide the highest instantaneous vertical acceleration to the moving platform. Such acceleration can be computed through the balance of the forces acting on the platform, the results are shown in Equation 2.47:

$$A = \frac{2\pi \cdot T_{max} - p \cdot M \cdot g}{p\left(J_s \cdot \left(\frac{2\pi}{p}\right)^2 + M\right)} \tag{2.47}$$

T_{max} is the maximum instantaneous torque that the motor can provide, p is the pitch of the ball screw, J_s is the total inertia of the rotating parts, g is the acceleration of gravity and M is the total translating mass divided by three, under the hypothesis that the load is shared equally between all the actuators. The inertia of the rotating part is the sum of the inertia of the motor, the screw, which is modelled as a cylinder, and the inertia of the joint between the two. The joint that was selected is the model smartflex® 1/932.333 manufactured by Mayr® (Eichenstraße 1D-87665 Mauerstetten, Germany) which has a mass moment of inertia of $1.04 \cdot 10^{-4}$ kg·m^2. The total translating mass is the sum of the mass of the payload, the mass of the translating parts of the shaker, which was increased to 32 kg, plus the mass of the translating part of the screw. The final outcome of this selection procedure was the couple composed of the servomotor R88M-1M3K020C-400V and the ball screw TV-110-32-32. The selected servomotor is a brushless motor with a nominal power output of 3000 W, a nominal torque output equal to 28,7 Nm. The rotor moment of inertia, for the model with brakes is $7{,}31 \cdot 10^{-3}$

kg·m^2. The nominal rotational speed is 1000 rpm. The nominal mass is 15 kg. Table 4 contains the nominal parameters of the motor, while Figure 21 shows the parametric draft of the motor.

Table 4: nominal parameters of the brushless motor R88M-1M3K020C-400V produced by Omron (dimensions in mm)

LL	KB1	KB2	KL1	KL2	LR	S	Q	QA	QK	W	U	T	Tap x depth
234	118	219	45	119	65	24	60	3	52	8	3	7	M8 x 20 L

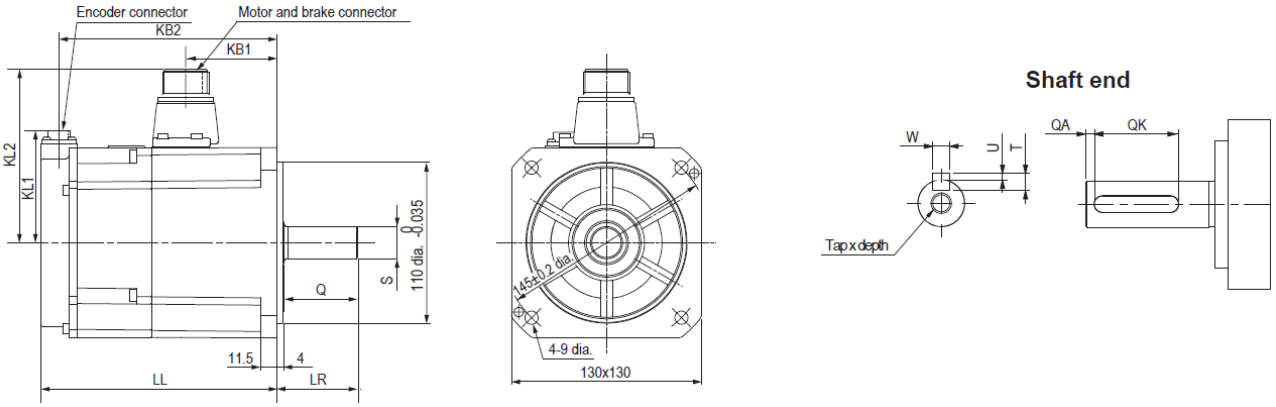

Figure 21: parametric draft of the brushless motor R88M-1M3K020C-400V produced by Omron

The selected ball screw assembly contains a ball screw with a nominal diameter of 32 mm and the pitch equal to 32 mm. The stroke of the actuator was 200 mm. The nominal mass is 20,6 kg. Figure 22 shows the parametric draft of the ball screw assembly.

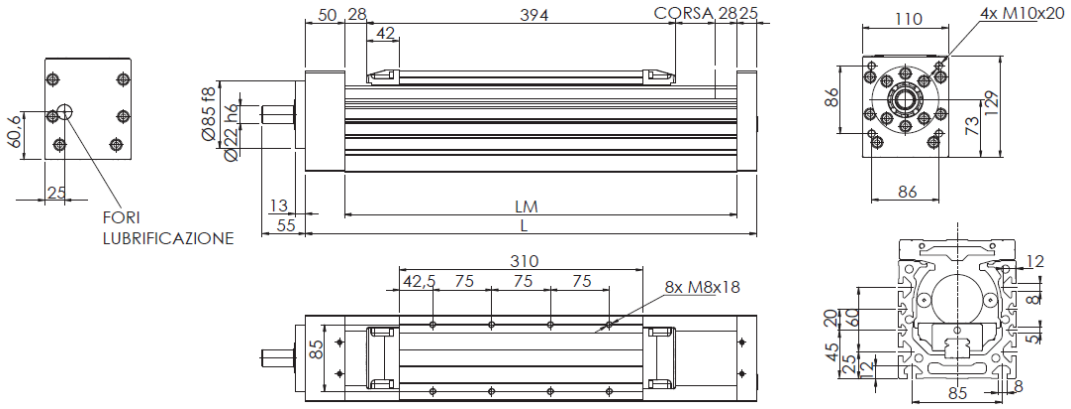

Figure 22: parametric draft of the ball screw assembly TV-110-32-32 produced by Rollon (dimensions in mm)

2.3 Structural design and optimization

With the constraints deriving from the selection of sizes, motors and ball screws, it was possible to design the components of the linear delta robot. Figure 23 shows the whole assembly. This section contains a detailed description of all the components, while Annex 1 contains all the produced drafts.

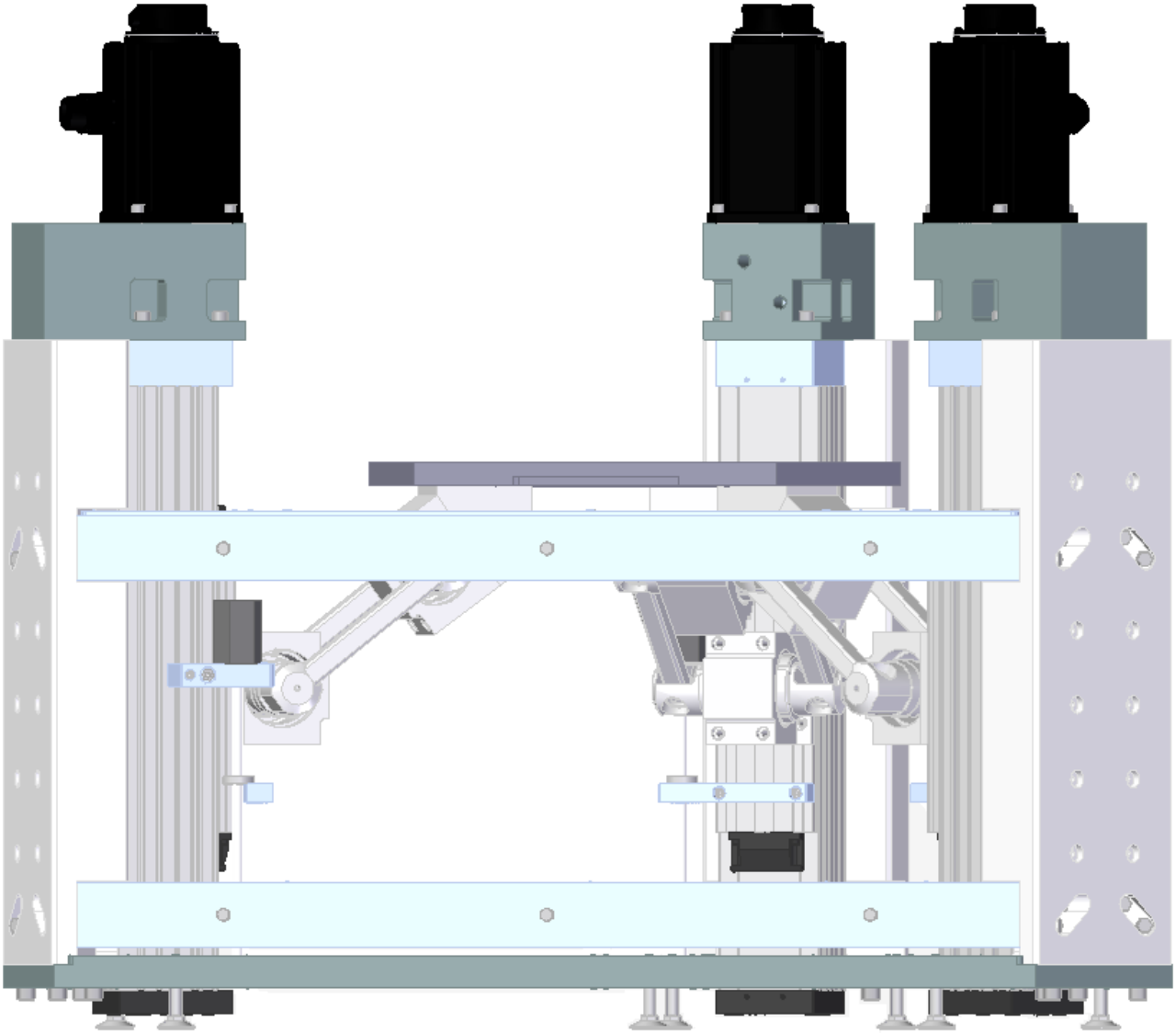

Figure 23: CAD drawing of the assembly of the Linear Delta Robot

Moving parts were designed to ensure the transmission of motion with a high stiffness and no backlash; however, their mass must be minimized, to not decrease the dynamic performance of the robot.

The vibrating platform was the first component to be designed. To obtain the best result, different concurrent parameters had to be optimized, from the geometry, to the material, to the production process. To reduce the complexity of the problem, some of those parameters were set from the start. It was decided to mill the component out of an aluminium plate. The thickness of the plate was 25 mm; the dimension was selected after an optimization process described in [76]. The mass was reduced by cutting stiffening ribs out of the stock material. The optimal thickness of the ribs was

20 mm. Three additional parameters were left to optimize: the shape of the plate, the geometry of the stiffening ribs and their thickness. Two shapes, called Configuration 1 and Configuration 2, were compared. Figure 24 shows such shapes.

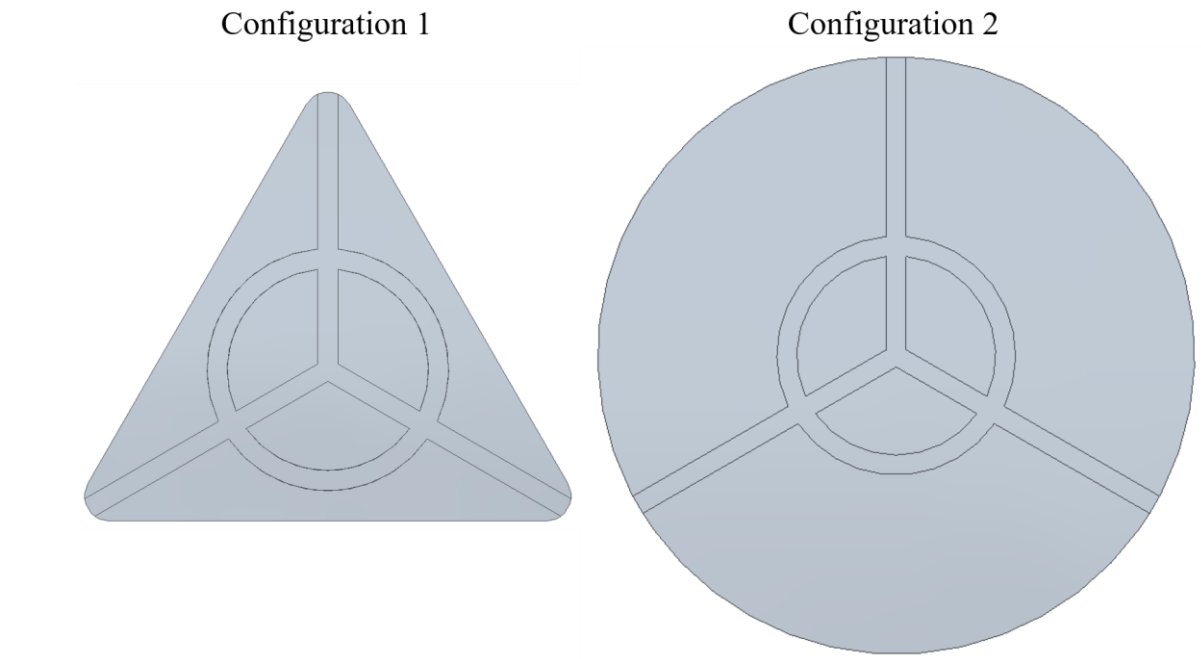

Figure 24: comparison between the two shapes compared for the moving platform of the delta shaker

The selection of the depth of the ribs and of the shape was done by comparing the resulting mass and stiffness, for both shapes, at different depth values. The stiffness of the plate was evaluated by computing, with the aid of a FEM model, its first natural frequency, under the hypothesis that a person is standing on it. The action of the person, at this point, was modelled as a force of 800 N distributed into two rectangular surfaces on the platform, with dimensions of 250x150 mm, simulating the feet.

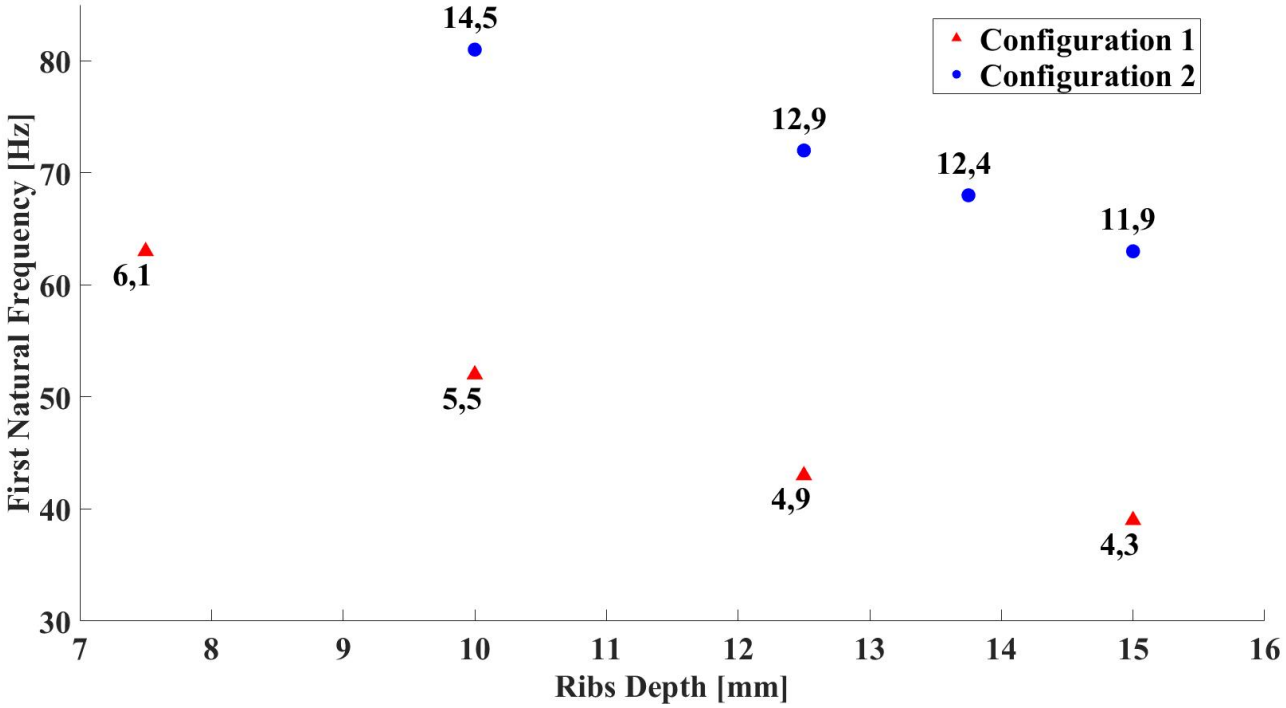

Figure 25: comparison between the first natural frequencies obtained with different rib depth on a circular and triangular platform. The mass of each solution, expressed in kg, is shown close to each point in the plot

Figure 25 shows that Configuration 2 provides a higher first natural frequency than Configuration 1, at a cost of a higher mass. For example, the frequency of 63 Hz can be obtained either with Configuration 2 having a mass of 11.9 Kg, or with Configuration 1 with mass equal to 6 kg, reflecting a 50% mass decrease. These results show that it is better to employ a shape closer to Configuration 1, given the resulting mass reduction. The final design was then obtained through a trial and error method. Figure 26A and Figure 26B show the CAD drawing of lower and upper sides of the optimized plate. A total of twelve through holes a1) allow the connection of the moving plate with the three cardan joints, through M8 screws. Six centring pins, inserted into the b1) holes, guarantee the alignment of the moving platform with the cardan joints. The through holes pattern c1) is equal to the hole pattern of the electrodynamic shaker model V830 produced by LDS (Baldock Road, Royston, UK), already available in the laboratory. This pattern would allow the same fixturing systems to be used on both machines. The ribs pattern d1) is milled on the bottom of the platform to decrease the mass of the moving platform, while maintaining a high stiffness.

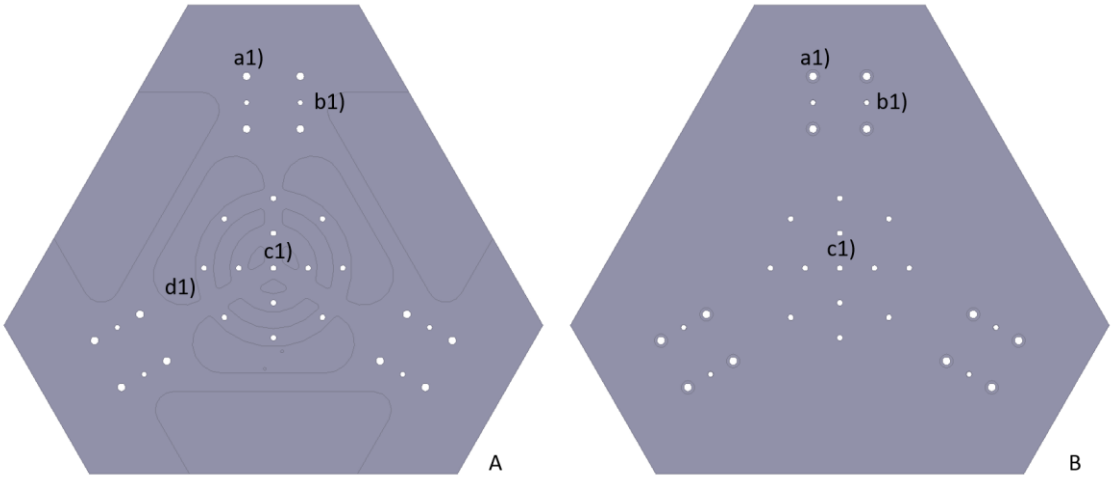

Figure 26: CAD drawing of the moving plate of the proposed shaker

The moving platform is connected to the rest of the shaker through three connection wedges, shown in Figure 27. The holes a2) and b2) correspond to the holes a1) and b1) of the moving platform (Figure 26). The holes allow the connection and the alignment between these two elements. The pocket c2) allows the reduction of the wedge mass. Four M8 threaded holes d2) allow the connection of the wedge with the cardan joint. Two holes e2) house the centring pins that align the wedge with the cardan joint.

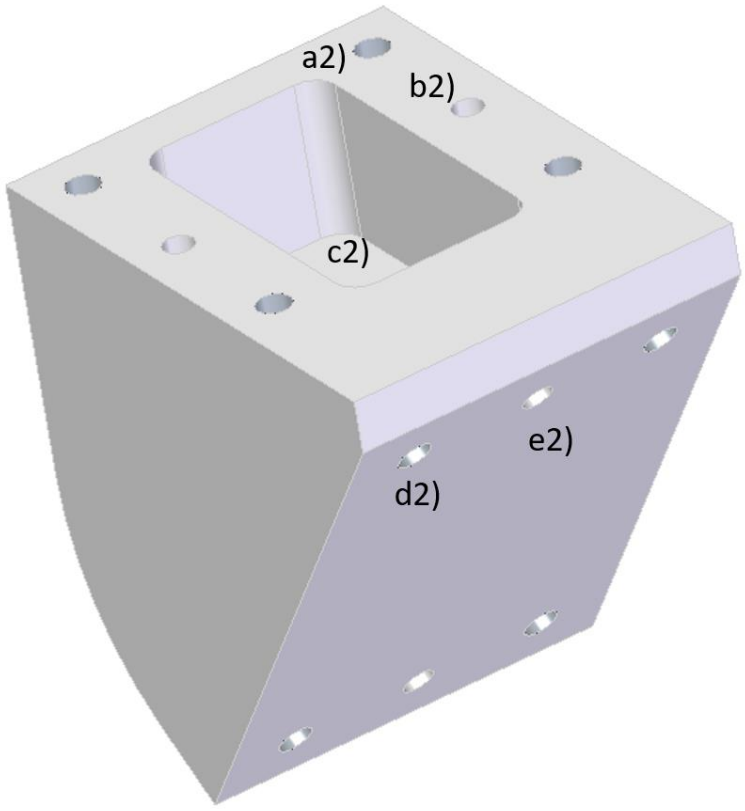

Figure 27: CAD drawing of the wedge connecting the moving platform to the cardan joint of the proposed shaker

To reduce even further the inertia of the moving parts, a new platform has been designed with a sandwich structure, having an aluminium honeycomb core 25 mm thick and skins made from 8 layers of carbon fibres fabric. The expected to mass of new platform is 2,4 kg. The new platform, currently under production, will replace both the existing platform and the connection wedges, for a total mass reduction of 14,4 kg. Figure 28 shows the CAD drawing of the new version of the moving platform.

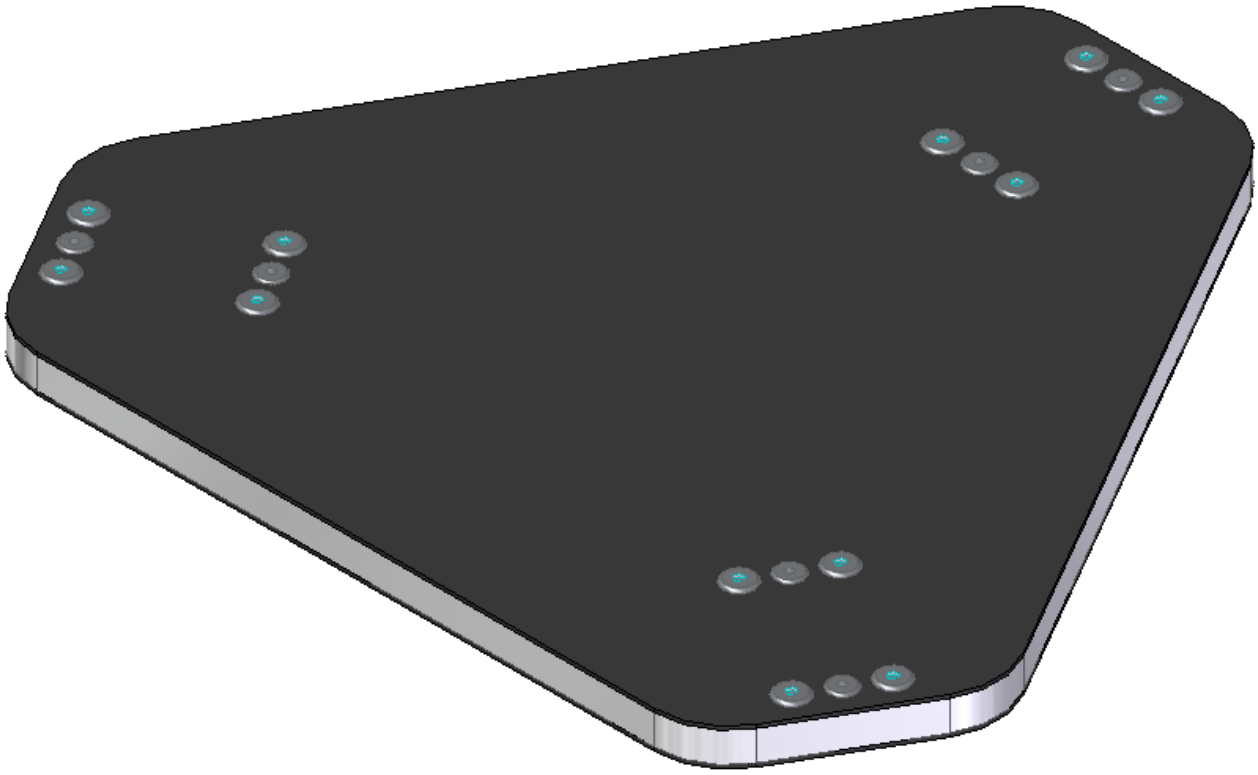

Figure 28: CAD drawing of the improved lightweight platform

To fulfil the requirements of high stiffness and zero backlash, a cardan joint was designed specifically for this application. The focal point of the cardan joint is the use of two couples of angular-contact ball bearings, allowing the rotation of the links, and another couple of angular contact ball bearing, whose axis of rotation is rotated 90° in respect to the axis of rotation of the other two couples of ball bearings. To avoid the backlash and maximize the stiffness, the couples of ball bearings are placed in an “O” configuration and tightened with screws.

The starting point was the selection of the ball bearing allowing the rotation of the links. The angular contact ball bearing with the smallest outer diameter in the SKF (SE-415 50 Göteborg, Sweden) catalogue was selected for this application. Another shaft, in fact, must contain in its cross section the cross sections of those two ball bearings and the cross section of the links. Thus, minimizing the size

of the ball bearings means minimizing the size, and the mass, of the whole cardan joint. The model of angular contact ball bearing selected is the BEP 7200. Table 5 contains the design parameters of that component; Figure 29 contains the reference technical draft.

Table 5: design parameters of the angular contact ball bearing BEP 7200

d	10 mm
D	30 mm
C	7.02 kN
C0	3.35 kN
e	1.14
Y0	0.52
Y1	0.55
B	9 mm

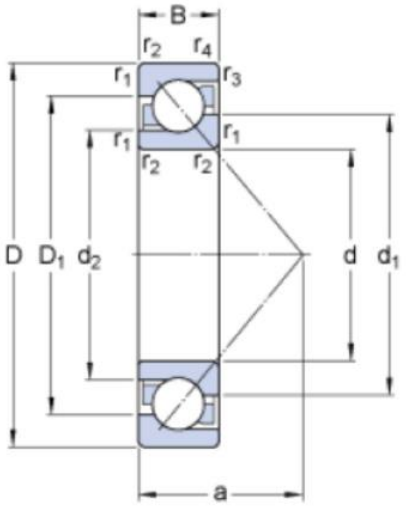

Figure 29: parametric draft of the angular contact ball bearing provided by SKF

According to the already mentioned multibody simulation, the maximum axial force acting on the link is 3,70 kN. The equivalent dynamic and static load acting on the bearings have been computed according to the prescriptions of the manufacturer. It was hypothesised that both ball bearings share equally the axial force of the link in the radial direction, and that the axial force on the bearings generated by the preload is small. Since the ratio between the load acting on the axial direction and the load acting on the radial direction of the ball bearing is lower than the parameter “e”, it is possible to estimate the equivalent dynamic load as the load acting along the radial direction. Thus, the equivalent dynamic load estimated for this ball bearing is equal to 1,85 kN; which is 3,8 times smaller than the maximum equivalent dynamic load. The static load acting on the angular contact ball bearing can be estimated according to equation 2.48:

$$P_0 = 0{,}5 \cdot F_r + Y_0 \cdot F_a \quad (2.48)$$

Where P_0 is the equivalent static load acting on the angular contact ball bearing, F_r is the load acting on the ball bearing along the radial direction; F_a is the load acting on the ball bearing along the axial direction and Y_0 is the design parameter specific for that component, as shown in Table 5. The equivalent static load acting on the angular contact ball bearing is then 0,93 kN; 1,8 times lower than the maximum value allowed.

The main constraint on the second kind of ball bearing is the diameter of the inner ring equal to 60 mm. An angular contact ball bearing satisfying that constraint was the model BEP 7212. However, that model has an outer diameter of 110 mm, and a mass of 0,8 kg. To reduce the mass and to decrease the size of the other components, the tapered roller bearing having an inner diameter of 60 mm was selected (model 32912). The outer diameter is 85 mm and the mass 0,3 kg.

Table 6: design parameters of the tapered roller bearing 32912

d	60 mm
D	85 mm
C	53 kN
C0	75 kN
e	0.33
Y0	1
Y1	1.8
B	17 mm

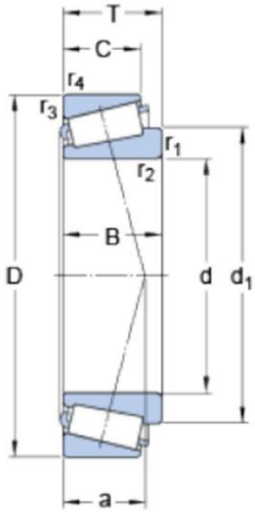

Figure 30: parametric draft of the tapered roller bearing provided by SKF

According to the multibody dynamic simulation, the maximum force acting on the cardan joint along the radial direction (F_r) of the tapered roller bearing is 3,78 kN, while the maximum force acting along

the axial direction (F_a) is equal to 0,34 kN. The symmetry condition allows supposing that both bearings share F_r equally, while F_a is acting only along one bearing, due to their arrangement. The equivalent dynamic load can be estimated as the force acting along the radial direction, as the ratio between the force acting along the axial direction and the force acting along the radial direction is lower than the parameter "e". The resulting equivalent dynamic load is then equal to 1,89 kN. The maximum equivalent dynamic load for which this bearing is rated is equal to 53 kN. Equation 2.48 allows the computation of the equivalent static load. The result for this bearing is equal to 1,85 kN. The maximum equivalent static load for which this component is rated is equal to 75 kN.

After selecting the bearings, it was possible to design the mechanical components of the cardan joint. To improve the understanding of the cardan joint assembly, Figure 31 shows the 3-D CAD drawing of that element of the machine, Figure 32 and Figure 33 show the cross-section views of the details.

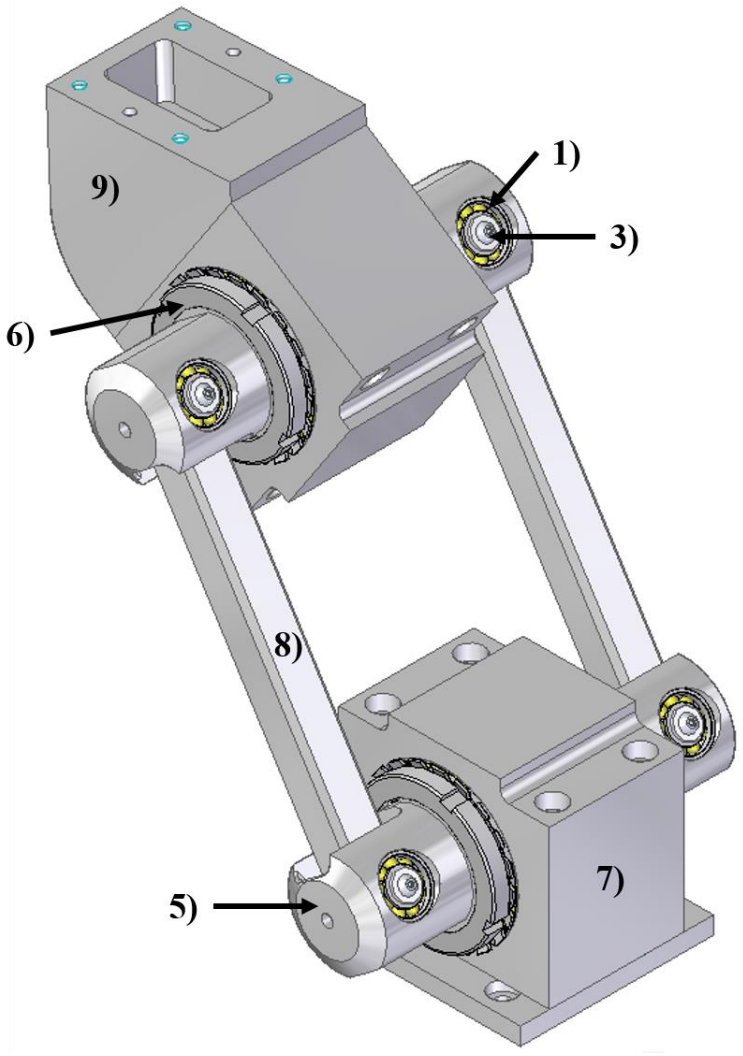

Figure 31: 3-D view of the cardan joint assembly of the Linear Delta Robot

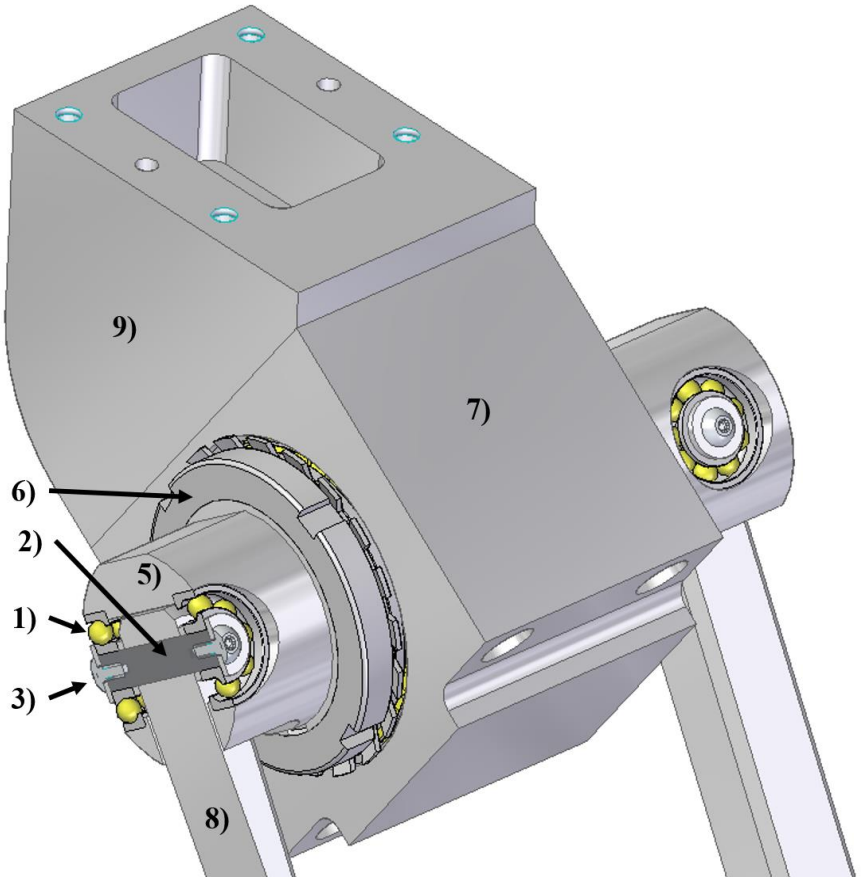

Figure 32: Cross section view of the angular contact ball bearing BEP 7200 inside the cardan joint

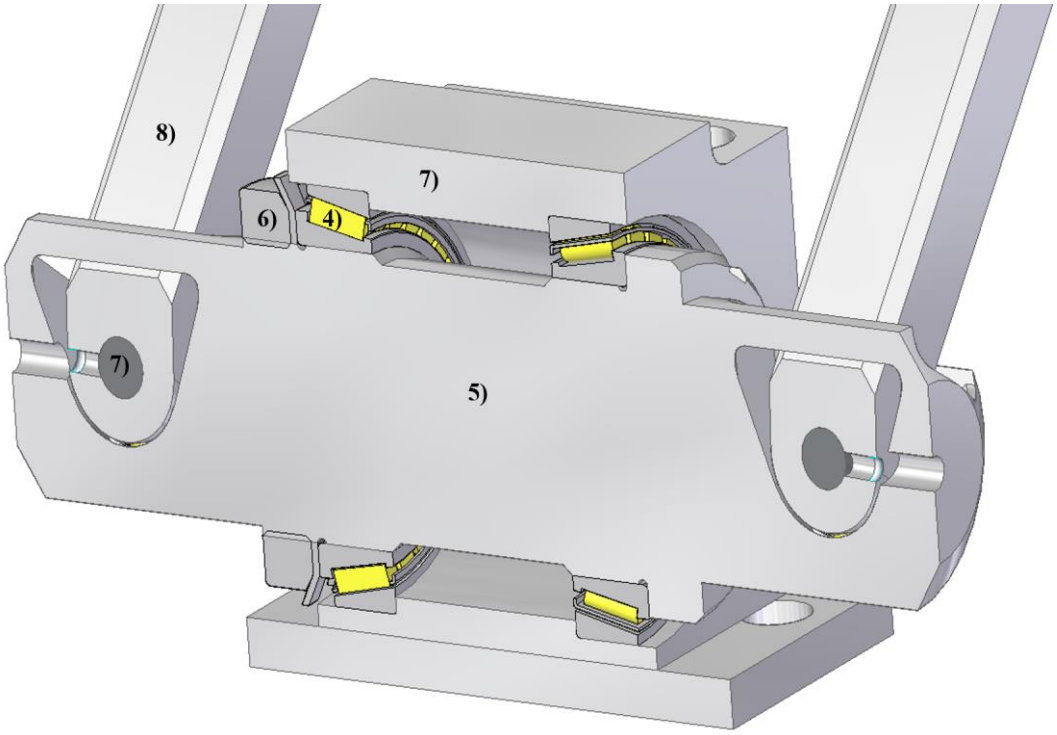

Figure 33: Cross section view of the tapered roller bearing 32912 inside the cardan joint

List of elements shown in Figure 31, Figure 32 and Figure 33:

1) Angular contact ball bearing BEP 7200
2) Shaft of angular contact ball bearing BEP 7200
3) Tightening nut for the shaft of angular contact ball bearing BEP 7200
4) Tapered roller bearings 32912
5) Shaft of tapered roller bearings 32912, with milled housings for angular contact ball bearing BEP 7200
6) Lock nut model KM 12 for the shaft of tapered roller bearings 32912, with lock washer MB 12
7) Housing for the tapered roller bearings 32912
8) Link of the Linear Delta Robot
9) Wedge connecting the cardan joint and moving platform

Figure 34A and Figure 34B show two views of the CAD drawing of the Housing for the Angular contact ball bearing 32912 of the proposed shaker. The through holes a3) and the holes b3) allow respectively the connection of this element with the rest of the machine, and correspond to the d2) and e2) holes of the wedge shown in Figure 27. The step c3) reduces the mass of this element. The hole d3) allows the insertion of the main shaft of the cardan join assembly. The step blocks the outer

ring of the angular contact ball bearing 32912 along the axial direction, allowing the application of the preload.

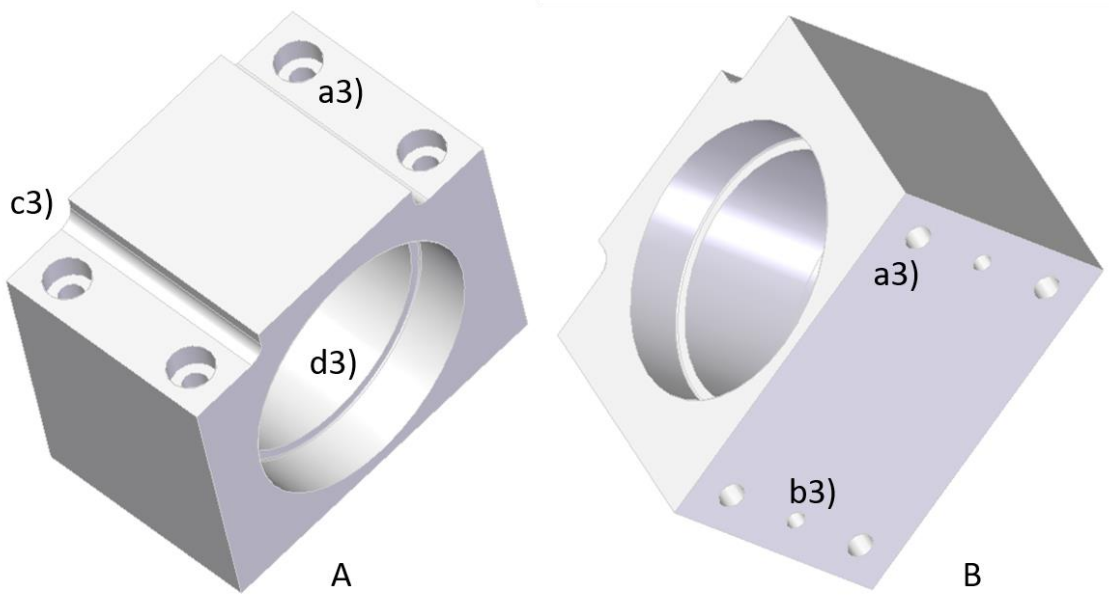

Figure 34: CAD drawing of the housing for the tapered roller bearings BEP 32912 of the proposed shaker

Figure 35 shows the drawing of the shaft of the tapered roller bearings 32912, with the housing for the angular contact ball bearing BEP 7200 of the proposed shaker. The inner ring of the tapered roller bearings 32912 is in contact with the surface a4). This component was anodized to increase its surface hardness, so to decrease the risk of damaging the surface a10) when mounting the tapered roller bearing. The threaded surface b4), coupled with a lock nut model KM 12, lock the outer rings of the tapered roller bearings 32912, allowing the application of the preload. The milled pocket c4) contains the inner tab of the lock washer MB 12, blocking the rotation of that component in the axial direction. One of the outer tabs of the lock washer MB 12 engages one of the grooves on the lock nut model KM 12, preventing the unscrewing of that component. The ring d4) has the same function of the lock nut model KM 12, as it engages the outer ring of the tapered roller bearings 32912. This feature increases the manufacturing time of this component, as it milled from a single piece. However, it offers a fixed reference for the assembly along the axial direction of the shaft, thus allowing a precise and repeatable assembly process. The holes e4) guarantee the access to the grub screw locking the links to their shaft. The links can rotate in the volume f4), of a maximum and minimum angle of ±22,5°. The holes g4) house the angular contact ball bearings BEP 7200. The step engages the outer ring of the angular contact ball bearing, allowing the application of the preload also on that component.

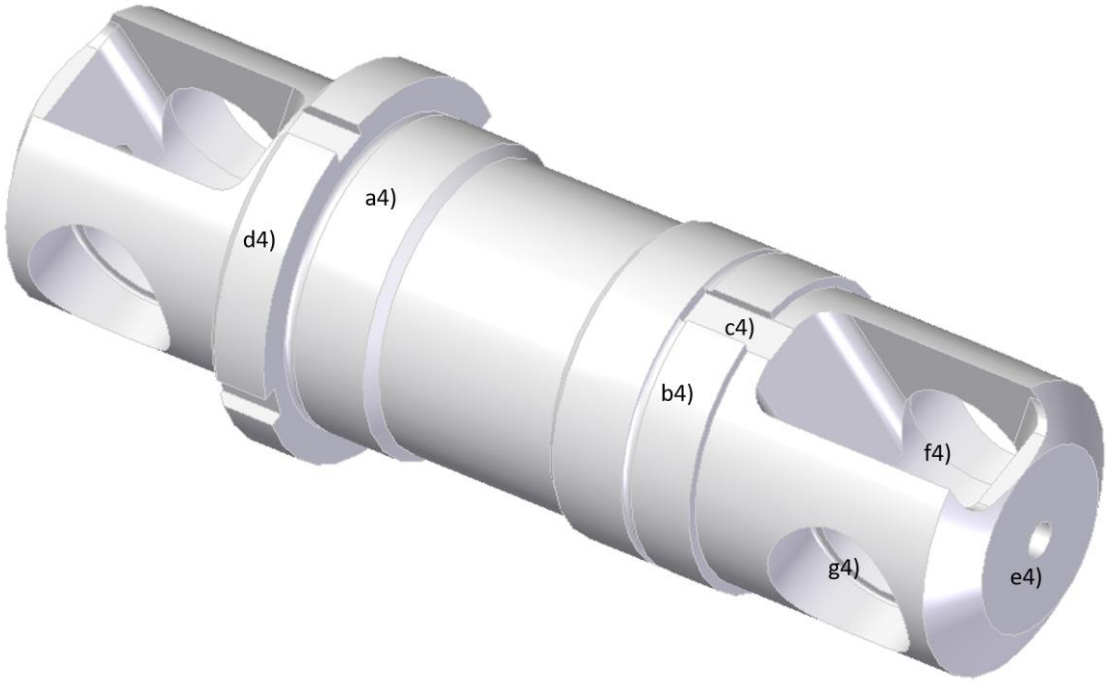

Figure 35: CAD drawing of the shaft of the tapered roller bearings 32912, with the housing for the angular contact ball bearing BEP 7200 of the proposed shaker

Figure 36 shows the CAD drawing of the link of the proposed shaker. A square cross-section allows the production of this component from a standard rod on a mill, easing the process. The two holes a5) connect the link to their shafts. A grub screw is used to lock the link with the shaft, through the threaded hole b5).

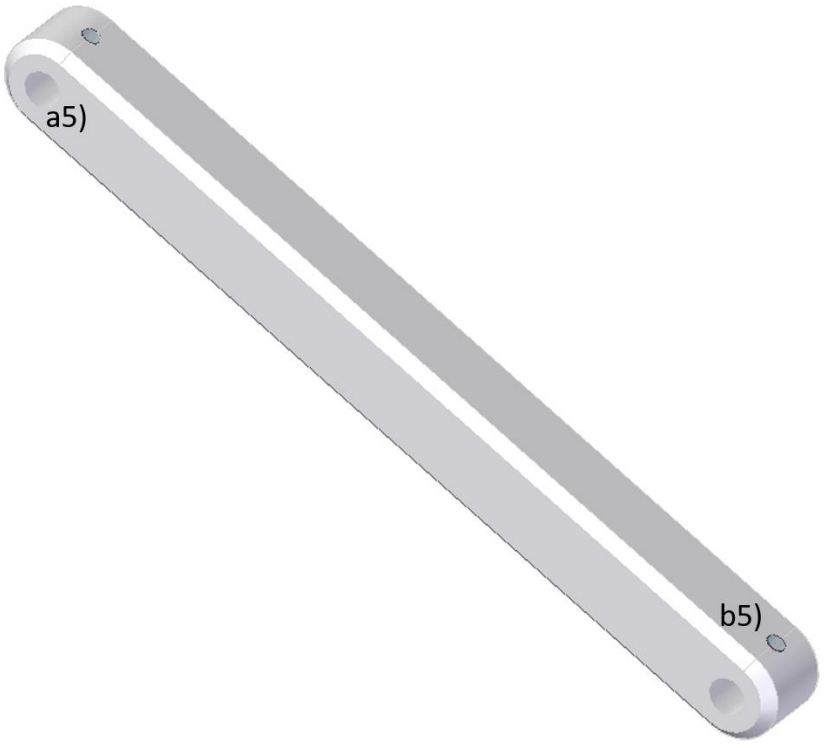

Figure 36: CAD drawing of the link of the proposed shaker

Figure 37 shows the CAD drawing of the plate connecting the ball screw assembly to the cardan joint. The four through holes patter a6) allow to connect the plate to the corresponding threaded holes on the end effector of the ball screw. The four threaded holes b6) allow the tightening of the housing for the tapered roller bearings to the plate. The holes c6) contains the centring pins, which ensure the alignment of the parts.

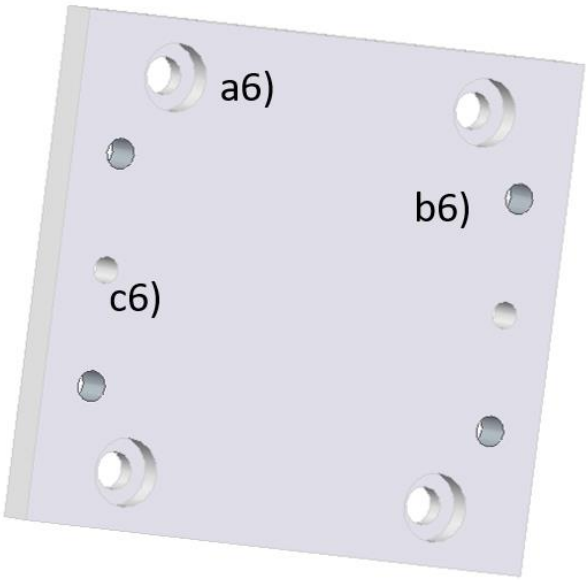

Figure 37: CAD drawing of the plate connecting the ball screw assembly to the cardan joint

The drawings for the static components were then prepared with the objectives of high stiffness and ease of manufacturing, as their only function is to hold together the frame of the robot. Figure 38 to Figure 41 show the static components drawn for this application.

Figure 38 shows the CAD drawing of the base plate of the proposed shaker. This component was cut from a steel sheet with a thickness of 25 mm. Seven adjustable feet, model GN.12004, produced by ELESA S.p.a. (Via Pompei 29, Monza, Italy) support the machine, and are connected to the base plate through the threaded holes a7). Being adjustable, the feet are also used to correct for irregularities in the floor and level the base plate. The through holes b7) are used to connect the base plate and the vertical columns holding the ball screws assemblies, through four M10 screws. The holes c7) ensure the alignment of the connection between the base and the vertical columns, as they are cut to hold a cantering pin. The pocket d7) allow to reduce the distance between the moving platform and the ground. The threaded holes pattern e7) can be used as anchoring point for instruments that may be needed for future tests under the moving platform.

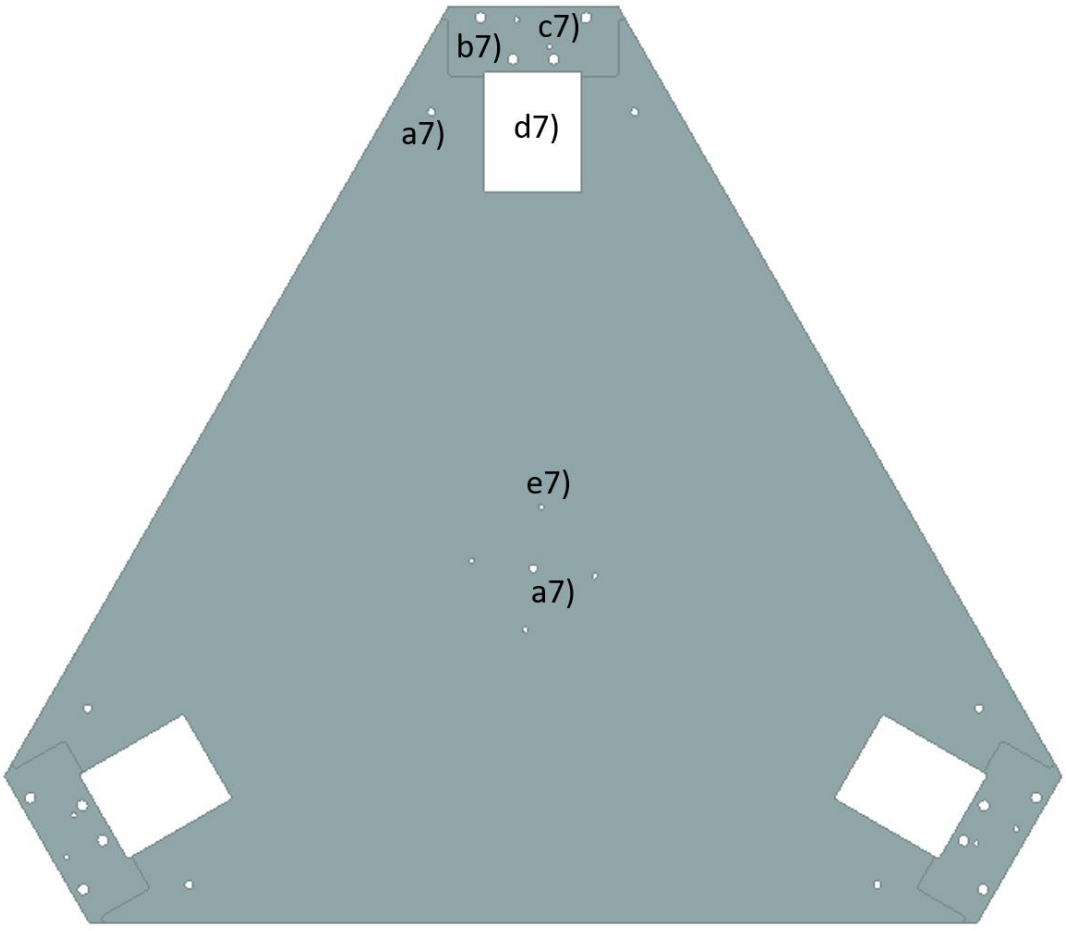

Figure 38: CAD drawing of the base plate of the proposed shaker

Figure 39A and Figure 39B show the CAD drawing of the vertical columns holding the ball screw assembly of the proposed shaker. This component, as all the other ones to be shown, was machined out of aluminium AA7075, to ease the manufacturing process. The size of the component itself ensure a high stiffness. The through holes a8) allow the connection between the column and the ball screw assembly, through ten M6 screws. The through holes b8) allow the connection between the vertical columns and the horizontal stiffening bars, through two M8 screws. The threaded holes c8) allow the connection of the vertical columns with the cube holding the electrical motors and the ball screws assembly. This triple anchorage improves the stiffness of the system, with respect to the standard layout in which that element is connected only to the ball screws and the motors. The holes d8) and e8) correspond to the holes b7) and c7) of the base platform (as per Figure 38).

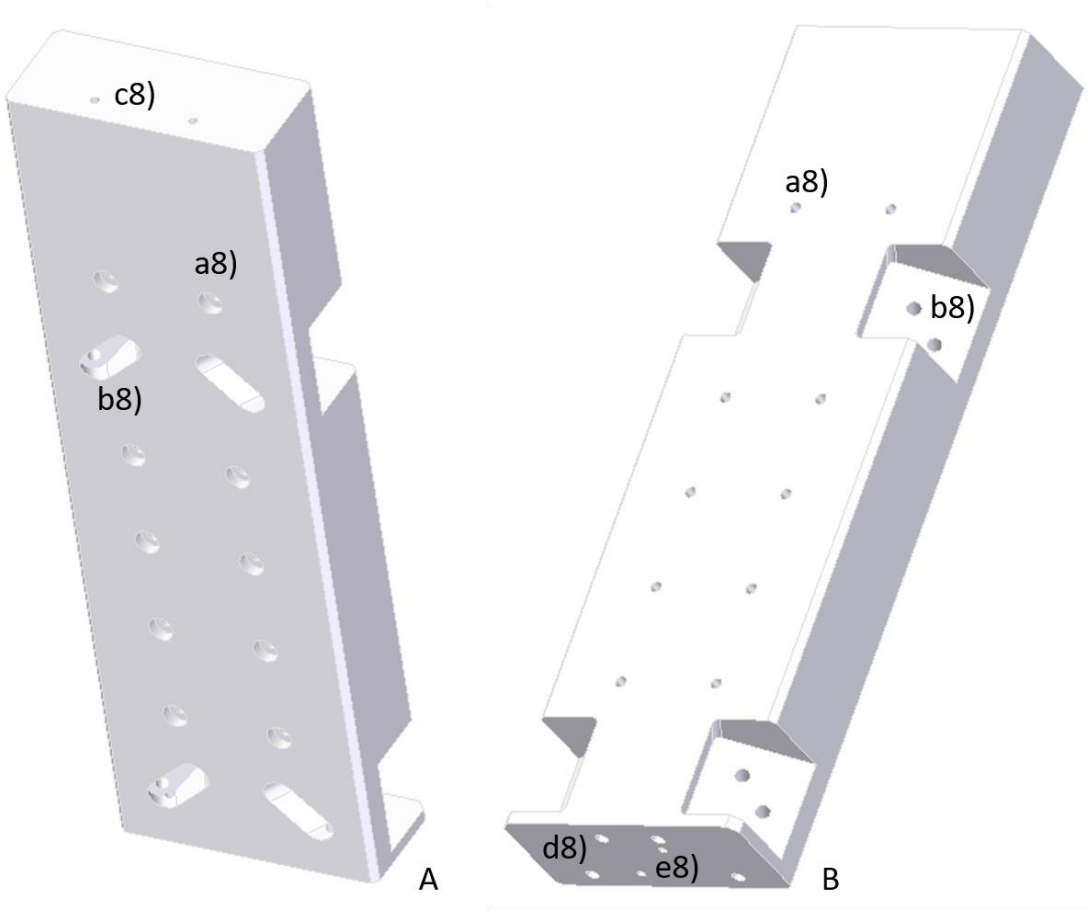

Figure 39: CAD drawing of the vertical columns holding the ball screw assembly of the proposed shaker

Figure 40 shows the CAD drawing of the cube connecting the ball screw assembly and the electrical motors of the proposed shaker. The hole a9) allows the space for the shafts of the ball screws and the motors, and the flexible joint connecting them. The M8 threaded holes pattern b9) allow the connection of the electrical motors. As explained above, the through holes c9) allows the connection

also to the vertical column, thus improving the stiffness of the system. The through holes d9) allow the connection with the ball screw assembly, using four M10 screws. The holes e9) are windows, needed to tighten the screws of the flexible joint connecting the ball screw and the motor.

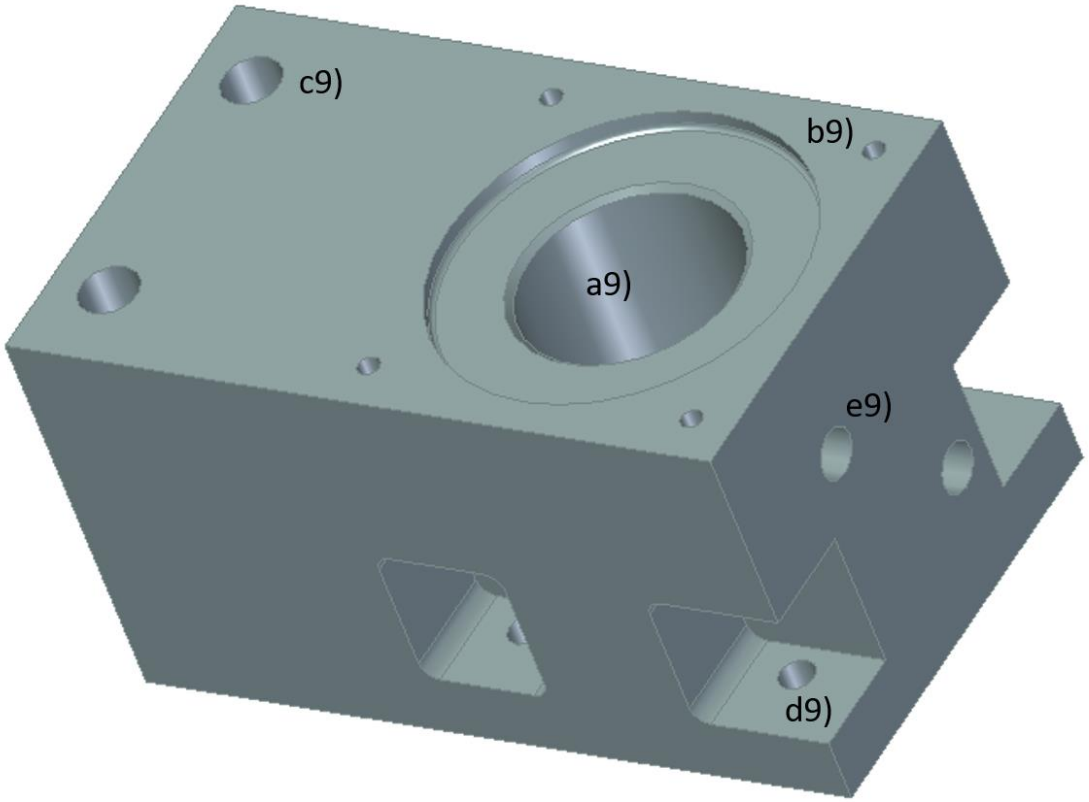

Figure 40: CAD drawing of the cube connecting the ball screw assembly and the electrical motors of the proposed shaker

Figure 41 shows the CAD drawing of the horizontal bars connecting the vertical columns of the proposed shaker. Two of these elements close each of the three sides of the delta robot. The threaded holes a10) correspond to the though holes b10) on the vertical columns, as Figure 39 shows. The three M8 threaded holes b10) connect the two horizontal bars of each side of the robot to a plate covering that side. The two M6 threaded holes c10) connect the upper horizontal bars to the horizontal plate cover. Although such holes are strictly needed only on the upper horizontal bars, both upper and lower bars have been produced according to this drawing, to reduce the number of parts and the complexity of the manufacturing.

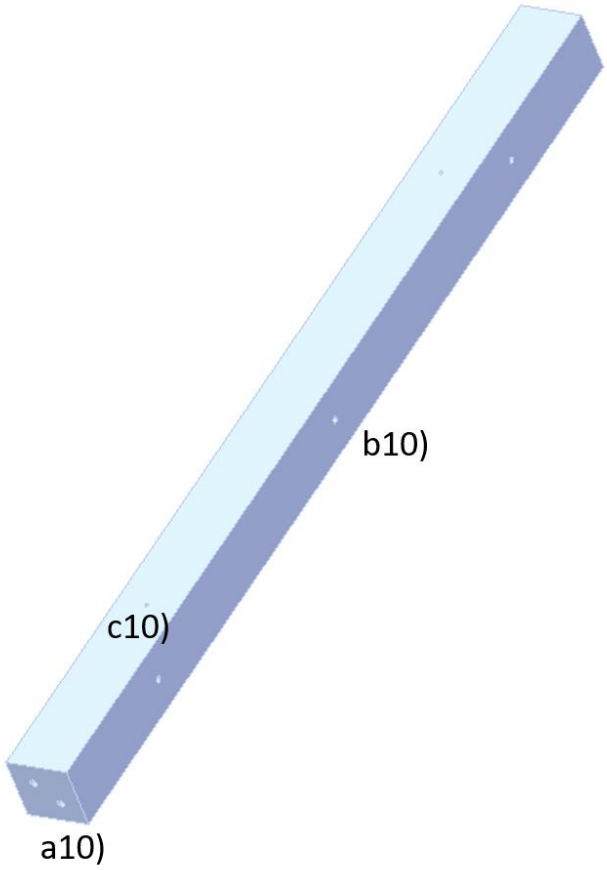

Figure 41: CAD drawing of the horizontal bars connecting the vertical columns of the proposed shaker

The FEM model was created using Abaqus FEA (Dassault Systèmes SE, 10 rue Marcel Dassault CS 40501 78946 Vélizy-Villacoublay Cedex – France). The first step for the creation of a FEM model was to simplify the geometry of the produced parts, by eliminating all the features with a defining dimension lower than 10 mm. This step is necessary to reduce the computational cost, as the description of small features through the FEM method would require many small elements and may not have a noticeable effect on the overall results. Five different materials have been defined: Aluminium, Steel, Bearing1, Bearing2 and Rubber. The properties associated to Aluminium, Steel, Bearing1 and Bearing2 are shown in Table 7, while the properties associated to Rubber, which was described through the Yeoh model, are shown in Table 8.

The material properties of the bearings have been computed to simulate their compliance, according to the data obtained from the manufacturer SKF. Under the expected loading conditions, the radial displacement of the angular contact roller bearing is equal to 6,5 μm. The expected radial displacement of the tapered roller bearing is equal to 2 μm. The bearings have been modelled as cylinders subjected to internal pressure. According to the theory of cylinder stress, equation 2.49 allows the computation of the equivalent Young Modulus for the bearings.

$$E = \frac{k}{u} \cdot \left((1-\nu)r + (1+\nu)\frac{R^2}{r} \right) \quad (2.49)$$

Where u is the expected radial displacement, r and R are respectively the inner and outer radii of the cylinder, ν is the Poisson's Ratio and the parameter k can be computed according to equation 2.50.

$$k = \frac{Pr^2}{R^2 - r^2} \quad (2.50)$$

The internal pressure, P, was estimated as the force acting along the radial direction of the bearing divided by the surface of the internal ring.

The equivalent density of the bearing was computed for each bearing as the mass divided by the nominal volume. Bearing1 material was assigned to the bearing model BEP 7200, while Bearing2 material was assigned to the bearing model 32912. The Steel material was assigned to the base plate and the rubber material was assigned to the rubber discs of the feet supporting the weight of the machine. The Aluminium material was assigned to all the other parts.

Table 7: properties associated to the materials Aluminium and Steel, as defined for the creation of the FEM model of the delta shaker.

Material Name	Young Modulus [MPa]	Density [kg/m^3]	Poisson's Ratio [-]
Aluminium	69000	2710	0,33
Steel	220000	7860	0,3
Bearing1	7780	5305	0,3
Bearing2	32950	7025	0,3

Table 8: properties associated to the rubber material, as defined for the creation of the FEM model of the delta shaker

C10	C20	C30	D1	D2	D3
0,9636	-0,6213	0,3265	0	0	0

The constraint imposed by the bearings was modelled using the coupling and tie interaction property. The coupling property was used to simulate the freedom of rotation allowed by the bearings. A reference point was created at the centre of each pin and at the centre of each hole. This ensure that the shaft inside the bearings can only rotate, but it cannot translate along its axis thus exiting from the bearings. Then the reference point on the pin was coupled with the outer surface of the pin, while the reference point in the hole was coupled with the inner surface of the hole. In both cases all the DOF

have been constrained. The purpose of the tie constraint is to fix all the bearings in their correct position. The outer surface of each bearing was tied to the inner surface of its hosting component. In fact, a tie constraint allows to link two surfaces in order to avoid the relative motion between them. The suspended parts have been then connected to the sliders through linear springs, applied to the four vertices of each slider, with a stiffness of 5500 N/mm. Moreover, only the rotation along the vertical axis of the sliders was allowed. This procedure was followed to model the compliance of the sliders. Finally, the model was connected to the ground by fixing all the degrees of freedom of the lower surface of the rubber discs. Figure 42 shows the FEM model of the linear delta shaker obtained after the process previously explained.

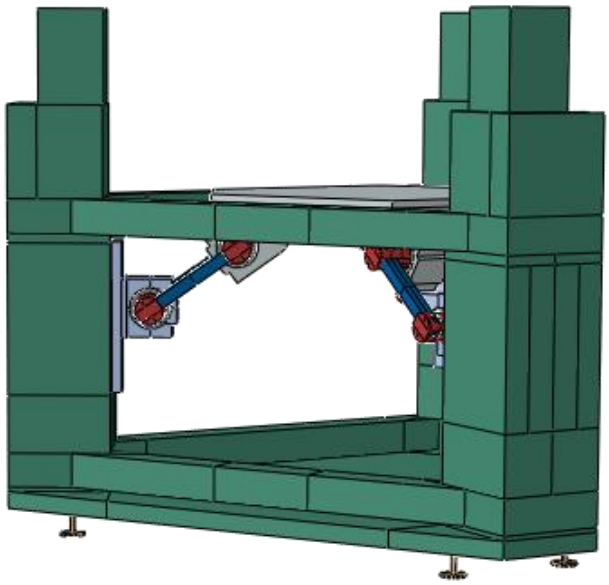

Figure 42: FEM structural model of the linear delta shaker

The elements type “Hex” were used to create the mesh for the modes of vibrations and the associated natural frequencies. To optimize the computational time, the size of the elements was different for each part of the shaker, according to its overall size and the size of its features. Elements with a size of 20 mm were used to model the whole structure. The links were modelled with elements of 4 mm size, the shaft of the cardan joint (item n.5 in Figure 31 - Figure 33) with elements of 3 mm size, and the plate connecting the cardan joints to the ball screws with elements of 7 mm size. Elements of size 6 mm were used to model all the remaining parts. The convergence of the results was ensured by varying the nominal size of the elements and verifying that the resulting modes of vibration and related natural frequencies did not change.

All the parts were then produced and mounted; the result is shown in Figure 43. In addition to the components previously shown, more elements were added to improve the safety of the machine. Vertical and horizontal covers are placed around the static structure, to prevent the accidental access to the empty volume under the moving platform. A two-steps ladder is placed in front of the shaker as a safety feature to help people to get on top of the moving platform. As an additional safety feature, also a frame of holding bars was added around the shaker.

Figure 43: Picture of the Linear Delta Shaker inside the MetroSpace Lab, at Lecco campus of Politecnico di Milano

Chapter III

3 Testing of the linear delta shaker

After the production of the machine, its performances were estimated both in terms of frequency response function, tested through the modal analysis, and in terms of characterization of the signal provided by the movement of the platform. Tests are needed to verify that the machine complies with the requirements and to understand the reasons behind the shortcomings.

3.1 Modal analysis

The modal analysis of the shaker is carried out through the creation of a model of the machine according to the Finite Elements Method (FEM) and its validation through the Experimental Modal Analysis (EMA), as explained in [77]. It is important to note that the correct validation of the FEM model is not crucial for the characterization of the performances of the robot, or its use as an excitation mean during future projects. However, an accurate model of the machine is of great interest to explain possible performance shortcomings and to simulate the outcome of corrective measures.

3.1.1 Method

The impulse was selected as the input signal for the EMA procedure. Such signal was provided through the dynamometric hammer 086C02 (PCB Piezotronics, Inc. 3425 Walden Avenue, Depew, NY 14043-2495 USA). Given the high mass of the structure to be excited and the interest in the response of the structure at low frequencies (i.e. < 100 Hz), the additional mass was screwed on the hammerhead, and the plastic tip was used. The output acceleration signal was measured through four single-axis piezoelectric accelerometers 4508B (PCB Piezotronics, Inc. 3425 Walden Avenue, Depew, NY 14043-2495 USA) and one three-axes piezoelectric accelerometer 356A22 (PCB Piezotronics, Inc. 3425 Walden Avenue, Depew, NY 14043-2495 USA). Two NI 9234 acquisition boards acquired all the signals. Both cards have been connected to a personal computer through the NI cDAQ9174 (National Instruments Corporation, 11500 N MoPac Expwy, Austin, Texas 78759-3504). The sampling frequency was set to 2048 Hz. One test was executed for each of the modal shape resulting from the FEM model with an associated natural frequency lower than 100 Hz. Each test consisted in 10 impulses, with a delay between impulses of at least 5 s. The position and the direction of the impulses and of the accelerometers was changed for each test, in accordance with the modal shape of interest. To improve the clarity of the dissertation, the position and direction of the

accelerometers and the impulse are given for each test together with the associated results in Figure 44 and Figure 45; in the following section 3.1.2. The signals acquired were used to compute the average H1 estimator of the frequency response function between the input force and each accelerometer. The modulus, phase and coherence of the estimators were analysed and compared to the results obtained by the FEM model for the validation process. The Modal Assurance Criterion (MAC) [78] was used to compare the modal shapes computed by the FEM model and the modal shapes extracted from the Experimental Modal Analysis, as in [79].

Moreover, also the frequency response function between the desired signal given as input to the machine and the actual acceleration measured at the centre of the platform was measured, for each of the three axes. White noise, with frequency components between 0,5 Hz and 50 Hz and RMS amplitude of 1 m/s^2 was used as the input signal. The signal was imposed for 120 s. The acceleration at the centre of the platform was measure through the tri-axial accelerometer 2466-010 made by Silicon Design Inc. (13905 NE 128th St. Kirkland, WA 98034 USA). The accelerometer was connected to the control system of the machine, which was custom-made by TRIO sistemi e misure s.r.l. (Viale Marconi 12e, 24044, Dalmine, BG, Italia). The signals were divided into 12 windows with no overlap, and the spectra were estimated by computing the H1 estimator, averaging the spectrum computed for each window.

3.1.2 Results

The results obtained from both FEM model and EMA shows that the vibration modes can be divided into two groups. The first group includes the modes of vibration involving the whole structure, while the second group includes the modes of vibration involving only the moving parts. To improve the consistency of the description of the results, the modes are shown as divided into these two groups, not in the order in which they appear frequency wise. This classification will be also relevant in the discussion section, where corrective measures to increase the natural frequencies of the robot are presented.

3.1.2.1 Modes of the structure

Regarding the modes involving the whole structure, the first resonance frequency is associated with the translation of the whole structure on the supports. It is computed to be at 20 Hz through the FEM. The EMA highlights the two resonances close to each other at 25 Hz and 30 Hz, as it is shown in Figure 44a. Given that all accelerometers move with the same response and in phase, it is possible to validate the FEM model with an error of 33% on the first resonance frequency. The MAC computed for this mode is equal to 0,94.

The second mode is the rotation of the whole structure on the supports and it occurs at 24 Hz according to the FEM model. In the results obtained from the experimental tests, it is possible to note that at 37.6 Hz accelerometers 1 has an almost null response while the other accelerometers move in phase, as it is shown in Figure 44b. In this case the error on the resonance frequency is 36%, and the MAC is equal to 0,91.

Figure 44c shows the third mode, which is the roto-translation of the whole structure on the supports. It is computed to occur at 83 Hz according to the FEM model. According to the EMA, it is possible to see that at 85 Hz it is possible to see that by increasing the height of accelerometer position, the modulus of the response increases, while the phases are equal. Accelerometer 1,2,3 are an example. This confirms the rotational motion, the frequency percentage error is 2,4% and the MAC is equal to 0,99.

As shown in Figure 44d, the fourth mode of vibration involving the whole structure is the bending of the structure. The results of the FEM model associate this mode with a frequency of 132 Hz. The EMA results show a resonance of the modulus of the H1 estimators of accelerometers 0, 2 and 3, which are placed on the columns, at the frequency of 129 Hz. The phases of H1 estimators are also equal for those accelerometers. The H1 function of accelerometer 1, which was placed at the centre of the platform do not show any resonance in the modulus, and its phase if opposite to the phase of the other accelerometers. This confirms the mode, with a percentage error on the frequency of 2,3% and a MAC equal to 0,86.

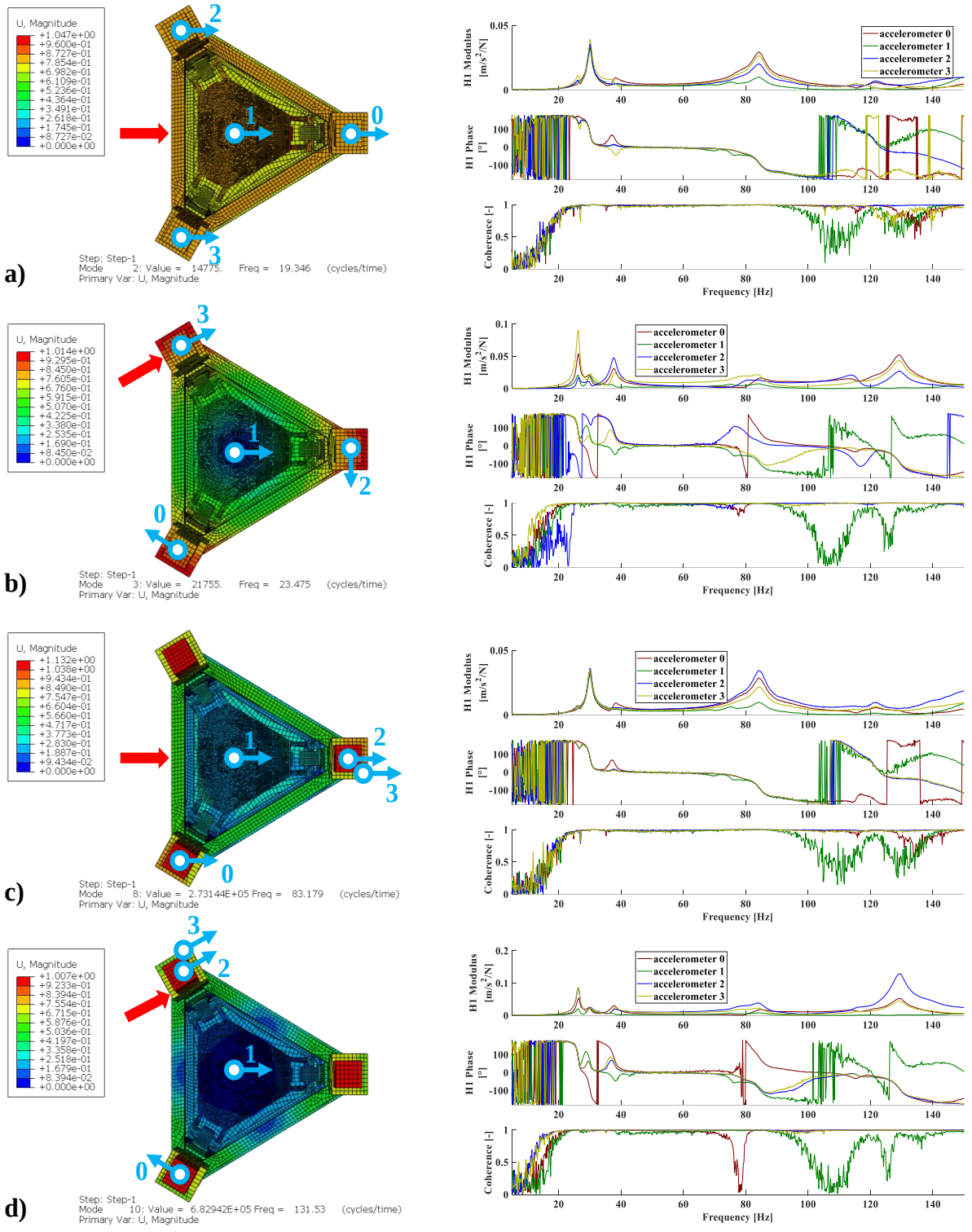

Figure 44: Comparison between the modes of vibration of the structure of the delta shaker computed by the FEM model and the frequency response functions estimated through the EMA

3.1.2.2 Modes of the platform

The first mode involving only the moving platform is its rotation of along the vertical axis and it occurs at 47 Hz according to the FEM model. As the results of the experiments (shown in Figure 45a) at 43 Hz accelerometer 2 remains still, while the others follow the rotation. Resonance peaks are confirmed by the phase shift of 180°. Accelerometers during the rotation move in phase. The mean percentage error is 9,3% and the MAC is 0,98.

The second mode is the Pitch of the moving platform around the horizontal axis and it is computed to occur at the frequency of 34 Hz. According to the experimental modal analysis, it is possible to see that a peak in modulus occurs at 65 Hz, as shown in Figure 45b. At that frequency the response of the accelerometer 2 is small. Accelerometer 0 and 3 move in phase, while accelerometer 1 is in counter phase, so it is possible to identify the mode. In this case, the mean percentage error on the frequency is 48 % and the MAC is equal to 0,99.

The third mode is the bending of the moving platform and it occurs at 107 Hz according to the results computed through the FEM model. According to the experimental data, as it is possible to see in Figure 45c, at the frequency of 107,5 Hz the response in modulus of accelerometer 2 is lower than the one of accelerometers 0, 1, 3 that respond in the same way and they move all in phase. In this case the mean percentage error is 2,7% and the MAC is equal to 0,89.

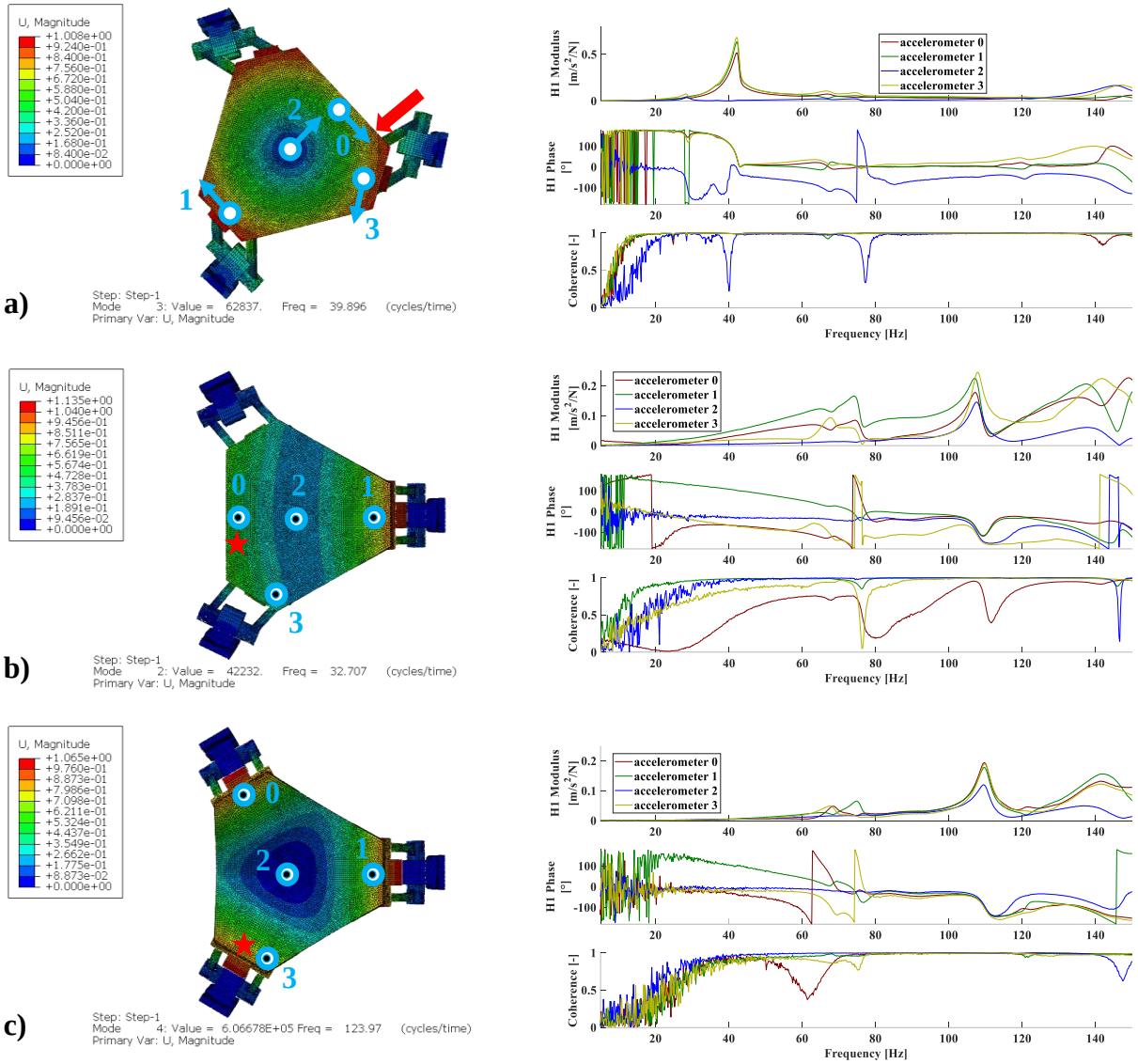

Figure 45: Comparison between the modes of vibration of the moving parts of the delta shaker computed by the FEM model and the frequency response functions estimated through the EMA

Figure 46 shows the H1 estimator of the Frequency Response Function computed by the control system of the delta robot between the provided input signal and the acceleration measured at the centre of the moving platform. The input signal was generated by the control itself and it was white noise; with an RMS value of 1 m/s^2 and a duration of 120 s. The frequency range was between 1 Hz and 50 Hz. The acquired signals were divided into 12 sections with a duration of 10 s each. The function is close to an ideal function up to 15 Hz. The horizontal axes show a modulus decrease below unity in the frequency range 27 Hz – 37 Hz, and a resonance at 47 Hz. The vertical axis shows a continuous increase in the modulus above 37 Hz. The phases of the three functions exhibit the same behaviour, except in the frequency range 22 Hz – 32 Hz and 45 Hz – 50 Hz, where the phase of the

FRF of the two horizontal axes show lower phase values in respect to the FRF of the vertical axis, which is almost linear throughout the whole frequency range taken into account. The coherence of all three functions drops for frequencies higher than 15 Hz, showing the effect of non-linarites in the actuation.

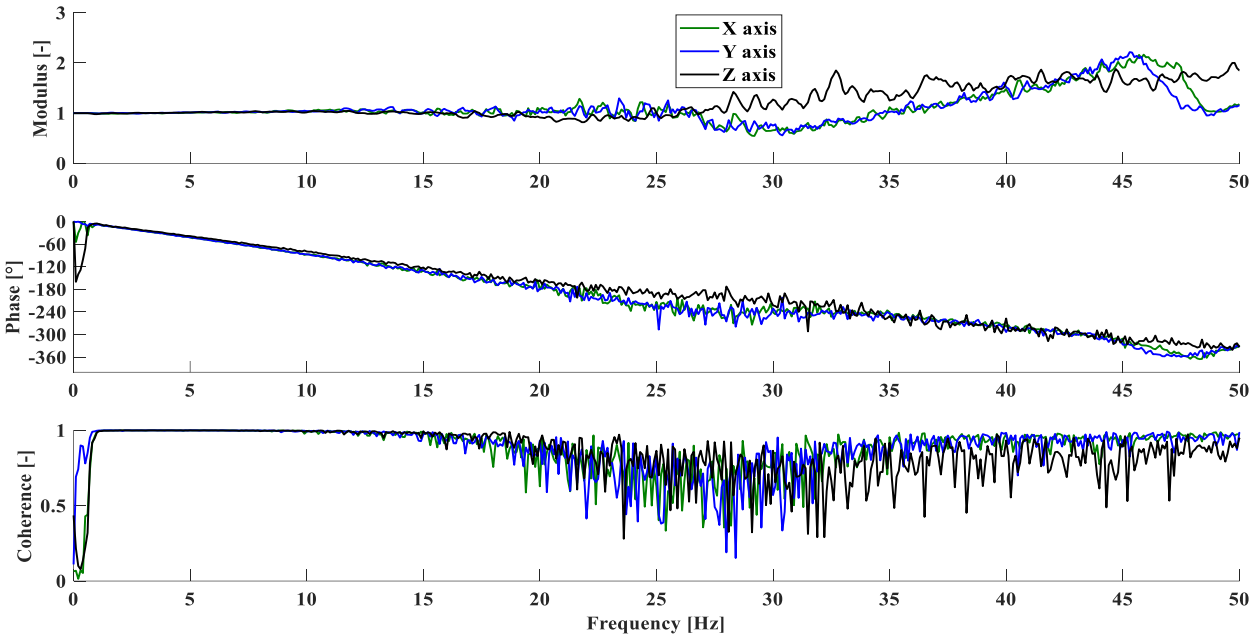

Figure 46: Moduli, Phases and Coherence of the frequency response functions between the input signal given to the delta shaker and the acceleration measured at the centre of the platform, along the three directions.

3.1.3 Discussion

Given the results obtained, it is possible to say that the EMA procedure validates the FEM model. The only critical situation is the pitch motion of the platform, in which the FEM model computes the natural frequency of the mode associated with an error higher than 40%, with respect to the experimental frequency response functions. However, this mismatch may be due to the high damping affecting this mode, which is shown by the slow pace with which the phases of the accelerometers 0 and 1 decrease of 180°. Taking this into account, the phases of such accelerometers shift of -90° at the frequency of 48 Hz, thus resulting in an estimation error of 29%.

The validated model allows to estimate the outcome of possible solution to increase the value of the natural frequencies of the machine. Regarding the modes affecting the whole robots, the solution found is to add structural elements to the base of the shaker, which are bolted into the ground, to increase the stiffness of the structure. Another possible solution could have been to decrease such natural frequency at frequencies below 1 Hz, however this would have led to high displacements due

to the low stiffness required. For safety reasons, this option was discarded. This intervention has already been executed, Figure 43 already shows the structural elements that were added to the base of the robot. Through this intervention, it was possible to increase the first natural frequency from 25 Hz to 34 Hz.

The interventions aimed at increasing the natural frequencies associated to the moving parts must be aimed both at increasing the stiffness and at decreasing the mass [80]. To decrease the mass, a new moving platform, made with lightweight material can be employed. With this new platform, also the connection wedges (elements 9 in Figure 31 and Figure 32) would not be necessary, thus leading to an increased bandwidth. To increase the stiffness of the moving parts, the most important intervention is the increase of the stiffness of the ball screws rails. Simulations with the FEM model show that by implementing the changes previously discussed, the first vibration mode related to the moving parts of the shaker, i.e. the pitch of the moving platform (Figure 45b), would be associated with a resonance frequency of 50 Hz. The validated FEM model also shows that other interventions aimed at decreasing the mass of other moving parts, like links and elements of the cardan joints, would lead to lower natural frequencies, due to the decrease of stiffness associated with the decrease of material quantity.

The frequency response functions between the imposed signal and the acceleration measured at the centre of the platform along the three axes is non-ideal inside the frequency range of interest. However, it does not show dramatic amplification in correspondence of the structural natural frequencies. Moreover, through the estimation of this function, it is possible to correct the input signal, thus leading to performances even exceeding the design requirements, as it is later shown in Figure 47.

3.2 Performance Evaluation

The performances of the shaker have been evaluated by imposing pseudo-random and sinusoidal stimuli. The pseudo-random stimulus tests aimed at evaluating whether the shaker could produce the design acceleration simultaneously along the three directions, suitable for evaluating the human response to vibrations. The harmonics tests were aimed at evaluating the quality of the signal generated, in terms of noise affecting the signal, uniformity across the surface of the platform and undesired rotation associated to the translation of the platform.

3.2.1 Pseudo random signals

3.2.1.1 Method

Two different tests were executed using the pseudo random signal. Fist, three different pseudo-random signals have been created as explained in 2.2, with frequency components between 1 Hz and 100 Hz, a duration of 120 s and an RMS value of 1 m/s^2. Acceleration signals were compensated for the frequency response function of the machine itself, as it is automatically done by the control software specifically made for the robot by TRIO sistemi e misure s.r.l. and then imposed to the three axes of movements of the end effector. The same test was repeated with a subject (height 172 cm, mass 62 kg, age 27) standing on the platform. The resulting acceleration have been measured at the centre of the platform using one three-axes accelerometer 2466-010 made by Silicon Design Inc. (13905 NE 128th St. Kirkland, WA 98034 USA), which was connected to the control system of the machine, with a sampling frequency of 1024 Hz. The acquired signal was divided in 120 segments with no overlap, and each segment was multiplied by the Hanning window; the modulus of the average spectrum between all the windows was computed. The moduli of the signals acquired with and without load have been compared to the modulus of the reference signal, using a ±3 dB tolerance, along the three axes. The Mean Quadratic Error between the measured moduli and the reference signal was used to characterize the error inside the frequency of interest (i.e. 1-100 Hz), while the Root Mean Squared value of the components at higher frequencies was used to characterize the noise which affected the signal.

A second test involving the pseudo-random signal was used to evaluate the crosstalk between the axes. The pseudo-random signals and the acquisition system for this test were the same as in the previous one, however they have been imposed only one axis each time. The signals were then amplified with a factor of 2 (RMS value of the reference signal of 2 m/s^2) and with a factor of 3 (RMS value of the reference signal of 3 m/s^2). The crosstalk between the axes was evaluated by comparing the RMS value of the acceleration along all the axes. No person was involved in this test.

3.2.1.2 Results

Figure 47 compares the moduli of the spectra of the acceleration signal acquired at the centre of the moving platform, with and without a person standing on it, with the modulus of the spectrum of the reference signal. Plots show that there are no significant differences between the loaded case and unloaded case. The moduli of the acquired spectra are comprised inside the ±3 dB tolerance band computed in respect of the reference accelerometers, except at frequencies higher than 90 Hz, for the Y-axis and the Z-axis.

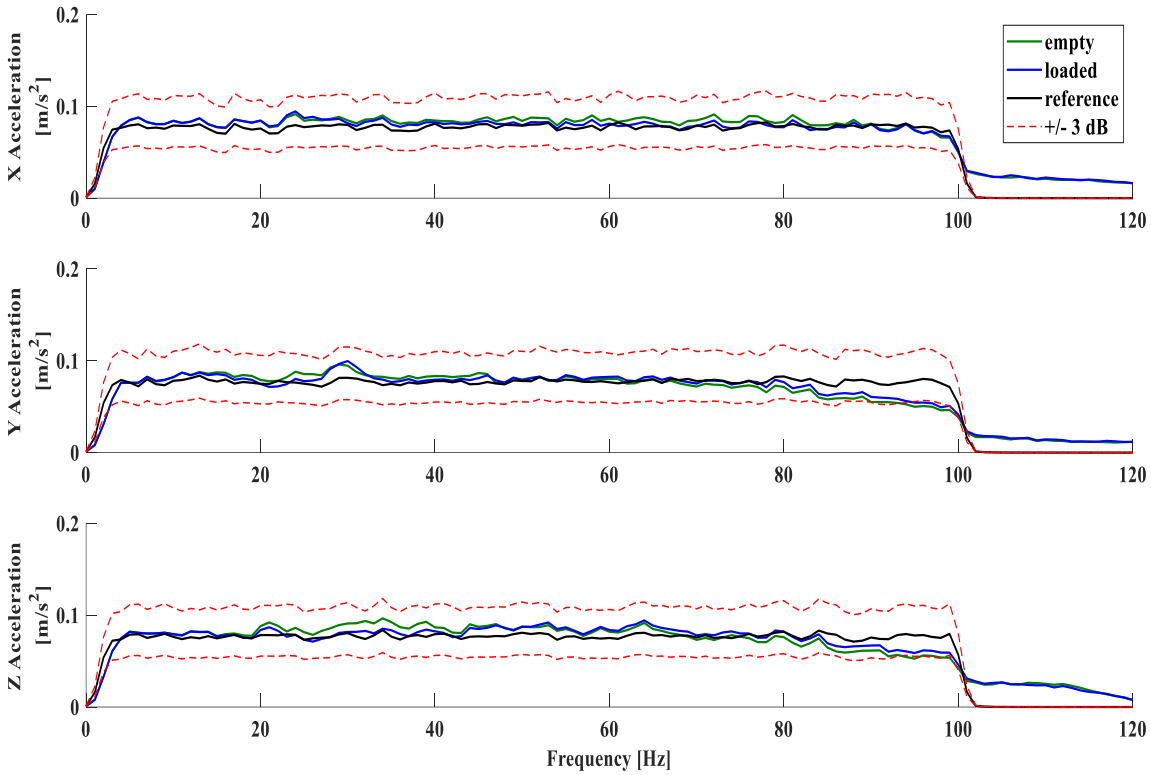

Figure 47: Comparison between the imposed acceleration signal and the acceleration of the moving platform, free and loaded with a person standing on it, along the three directions

Table 9 reports the mean quadratic error of the moduli of the spectra of the acceleration signals acquired when a pseudo-random signal was imposed simultaneously along the three axes, with and without a person standing on the platform. The lowest value is 5,3 mm/s^2 and it is measured along the X-axis when the platform was loaded. The highest value is 11,4 mm/s^2 and it is measured along the Y-axis when the platform was not loaded. The loaded case shows a better accordance between the measured signal and the reference signal inside the frequency range of interest, with a mean quadratic error across the axis of 13,4 mm/s^2, compared to 17,2 mm/s^2 for the unloaded case.

Table 9: Mean quadratic errors of the moduli of the spectra of the acceleration signals measured on the moving platform at frequencies between 1 and 100 Hz, when imposing pseudo-random noise with RMS of 1 m/s2 and equal frequency components between 1 and 100 Hz contemporarily along the three spatial axes

	X [mm/s^2]	Y [mm/s^2]	Z [mm/s^2]
No load	7,0	11,4	10,8
Loaded	5,3	9,3	8,1

Table 10 shows the RMS value of the acceleration outside the nominal excitation bandwidth (higher than 100 Hz). The highest value is measured along the X-axis in the loaded case and is 9,9 mm/s^2. The lowest value is 7,3 mm/s^2, and it is measured along the y-axis in the unloaded case. However, no meaningful difference can be found in the noise outside the frequency band of interest between the unloaded and loaded scenarios.

Table 10: Mechanical noise outside the excitation band: RMS of the vibration at frequencies higher than 100 Hz, when imposing pseudo-random noise with RMS of 1 m/s^2 and equal frequency components between 1 and 100 Hz contemporarily along the three spatial axes

	X [mm/s^2]	Y [mm/s^2]	Z [mm/s^2]
No load	9,8	7,3	8,3
Loaded	9,9	7,5	8,1

Table 11 shows the RMS value of acquired signals and compares them to the reference value. In all the cases, the acceleration amplitude is higher than the reference one. The lowest increase can be found along the Y-axis in the unloaded case, with an increase of 1% in respect to the nominal value, while the highest increase can be found along the X-axis in the loaded case, with an increase of 9% in respect to the nominal value.

Table 11: Root-Mean-Squared values of the signal acquired with no load, with load and of the reference signal when imposing pseudo-random noise with RMS of 1 m/s^2 and equal frequency components between 1 and 100 Hz contemporarily along the three spatial axes

RMS [m/s^2]	X	Y	Z
No load	1,094	1,010	1,049
Loaded	1,063	1,016	1,046
Reference	1,000	1,000	1,000

Table 12 to Table 14 show the RMS of the acceleration signal measured along the three axes at the centre of the platform when three pseudo-random acceleration signals with RMS of 1 m/s^2, 2 m/s^2 and 3 m/s^2 and frequency components between 1 and 50 Hz were imposed only along the X-axis. The RMS value of the acceleration measured along the Y-axis is on average 12% of the reference signal, while the RMS value of the acceleration measured along the Z-axis is on average 36% of the reference signal. No meaningful differences can be found in respect to the amplitude of the reference signal.

Table 12: Comparison between the Root-Mean-Squared values of the signal acquired with no load and of the reference signal, when imposing pseudo-random noise with RMS of 1 m/s^2 and equal frequency components between 1 Hz and 50 Hz along the X direction

RMS [m/s^2]	X	Y	Z
Measured Signal	0,93	0,12	0,37
Reference	1,00	0,00	0,00

Table 13: Comparison between the Root-Mean-Squared values of the signal acquired with no load and of the reference signal, when imposing pseudo-random noise with RMS of 2 m/s^2 and equal frequency components between 1 Hz and 50 Hz along the X direction

RMS [m/s^2]	X	Y	Z
Measured Signal	1,96	0,23	0,70
Reference	2,00	0,00	0,00

Table 14: Comparison between the Root-Mean-Squared values of the signal acquired with no load and of the reference signal, when imposing pseudo-random noise with RMS of 3 m/s^2 and equal frequency components between 1 Hz and 50 Hz along the X direction

RMS [m/s^2]	X	Y	Z
Measured Signal	3,05	0,39	1,05
Reference	3,00	0,00	0,00

Table 15 to Table 17 show the RMS of the acceleration signal measured along the three axes at the centre of the platform when three pseudo-random acceleration signals with RMS of 1 m/s^2, 2 m/s^2 and 3 m/s^2 and frequency components between 1 and 50 Hz were imposed only along the Y-axis. The RMS value of the acceleration measured along the X-axis is on average 19% of the reference signal, while the RMS value of the acceleration measured along the Z-axis is on average 22% of the reference signal. As for the previous tests, no meaningful differences can be found in respect to the amplitude of the reference signal.

Table 15: Comparison between the Root-Mean-Squared values of the signal acquired with no load and of the reference signal, when imposing pseudo-random noise with RMS of 1 m/s^2 and equal frequency components between 1 Hz and 50 Hz along the Y direction

RMS [m/s^2]	X	Y	Z
Measured Signal	0,19	0,94	0,24
Reference	0,00	1,00	0,00

Table 16: Comparison between the Root-Mean-Squared values of the signal acquired with no load and of the reference signal, when imposing pseudo-random noise with RMS of 2 m/s^2 and equal frequency components between 1 Hz and 50 Hz along the Y direction

RMS [m/s^2]	X	Y	Z
Measured Signal	0,37	1,97	0,41
Reference	0,00	2,00	0,00

Table 17: Comparison between the Root-Mean-Squared values of the signal acquired with no load and of the reference signal, when imposing pseudo-random noise with RMS of 3 m/s^2 and equal frequency components between 1 Hz and 50 Hz along the Y direction

RMS [m/s^2]	X	Y	Z
Measured Signal	0,54	3,06	0,66
Reference	0,00	3,00	0,00

Table 18 to Table 20 show the RMS of the acceleration signal measured along the three axes at the centre of the platform when three pseudo-random acceleration signals with RMS of 1 m/s^2, 2 m/s^2 and 3 m/s^2 and frequency components between 1 and 50 Hz were imposed only along the Z-axis. The RMS value of the acceleration measured along the X-axis does not seem to be linked with the amplitude of the acceleration of the reference signal. Its value increases from 0,09 m/s^2 to 0,11 m/s^2, the augmentation is not proportional to the RMS value of the reference signal. The RMS value of the acceleration measured along the Y-axis is on average 8% of the reference signal.

Table 18: Comparison between the Root-Mean-Squared values of the signal acquired with no load and of the reference signal, when imposing pseudo-random noise with RMS of 1 m/s^2 and equal frequency components between 1 Hz and 50 Hz along the Z direction

RMS [m/s^2]	X	Y	Z
Measured Signal	0,09	0,08	0,98
Reference	0,00	0,00	1,00

Table 19: Comparison between the Root-Mean-Squared values of the signal acquired with no load and of the reference signal, when imposing pseudo-random noise with RMS of 2 m/s^2 and equal frequency components between 1 Hz and 50 Hz along the Z direction

RMS [m/s^2]	X	Y	Z
Measured Signal	0,10	0,18	1,96
Reference	0,00	0,00	2,00

Table 20: Comparison between the Root-Mean-Squared values of the signal acquired with no load and of the reference signal, when imposing pseudo-random noise with RMS of 3 m/s^2 and equal frequency components between 1 Hz and 50 Hz along the Z direction

RMS [m/s^2]	X	Y	Z
Measured Signal	0,11	0,23	2,96
Reference	0,00	0,00	3,00

3.2.2 Sinusoidal Signals

3.2.2.1 Method

Two series of tests were performed using sinusoidal acceleration. The first consisted in imposing a sinusoidal acceleration signal with a RMS value of 1 m/s^2 and frequency of 5 Hz, 10 Hz, 15 Hz and 20 Hz along a single axis each time, for a duration of 10 s. The acceleration was measured by five single-axis piezo-accelerometers 4508B (PCB Piezotronics, Inc. 3425 Walden Avenue, Depew, NY 14043-2495 USA), which were connected to two NI 9234 acquisition boards. Both cards have been connected to the NI cDAQ9174 (National Instruments Corporation, 11500 N MoPac Expwy, Austin, Texas 78759-3504), which were connected to a personal computer. The position and the sensing direction of the accelerometers was different for each direction tested, and it is reported in Figure 48.

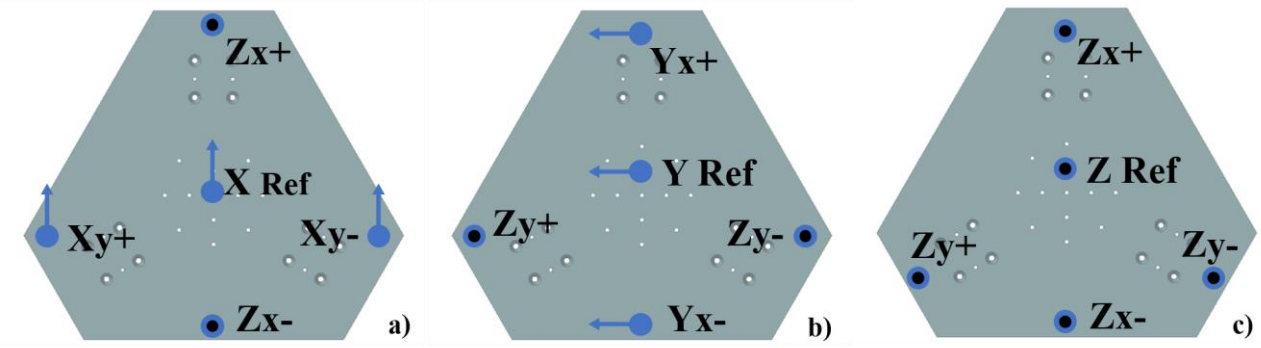

Figure 48: Position of the accelerometers on the moving platform and their sensing direction for the tests done along: a) the X direction, b) the Y direction and c) the Z direction

The spectrum of the signals acquired by the reference accelerometers have been used to quantify the noise affecting the signal. The spectrum has been normalized with respect to the modulus at the reference frequency. To evaluate the motion of the platform, the RMS of the signals acquired by the accelerometers sensing along the direction of excitation were compared. For the two tests done in the horizontal plane, the spectra of the signals acquired by the accelerometers sensing in the vertical direction have been computed. The absolute value of phase difference of the harmonics with a

modulus higher than 0,01 m/s^2 have been used to characterize undesired rotations. Along the vertical direction, the same procedure was adopted, but the phase difference was computed between each accelerometer and the reference one.

The second test done using a sinusoidal excitation consisted in applying such signal to all three degrees of freedom, one at each time, with a fixed frequency from 1 Hz to 30 Hz, with the step of 1 Hz. Two different nominal amplitudes have been imposed, 1 m/s^2 and 5 m/s^2. At low frequencies, due to the limits on the displacement, the amplitude was decreased. At 1 Hz, the acceleration imposed had an amplitude of 0,5 m/s^2. At 2 Hz the maximum acceleration imposed was 1 m/s^2. At 3 Hz the maximum acceleration imposed had an amplitude of 1,5 m/s^2. Between 4 and 6 Hz the amplitude of the acceleration imposed had a maximum value of 2 m/s^2. The acceleration signals were measured at the centre of the moving platform, along the imposed direction of motion, and on the three actuators, along the vertical direction. The measurement setup was the same used in the previous test: four single-axis piezo-accelerometers 4508B (PCB Piezotronics, Inc. 3425 Walden Avenue, Depew, NY 14043-2495 USA) were connected to one NI 9234 acquisition boards. Moduli were docked in a NI cDAQ9174 (National Instruments Corporation, 11500 N MoPac Expwy, Austin, Texas 78759-3504) chassis and then connected to a personal computer. Tests were performed after that the platform reached the steady state; signals have been acquired for 4 s. The time histories were then segmented into four sections of 1 s. The spectra of all the signals have been then estimated as the complex average of the spectra of the four segments; the complex averaging procedure was possible thanks to the ratio between the signal period and the length of the observation window. The moduli of the nominal excitation frequency, the 2X, 3X and 4X harmonics have then been extracted. The modulus of the signal acquired at the centre of the platform evaluated at the nominal excitation frequency was used to normalize all the other spectra evaluated in the same testing conditions.

3.2.2.2 Results

Figure 49 shows an example of the acceleration signal measured at the centre of the moving platform when imposing a sinusoidal signal along the X direction, with an amplitude of 1 m/s^2 and a frequency of 15 Hz.

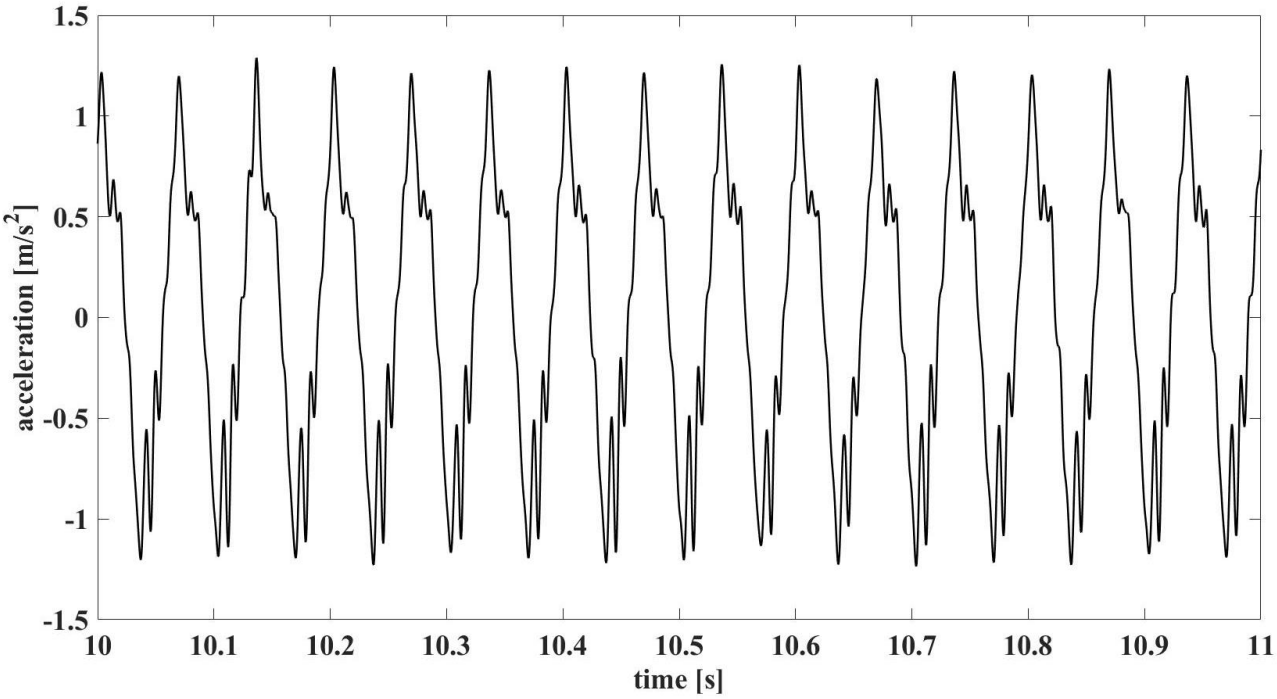

Figure 49: Example of time history of the acceleration signal measured at the centre of the moving platform when imposing a sinusoidal signal along the X direction, with an amplitude of 1 m/s^2 and a frequency of 15 Hz

Figure 50 to Figure 52 show the relative acceleration spectra (ratio between the amplitude at each frequency divided by the amplitude of the principal harmonic). The stimuli were sinusoidal signals with frequencies of 5 Hz, 10 Hz, 15 Hz and 20 Hz along the X-axis, Y-axis and Z-axis. Plots show that at each excitation frequency, independently from the direction of motion, the spectra are characterized by multiple harmonics, in particular by the 3X multiple. Multiple harmonics are further amplified by the natural resonances of the system: the 5X harmonics of the 5 Hz sinusoidal signal for example is amplified along the X and Y direction. Along the Z direction, all the multiples at 30 Hz are amplified.

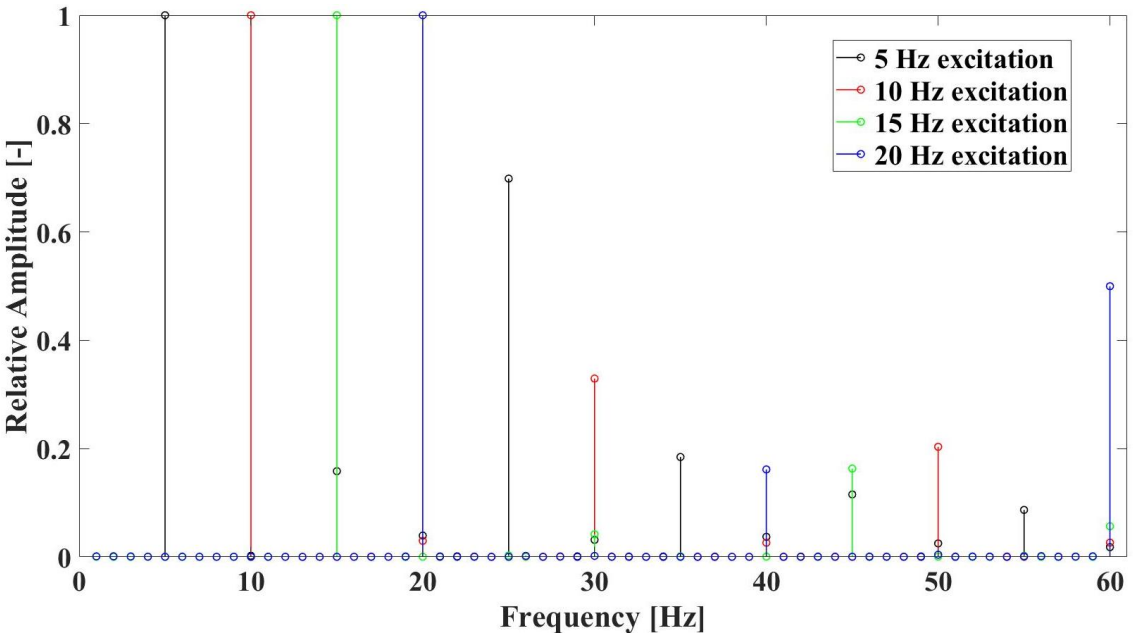

Figure 50: Moduli of the spectra of the signals acquired by the reference accelerometers normalized by the value at the reference signal, when a sinusoidal acceleration with a frequency of 5 Hz, 10 Hz, 15 Hz and 20 Hz is imposed along the X direction

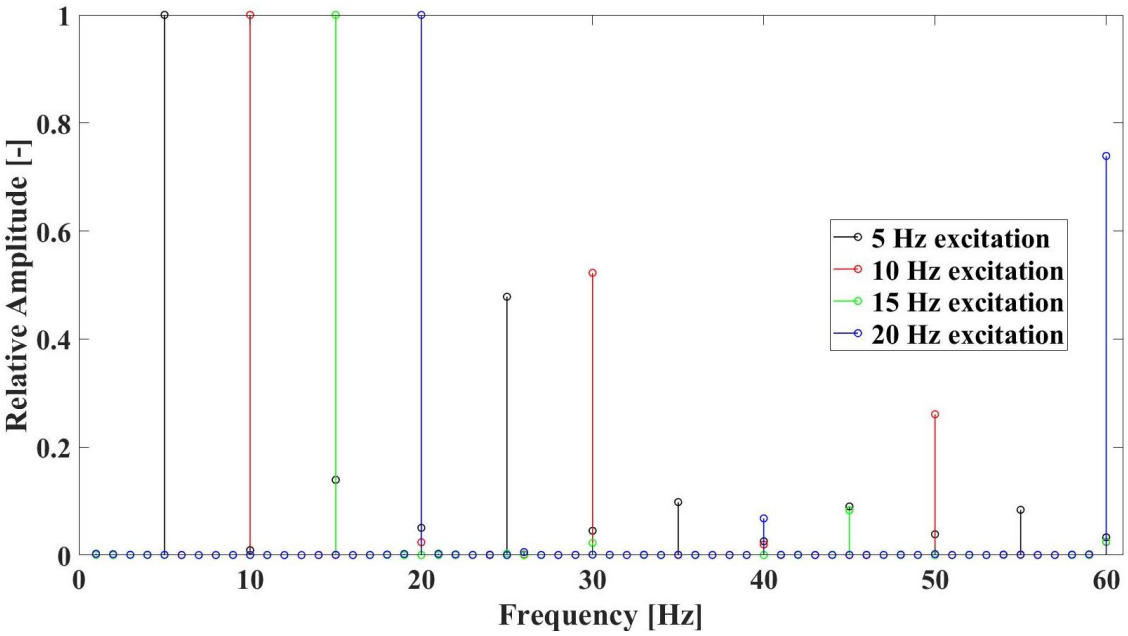

Figure 51: Moduli of the spectra of the signals acquired by the reference accelerometers normalized by the value at the reference signal, when a sinusoidal acceleration with a frequency of 5 Hz, 10 Hz, 15 Hz and 20 Hz is imposed along the Y direction

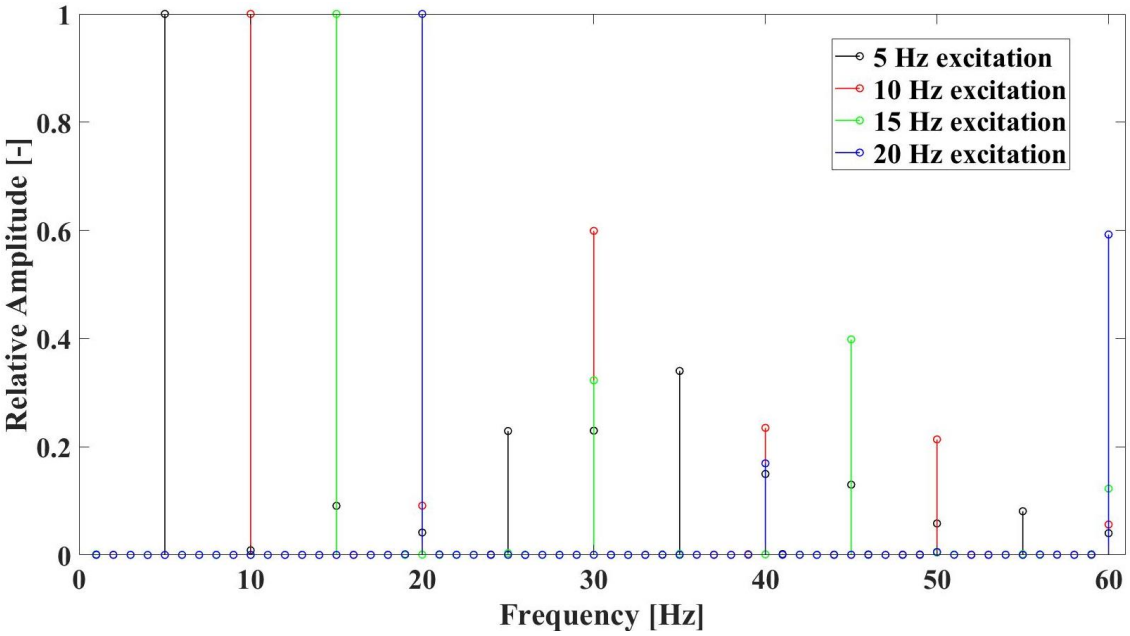

Figure 52: Moduli of the spectra of the signals acquired by the reference accelerometers normalized by the value at the reference signal, when a sinusoidal acceleration with a frequency of 5 Hz, 10 Hz, 15 Hz and 20 Hz is imposed along the Z direction

Table 21 to Table 23 show the difference between the RMS value of the acceleration measured by the accelerometers pointing in the direction of the motion and the reference accelerometer, expressed as a percentage of the RMS of the acceleration measured by the reference accelerometer. Along the X direction, the accelerometer X_{y+} measured an acceleration with an RMS value 17% higher than the one measured by the reference accelerometer, when a 20 Hz sinusoidal signal was imposed. The accelerometer X_{y-} measured an acceleration with an RMS value 15% higher and 14% higher than the one measured by the reference accelerometer, when a 5 Hz and 10 Hz sinusoidal signal were imposed, respectively. When the test was repeated along the Y direction, the accelerometers Y_{x+} and Y_{x-} measured an acceleration with an RMS value which differed less than 10% from the RMS value of the acceleration measured by the reference accelerometer. Regarding the tests done along the Z direction, the accelerometers Z_{y+} and Z_{y-} measured an acceleration with an RMS value which differed from the one measured by the reference accelerometer when the excitation frequency was 20 Hz of 15% and 23% respectively. When the excitation frequency was 15 Hz, Z_{y-} measured an acceleration whose RMS value differed from the value measured by the reference accelerometer of 15%. Z_{x+} and Z_{x-} never measured an acceleration signal whose RMS value was different from the one measured by the reference accelerometer more, or less than, 10%.

Table 21: Percentage difference between the RMS value of the signals acquired by the accelerometers pointing in the X direction and the reference accelerometer, computed in respect of the reference accelerometer, for the tests done along the X direction

Excitation Frequency [Hz]	X_{y+} [%]	X_{y-} [%]
5	9	15
10	9	14
15	5	-1
20	17	-2

Table 22: Percentage difference between the RMS value of the signals acquired by the accelerometers pointing in the Y direction and the reference accelerometer, computed in respect of the reference accelerometer, for the tests done along the Y direction

Excitation Frequency [Hz]	Y_{x+} [%]	Y_{x-} [%]
5	5	-3
10	6	-4
15	4	-2
20	3	5

Table 23: Percentage difference between the RMS value of the signals acquired by the accelerometers pointing in the Z direction and the reference accelerometer, computed in respect of the reference accelerometer, for the tests done along the Z direction

Excitation Frequency [Hz]	Z_{y+} [%]	Z_{y-} [%]	Z_{x+} [%]	Z_{x-} [%]
5	2	-3	-9	10
10	-1	3	-10	6
15	3	15	-8	9
20	15	23	9	5

Figure 53 and Figure 54 show the absolute value of the difference between the phases of the spectra of the acceleration signal measured by the accelerometers measuring along the vertical direction, when the sinusoidal signal was imposed along the X-axis and Y-axis respectively. Results are consistent across both direction of motion and excitation frequencies. In fact, the phase difference of the first harmonic exceed 150° in all the cases, except when a sinusoidal signal with a frequency of 20 Hz was imposed along the X-axis. The average phase difference between the first harmonics,

across both directions and all the excitation frequencies is 150°, with a standard deviation of 46°. Figure 55 shows the absolute value of the difference between the phases of the spectra of the signals acquired by the accelerometers placed on opposite side of the moving platform when the sinusoidal motion was imposed along the Z-axis. The plots show low values of phase difference, as the maximum value of phase difference of a fundamental harmonic is reached by the accelerometers Z_{X+} and Z_{X-} when the excitation frequency was 20 Hz, and it is 15°

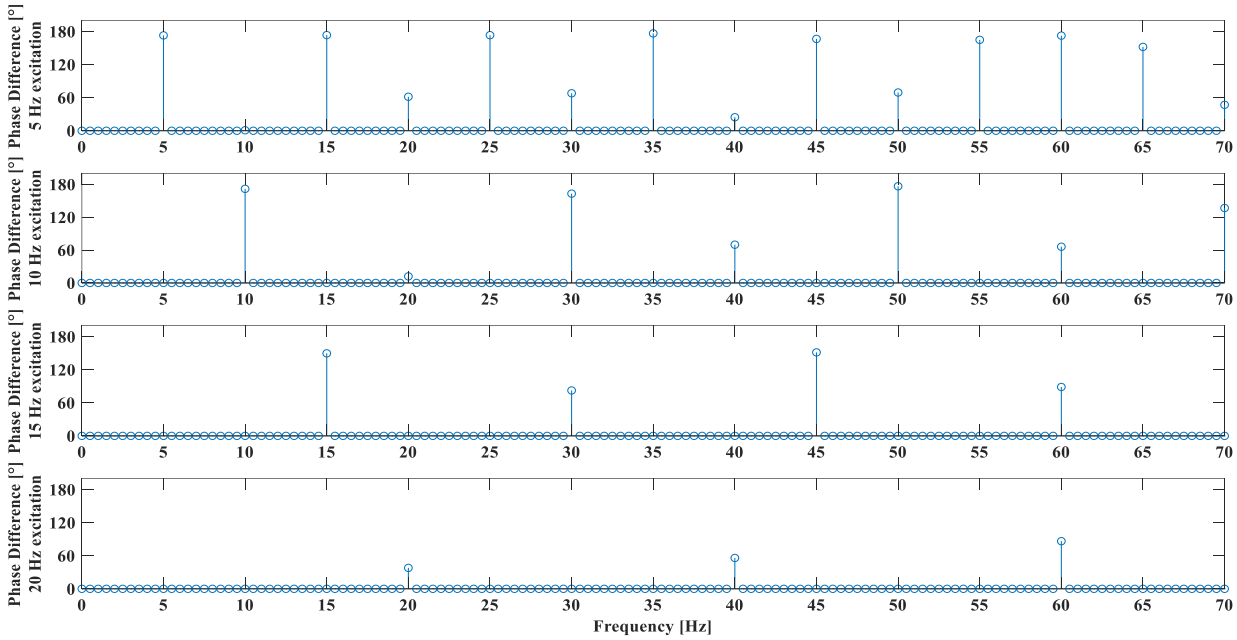

Figure 53: Absolute value of the spectra phase difference between the accelerometers pointing in the vertical direction during the tests done imposing a sinusoidal acceleration along the X direction

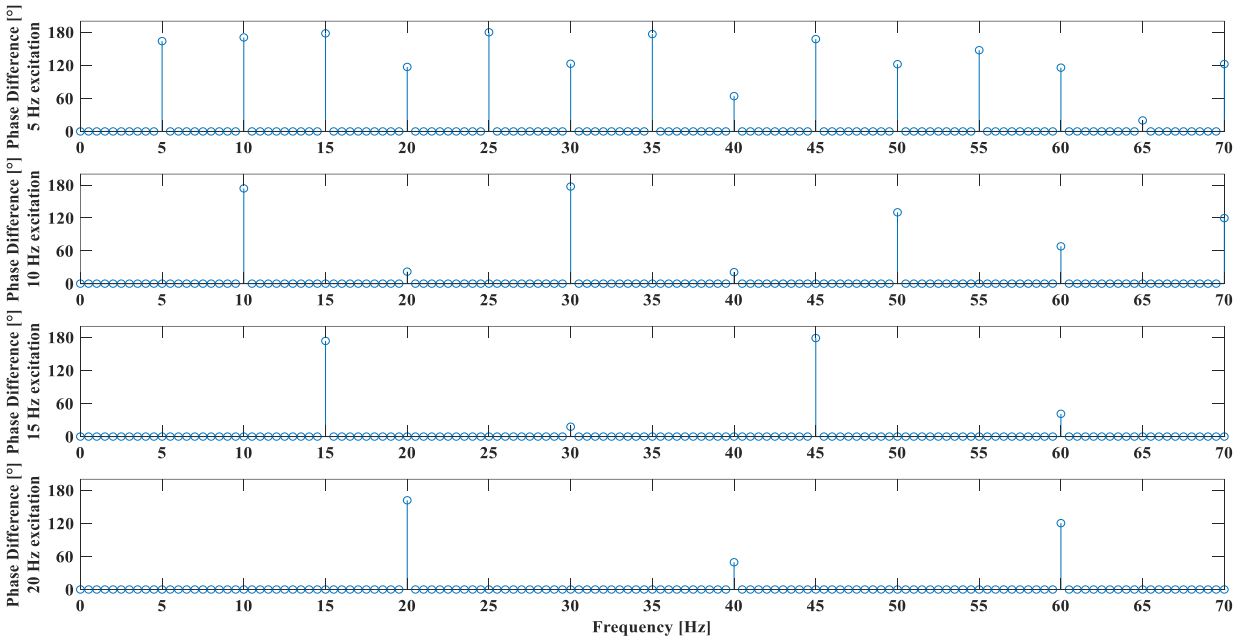

Figure 54: Absolute value of the spectra phase difference between the accelerometers pointing in the vertical direction during the tests done imposing a sinusoidal acceleration along the Y direction

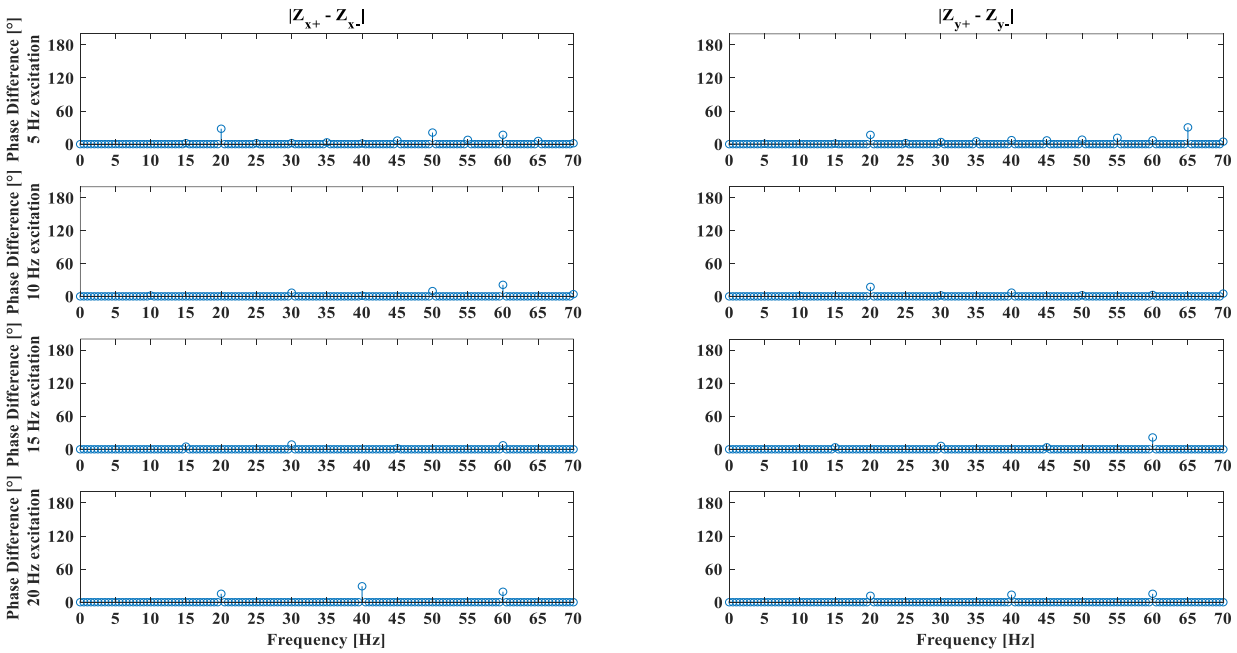

Figure 55: Absolute value of the spectra phase difference between the accelerometers pointing in the vertical direction aligned along the X axis (left) and aligned along the Y axis (right) during the tests done imposing a sinusoidal acceleration along the Z direction

Figure 56 shows the results obtained from the sinusoidal tests done by imposing the excitation along the X direction, with an amplitude of 1 m/s^2. As it is possible to see from the top plot, the 3X harmonic is the most relevant one, with a maximum of 0,76 at the frequency of 27 Hz. The signals acquired at the actuators show that after the frequency of 20 Hz the acceleration at the first actuator increase from an average of 1,2 to values always higher than 2, while signals on the other two actuators decrease from averages of 0,66 (actuator 2) and 0,65 (actuator 2) to values lower than 0,3.

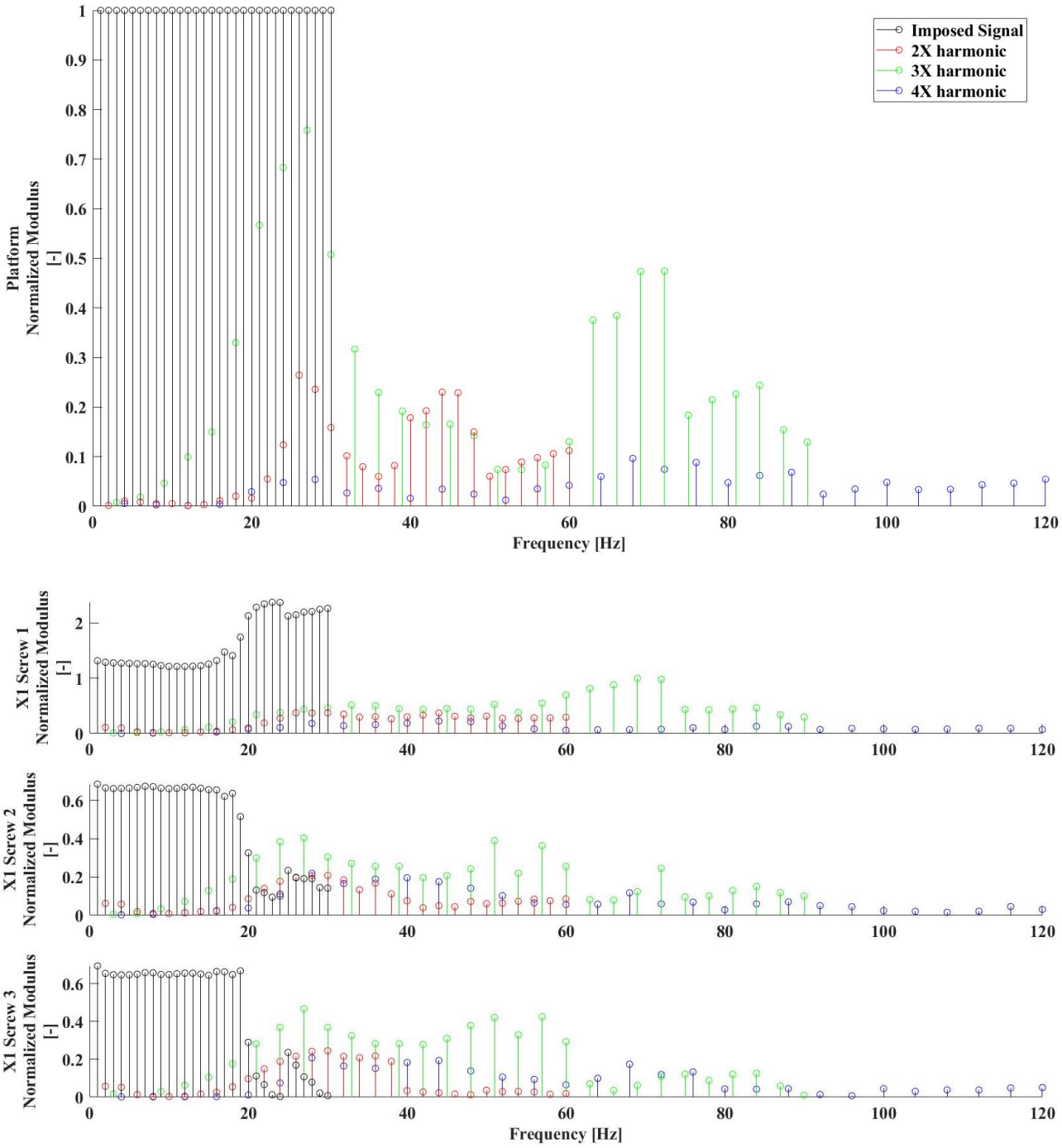

Figure 56: Plot of the nominal frequencies and multiple harmonics of the signals acquired on the moving platform and on the three actuators during the tests done by imposing a sinusoidal acceleration with an amplitude equal to 1 m/s^2 along the X direction normalized by the fundamental frequency of the signal acquired at the centre of the moving platform

Figure 57 shows the results obtained from the sinusoidal tests done by imposing the excitation along the X direction, with an amplitude of 5 m/s^2. The top plot shows again that the 3X harmonic is the most relevant one. In this case, the maximum is equal to 0,46 and it is measured at the frequency of 24 Hz. The moduli of the fundamental frequency of the acceleration signals measured along the

first actuator show first a slight decrease to a minimum of 0,69 Hz at the frequency of 23 Hz. The acceleration signals acquired along the other two axes show a more marked decrease in the modulus after the frequency of 20 Hz, reaching values as low as 0,09 (actuator 2) at the frequency of 27 Hz. Moreover, all the moduli of the fundamental frequencies acquired on the actuators show a sharp increase the frequency of 29 Hz, up to a value of 4,5 (actuator 1).

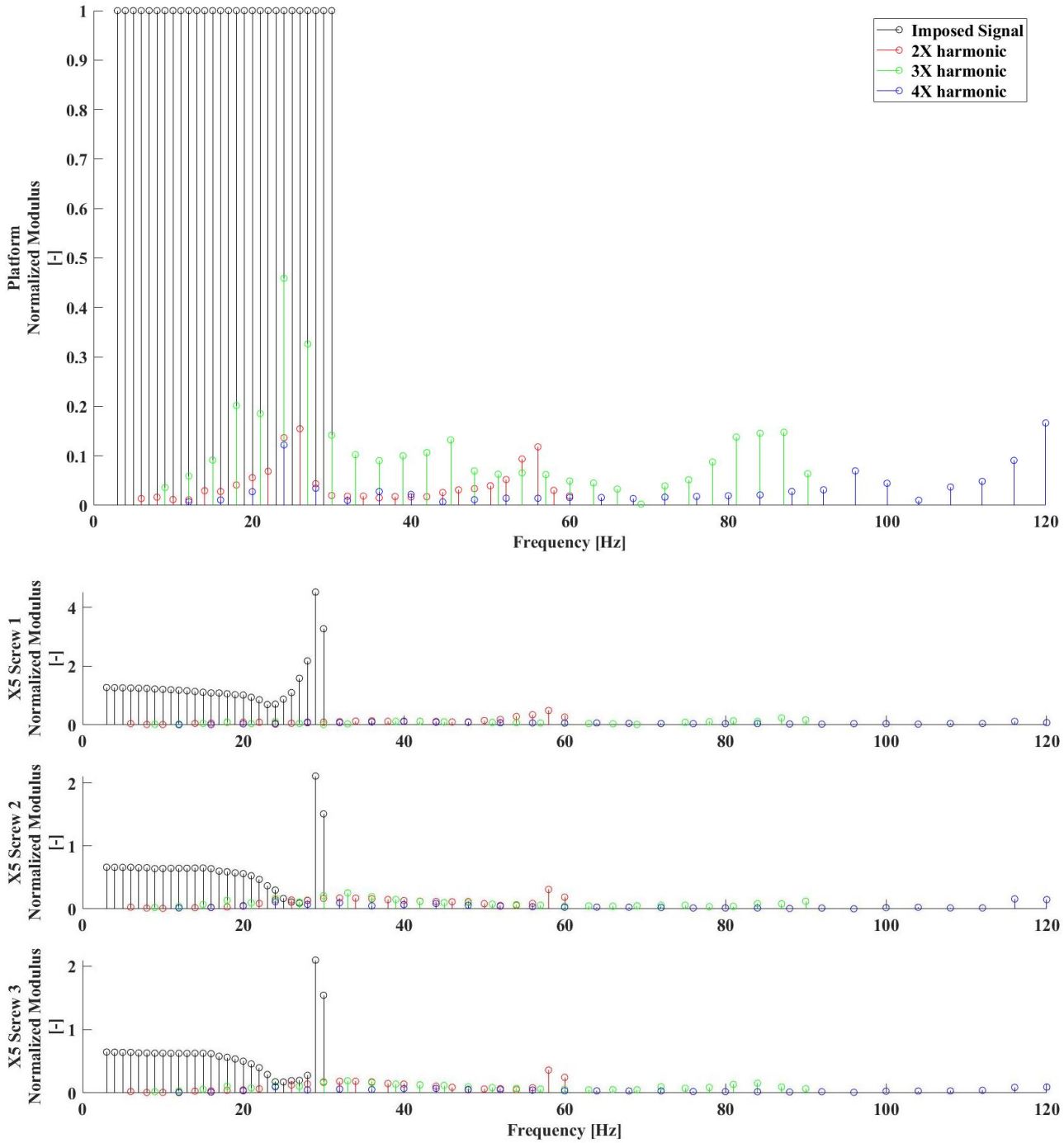

Figure 57: Plot of the nominal frequencies and multiple harmonics of the signals acquired on the moving platform and on the three actuators during the tests done by imposing a sinusoidal acceleration with an

amplitude equal to 5 m/s^2 along the X direction, normalized by the fundamental frequency of the signal acquired at the centre of the moving platform

Figure 58 shows the results obtained from the sinusoidal tests done by imposing the excitation along the Y direction, with an amplitude of 1 m/s^2. Also in this direction, the 3X component is the most relevant multiple frequency measured at the centre of the platform, reaching a value of 0,72 at the frequency of 27 Hz. The bottom plots show that all the fundamental frequencies exhibit an increase after the frequency of 15 Hz. For actuators 2 and 3, they increase from an average of 1,1 to an average of 1,4. Moreover, after the frequency of 27 Hz, the fundamental frequencies of the signal acquired at actuator 2 show a decrease, down to a minimum of 1,2 at the frequency of 30 Hz; while on the actuator 3 it shows a parallel increase, up to a maximum of 1,5, at the frequency of 30 Hz.

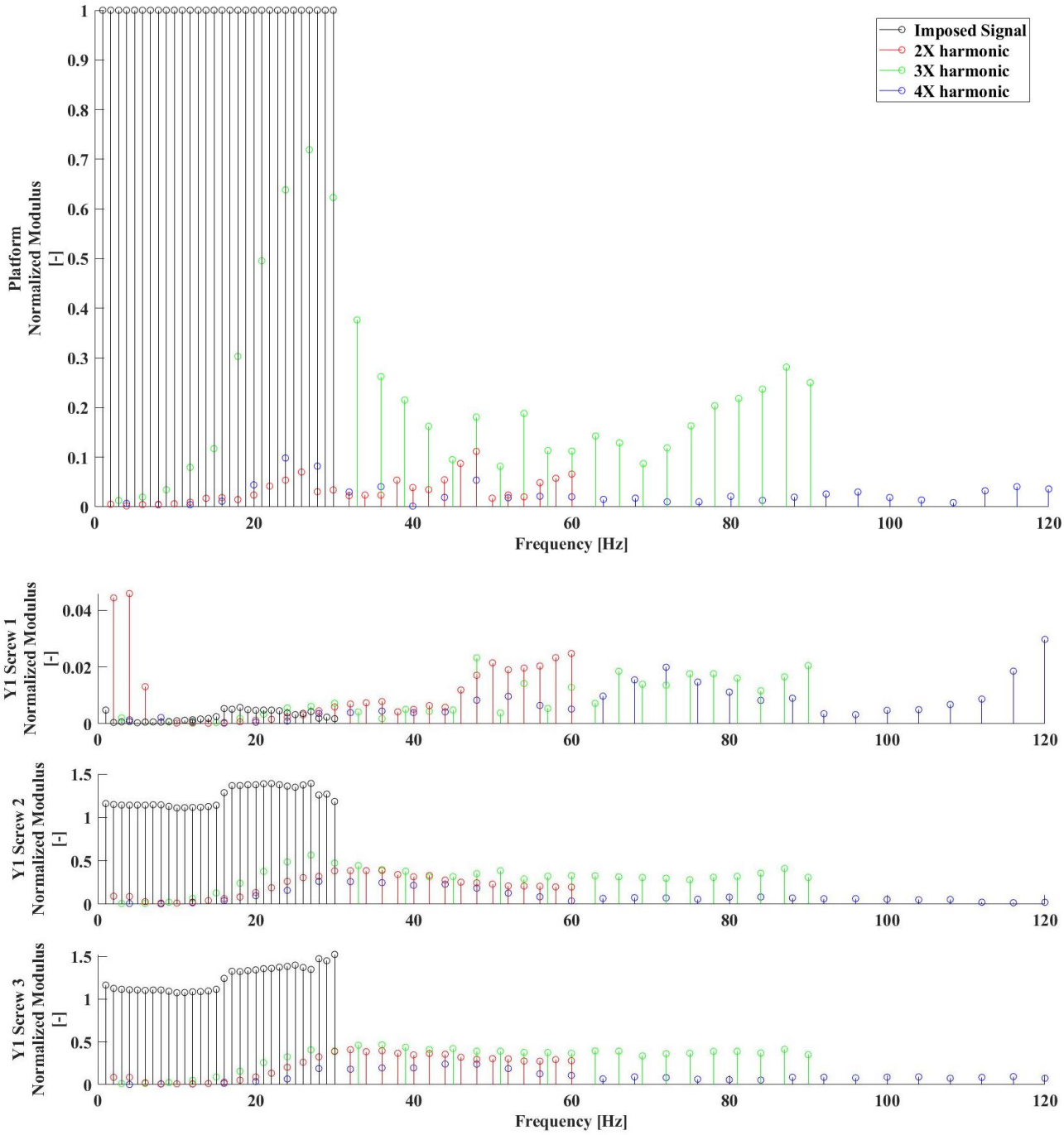

Figure 58: Plot of the nominal frequencies and multiple harmonics of the signals acquired on the moving platform and on the three actuators during the tests done by imposing a sinusoidal acceleration with an amplitude equal to 1 m/s^2 along the Y direction normalized by the fundamental frequency of the signal acquired at the centre of the moving platform

Figure 59 shows the results obtained from the sinusoidal tests done by imposing the excitation along the Y direction, with an amplitude of 5 m/s^2. The results are similar to the ones already shown for the X direction, at the same amplitude level. The maximum of the modulus of the 3X harmonic of the signals acquired on the platform is 0,36 and it is at the frequency of 27 Hz. The modulus of the

fundamental harmonic measured at the three actuators shows a sharp increase after the frequency of 26 Hz, exceeding the value of 4 at 29 Hz for the actuators 2 and 3.

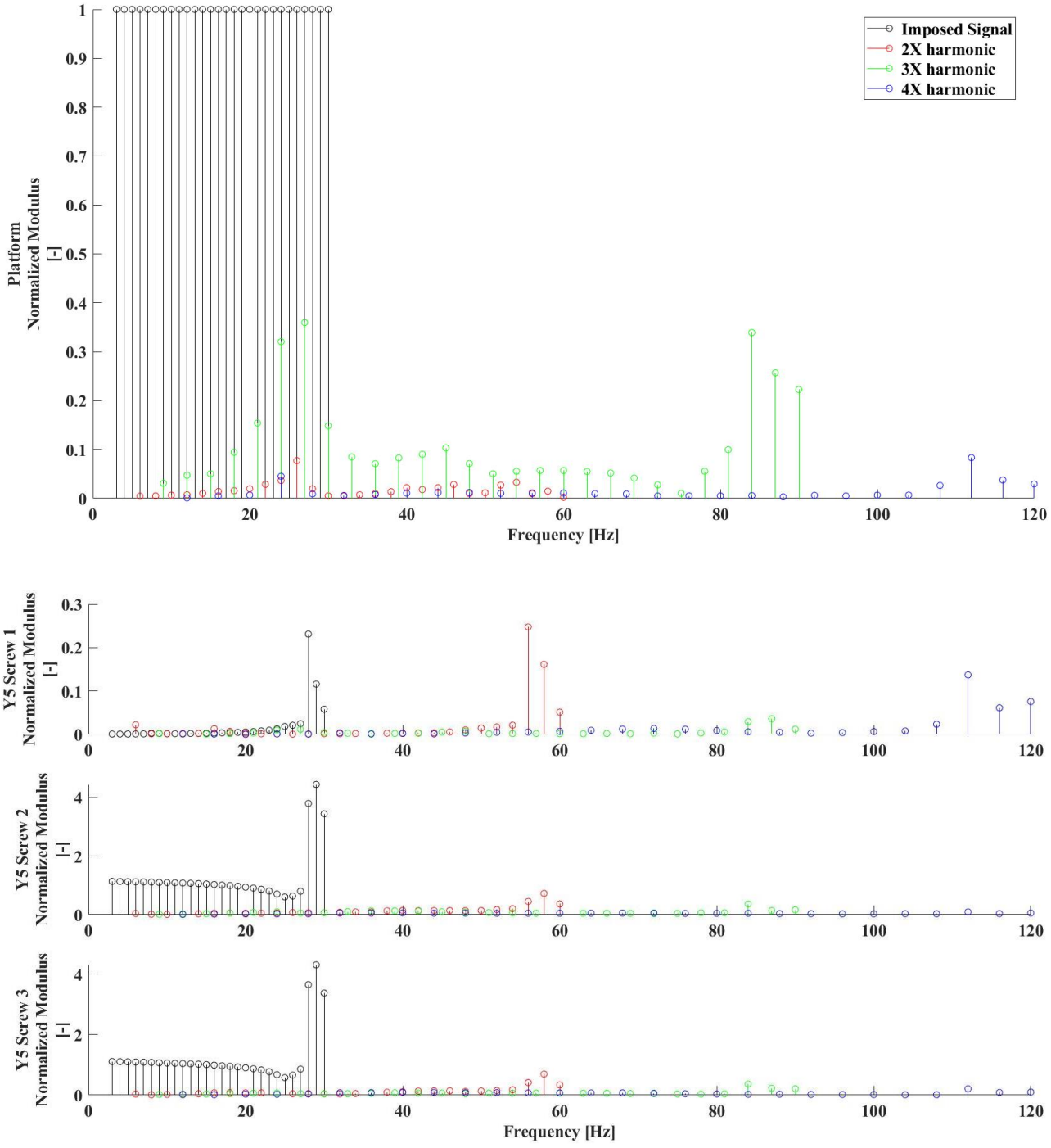

Figure 59: Plot of the nominal frequencies and multiple harmonics of the signals acquired on the moving platform and on the three actuators during the tests done by imposing a sinusoidal acceleration with an amplitude equal to 5 m/s^2 along the Y direction normalized by the fundamental frequency of the signal acquired at the centre of the moving platform

Figure 60 shows the results obtained from the sinusoidal tests done by imposing the excitation along the Z direction, with an amplitude of 1 m/s^2. The results are like the ones already shown for the other two directions, at the same amplitude level. The maximum of the modulus of the 3X harmonic of the signals acquired on the platform is 0,72 and it is at the frequency of 69 Hz. In the frequency range of interest, it is important to note a second peak, with a modulus of 0,69 at the frequency of 30 Hz. The moduli of the fundamental harmonic measured at the three actuators show non negligible differences after the frequency of 15 Hz. In the frequency range between 20 Hz and 30 Hz, the moduli of the fundamental frequencies at the actuator 1 increase, up to a value of 2 at the frequency of 23 Hz. The ones measured at the second actuator show a parallel decrease, reaching the minimum of 0,51 at the frequency of 23 Hz. Also, the ones measured at the third actuator show a decrease in that frequency range, reaching the minimum of 0,34 at the frequency of 23 Hz.

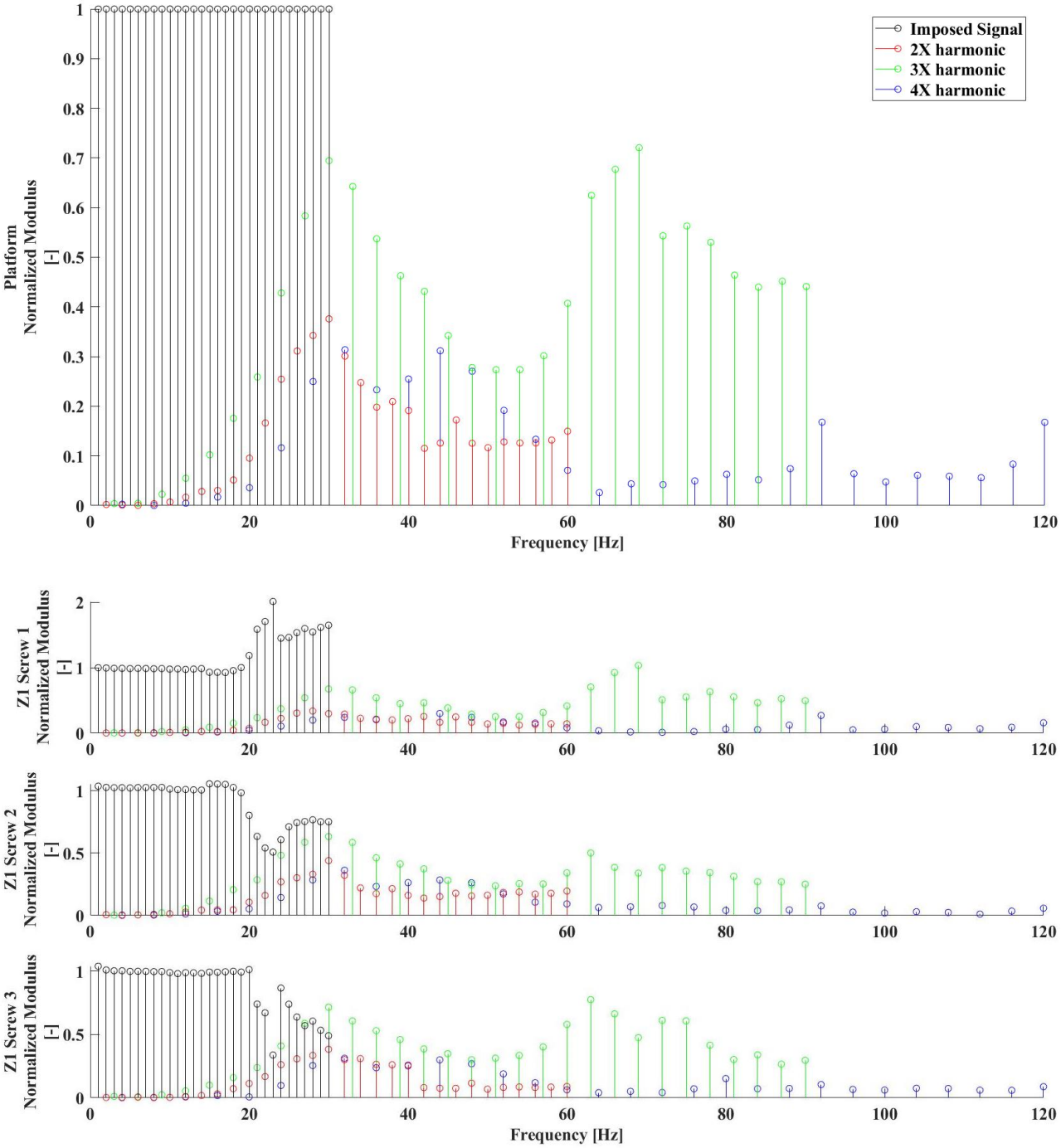

Figure 60: Plot of the nominal frequencies and multiple harmonics of the signals acquired on the moving platform and on the three actuators during the tests done by imposing a sinusoidal acceleration with an amplitude equal to 1 m/s^2 along the Z direction normalized by the fundamental frequency of the signal acquired at the centre of the moving platform

Figure 61 shows the results obtained from the sinusoidal tests done by imposing the excitation along the Z direction, with an amplitude of 5 m/s^2. The modulus of the 2X harmonic of the signals acquired on the platform shows a peak of 0,15 at the frequency of 38 Hz. The maximum of the modulus of the 3X harmonic of the signals acquired on the platform is 0,20 and it is at the frequency

of 32 Hz. The moduli of the fundamental harmonic measured at the three actuators show discrepancies between the actuators 1 and 2 after the frequency of 15 Hz. In that frequency range, the moduli of the fundamental frequencies at the actuator 1 decrease, reaching a value of 0,83 at the frequency of 25 Hz. The ones measured at the second actuator show a parallel increase, up to a value of 1,15 at the frequency of 23 Hz and 24 Hz.

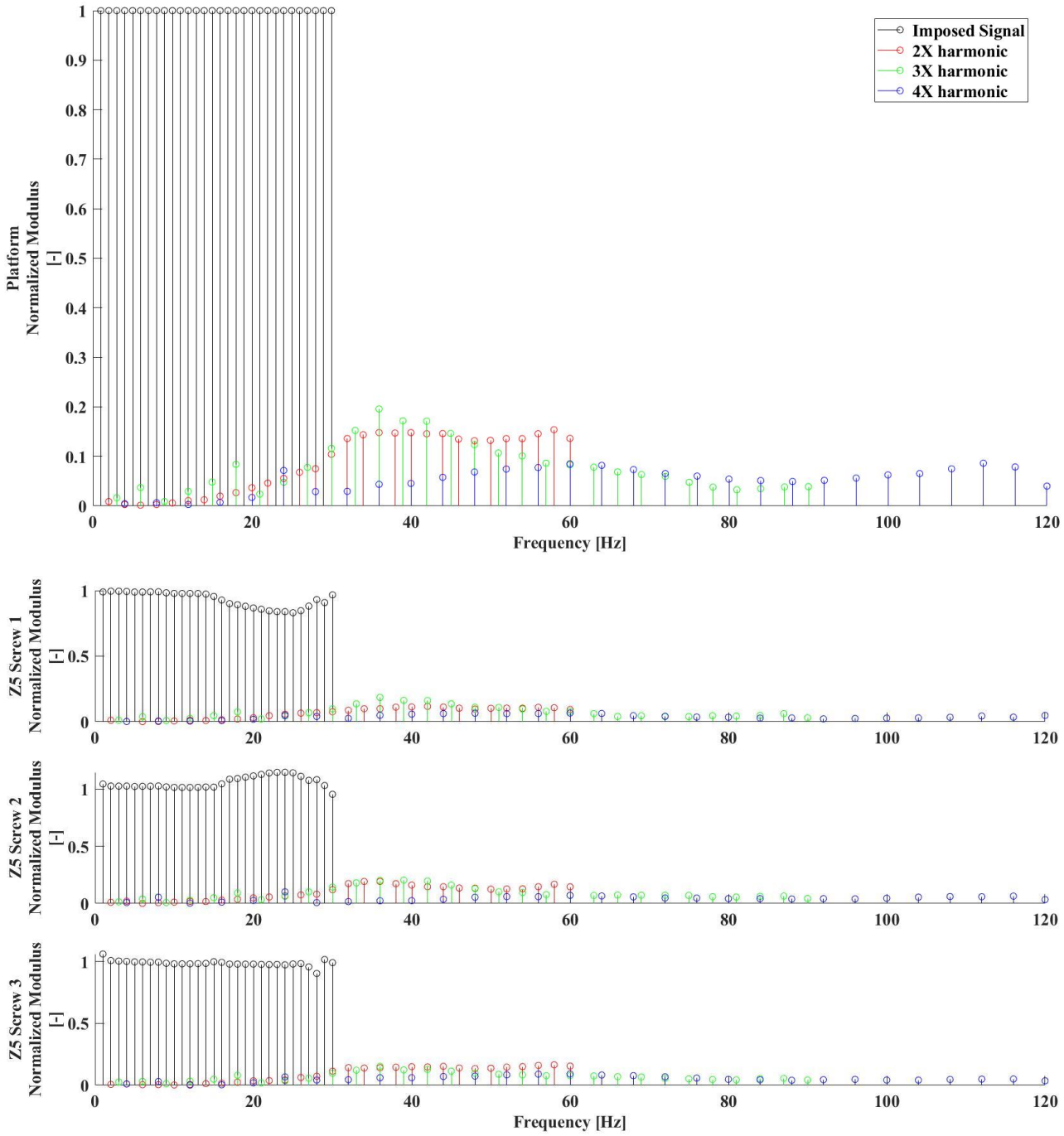

Figure 61: Plot of the nominal frequencies and multiple harmonics of the signals acquired on the moving platform and on the three actuators during the tests done by imposing a sinusoidal acceleration with an

amplitude equal to 5 m/s^2 along the Z direction normalized by the fundamental frequency of the signal acquired at the centre of the moving platform

3.3 Discussion

The tests done by imposing a pseudo-random signal along the three axis simultaneously proved that the shaker is able to generate an acceleration signal with a flat spectrum along all three spatial axes simultaneously, with and without a person standing on it, even over the frequencies for which it was created. Even though the design limit was set to 30 Hz, it was possible to perform tests with a bandwidth from 1 to 80 Hz: the root mean squared error between the modulus of the spectrum of the signal acquired by reference accelerometer and the one of the imposed signal are much lower than the ones reported in Table 9. The average ± standard deviation across the direction of motions is 6,9 ± 0,5 mm/s^2 and 5,5 ± 0,5 mm/s^2 for the unloaded and loaded case respectively.

However, the tests done by imposing a similar pseudo-random signal only along a single axis show crosstalk between the axes, which is larger when the signal is imposed along the horizontal plane. When the signal is imposed along the Z-axis the noise level along the X-axis shows very little dependence on the excitation amplitude, while the noise along the Y-axis increases proportionally with the amplitude of the acceleration, with a proportionality coefficient of 8%.

The moduli of the spectra of the acceleration signals acquired at the centre of the platform highlight how multiple harmonics decrease the quality of the signal generated. Across all the tests, it is possible to see that the 3X harmonic is the most relevant source of noise. Multiple harmonics can create further problems, when they match a resonance frequency of the machine.

The comparison between the amplitude of the acceleration signals acquired by the accelerometers placed across the moving platform shows a non-uniform behaviour of the platform, with differences of RMS comprised by -4% and 23% of the RMS of the acceleration signal acquired by the reference accelerometer. The phase differences between the spectra of the signal acquired by the accelerometers exceeds 150° when the signal is imposed along the horizontal plane, thus confirming a partial rotation of the moving platform along the horizontal axes.

The moduli of the spectra of the acceleration signals acquired at the centre of the platform and along the three actuators confirm that the 3X harmonic is the most relevant in the distortion of the sinusoidal signal. The tests done with a higher amplitude shows that the amplitude of the multiple harmonics, normalized by the amplitude of the modulus of the fundamental frequency is lower in respect to the one measured when imposing the signals with a nominal amplitude of 1 m/s^2. This decrease however is not proportional, as the mean percentage decrease of the maximum value of the

3X harmonic, measured at the centre of the platform is equal to 57%, in respect of an amplitude increased 5 times. The signals acquired on the actuators highlight unbalances on the modulus of the acceleration measured on them, giving further proof of the non-ideal motion of the platform when imposing a sinusoidal signal.

The inability of the Delta Shaker to generate a pure sinusoidal acceleration signal is shared with other electromechanical parallel manipulators, due to the practical difficulty of eliminating the static friction and the backlash between every mechanical joint. As an example, the acceleration was measured at the centre of the moving platform of the parallel robot R3000 produced by Mikrolar, when a sinusoidal signal was imposed along the vertical direction. As Figure 62 shows, the results obtained were similar to the one obtained by the machine proposed in this dissertation in terms of harmonic distortion, but the Mikrolar shaker has worst performances with random stimuli, given the absence of a closed-loop control that compensates for the non-ideal shaker frequency response function.

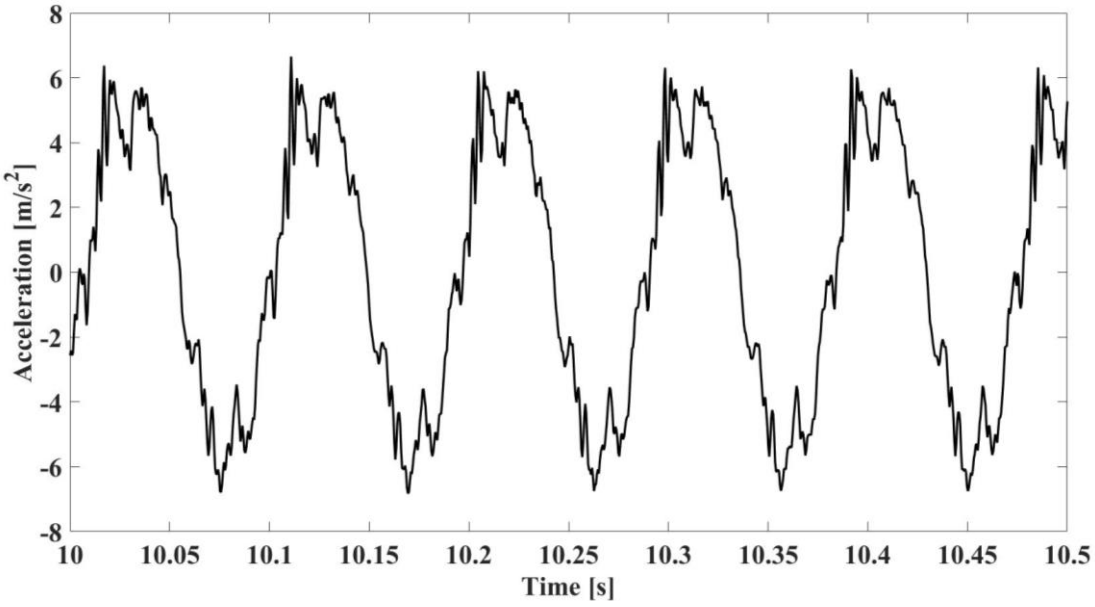

Figure 62: Example of time history of the acceleration signal measured at the centre of the moving platform of the parallel robot R3000 produced by Mikrolar, when imposing a sinusoidal vibration.

The tests previously explained can prove that the shaker is able to meet the design requirements and exceed them in terms of frequency bandwidth. The shaker performances however show shortcomings when generating a signal composed of a single frequency, thus limiting its employment in generating three-directional noise with a desired spectrum. The problems of crosstalk and partial rotation of the moving platform can be linked to a low stiffness of the transmission system. Given also the results obtained from the modal analysis, as it was discussed in 3.1.3, the stiffening of the rails of the ball screws may bring benefits also to the quality of the generated signal. The problems

linked to the multiple harmonics may be reduced by avoiding the frequency match with a resonance frequency of the machine, which means increasing the first natural frequency of the robot to a higher value. A new and improved control algorithm, able to consider the different characteristics of each actuator could also be beneficial to the capability of the machine in creating sinusoidal acceleration signals.

Chapter IV

4 2-D lumped-parameters model of the Foot-Ankle system to represent the transmissibility of vertical vibration and the vertical apparent mass

In addition to the machine required to characterize the response of the foot to vibration, it is also necessary to create the mathematical models to understand phenomena at the base of the different foot pathologies that can be linked to the vibration. For this reason, in parallel with the mechanical design and testing of the Linear Delta shaker, a 2D lumped parameter model of the foot-ankle system was created. The model was developed starting from transmissibility and apparent mass data available in the literature. The transmissibility was measured at five points on the foot under and the apparent mass was the one of standing subjects exposed to vertical vibration. The model was developed with single-axis vibration and it will be validated in the future under multiaxial vibration.

4.1 Data Collection Protocol

The complete description of the method used to collect the transmissibility functions data used for the model optimization can be found in [81]. A group of 21 people took part of the experiments, 6 females and 15 males. The main biometric data, expressed as average ± standard deviation, are the following: age of 24 ± 7.8 years, height of 175.6 ± 9.1 cm, mass of 70.1 ± 14.0 kg, and total foot length of 25.8 ± 2.0 cm. The subjects were asked to stand barefoot in a natural posture on the vibrating plate of a vibrating platform. The stimulus used was a sinusoidal sweep with constant velocity amplitude of 30 mm/s and the frequency range from 10 Hz to 200 Hz. The duration of the stimulus was 51 s. The response vertical velocity was measured on a total of 24 points on the right foot using a laser Doppler vibrometer. For modelling purposes, the 24 transmissibility functions were aggregated according to the similarities in the response, into five average functions, representing the toe, the forefoot, the mid foot, the ankle and the heel. Figure 63 shows the position of the measurements points and how they have been grouped together.

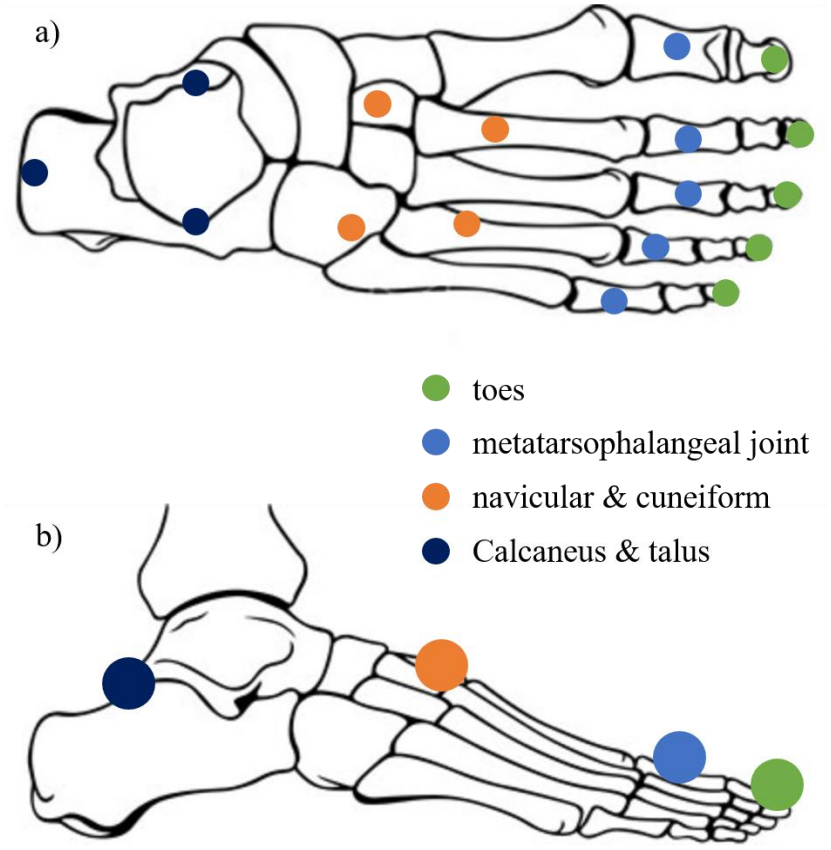

Figure 63: sketch of the bones composing a human right foot, with the position of the points in which the transmissibility functions were measured (a) and the indication how such measured functions were grouped together (b)

The data collection protocol used to measure the normalized vertical apparent mass of standing subjects used for the model optimization was derived from another study [82]. Ten male subjects were exposed to a vertical sine sweep from the frequency of 1 Hz to a frequency of 30 Hz, with a constant acceleration RMS equal to 1 m/s^2. The pressure distribution at the feet was measured through the pedar®-x system (novel GmbH, Ismaninger Str. 51, München, DE). The apparent mass functions measured through this system were then normalized by dividing them by the static mass of the corresponding subject. The anthropometric data of the subjects, expressed as mean ± standard deviation, are: age of 26 ± 0.9 years, height of 174.7 ± 5.0 cm and a mass of 73.5 ± 9.9 kg.

4.2 Model Description

Figure 64 shows the scheme of the proposed lumped-parameters model, as presented in [83]. Four rigid bodies compose the foot and ankle portion of the lumped parameters model proposed to reproduce the measured data. These segments represent respectively the toes (S_1), the metatarsal (S_2), the navicular and cuneiform (S_3), and the calcaneus and talus (S_4). The segments are hypothesised to

be rigid bodies with uniform mass distribution. The inertial and geometrical properties of the bodies (mass “m”, length “L” and moment of inertia “I”) are taken from literature values [84]-[86].

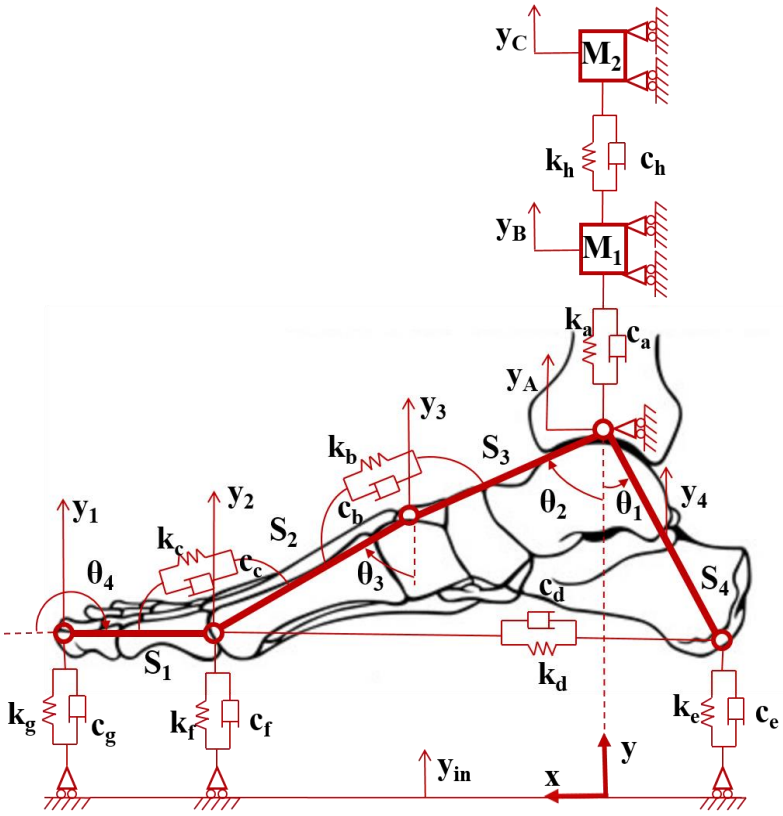

Figure 64: lumped parameters model proposed to represent the foot-ankle system and to reproduce the apparent mass of a standing person.

Table 24 shows the inertial values adopted. The bodies S_1 and S_2; and the bodies S_2 and S_3 are connected respectively by two angular viscous-elastic elements, identified with the subscripts “c” and b”. These elements represent the mechanical properties of the muscles and ligaments inside the foot. The distal ends of the segments S_2 and S_4 are connected by a linear viscous-elastic element, identified with the subscripts “d”, representing the plantar fascia, as in the models already presented in literature and discussed in the introduction. Three other viscous-elastic element, identified with the subscripts “g”, “f” and “e”, connect the distal ends of the segments S_1, S_2 and S_4 to the ground. These elements represent the mechanical properties of the biological tissues in contact with the ground.

Table 24: inertial and geometrical parameters of the four rigid bodies composing the model of the foot-ankle system

	S_1	S_2	S_3	S_4

m [kg]	0.098	0.196	0.294	0.294
L [m]	0.06	0.07	0.085	0.046
I [kg·m2]	15·10-7	14·10-6	1·10-6	28·10-5

The contribution of the rest of the human body is represented as the model 2a suggested by Matsumoto and Griffin [41]. Two masses, M_1 and M_2, are constrained to move only along the vertical axes, and are connected by a viscous-elastic element with properties k_h and c_h. The lower mass M_1 is connected to the hinge representing the ankle joint through another viscous-elastic element, whose properties are k_a and c_a. The nominal sum of these two masses is set to be equal to half of the average mass of the human body, i.e. 35 kg, under the hypothesis that the weight is shared equally among the two feet. The mass M_1 is set to be equal to 57,4% of the total nominal mass, while M_2 is set to be equal to 39,4% of the total nominal mass.

The motion of the system can be described through a total of seven degrees of freedom (DOF). The first three DOF are the vertical displacements of the two masses and of the ankle, respectively y_C, y_B and y_A. The other four degrees of freedom are: θ_1, i.e. the angle between the segment S_4 and the vertical axis in the anti-clockwise direction. θ_2, i.e. the angle between the segment S_3 and the vertical axis in the clockwise direction. θ_3, i.e. the angle between the segment S_2 and the vertical axis in the clockwise direction and θ_4, i.e. the angle between the segment S_1 and the horizontal axis in the clockwise direction. The initial state of the system is the static equilibrium, and the initial values of the angles are respectively 49°, 69°, 82° and 180°, derived from the literature. An additional degree of freedom, y_{in}, is the vertical displacement of the ground and it is constrained to move in the vertical direction to simulate the action of the vibrating platform.

4.3 Parameters Optimization

4.3.1 Method

The first step of the method is to describe the vertical displacements of the five points of the model corresponding to the five points in which the transmissibility functions have been experimentally measured. The transmissibility function measured at the toe, $\tilde{T}_1$, is represented in the model, T_1, by the ratio between the vertical displacement of the distal end of the S_1 segment of the model, called y_1, and the constrained degree of freedom, y_{in}. The transmissibility function measured at the forefoot, $\tilde{T}_2$, is represented in the model with the function T_2, the ratio between the vertical displacement of the distal end of the segment S_2, i.e. y_2, and y_{in}. The transmissibility function measured at the midfoot, $\tilde{T}_3$, corresponds in the model with the function T_3 ratio between the vertical displacement of the distal end of the segment S_3, i.e. y_3, and y_{in}. The transmissibility function

measured at the ankle, $\widetilde{T}_5$, is represented by the function T_5, i.e. the ratio between the vertical displacement of the ankle, called y_5, and y_{in}. The transmissibility function measured at the heel, $\widetilde{T}_4$, corresponds in the model to the function T_4, i.e. the ratio between the vertical displacement of the midpoint of the segment S_4, called y_4, and y_{in}. The normalized apparent mass reconstructed by the model, called am, is the sum of all the forces exchanged by the model and the constrained degree of freedom, i.e. the sum of the forces generated by the viscous-elastic elements e, f and g; divided by the static mass of the model. The notation $\widetilde{am}$ denote the experimentally measured normalized apparent mass function.

After having obtained the correspondence between the model and the experimental data, it is necessary to compute the theoretical transmissibility functions obtained from the model. The method used is the standard Lagrangian approach.

The vector "$\underline{v}$" of the degrees of freedom of the system can be divided in the free degrees, of freedom, $\underline{v}_{dof}$ and the constrained degrees of freedom, $\underline{v}_{in}$, as follows in equation 4.1 (see Figure 64 for the notation):

$$\underline{v} = \begin{bmatrix} y_A \\ y_B \\ y_C \\ \theta_1 \\ \theta_2 \\ \theta_3 \\ \theta_4 \\ \hline y_{in} \end{bmatrix} = \begin{bmatrix} \underline{v}_{dof} \\ \hline \underline{v}_{in} \end{bmatrix} \tag{4.1}$$

The kinetic energy of the system can be expressed as follows in equation 4.2:

$$E = \frac{1}{2}\mathrm{M}_1\dot{y}_B^2 + \frac{1}{2}\mathrm{M}_2\dot{y}_C^2 + \frac{1}{2}\sum_{j=1}^{4} m_j(\dot{x}_j^2 + \dot{y}_j^2) + \frac{1}{2}\sum_{j=1}^{4} I_j\dot{\theta}_j^2, \tag{4.2}$$

In the previous equations 4.2 m_j and I_j express the mass and the moment of inertia of the j-th rigid body of the model. The numeric values can be found in Table 24. $\dot{x}_j$ and $\dot{y}_j$ are the velocity components of the centre of mass of the j-th rigid body in the system, in the fixed reference system. Such quantities can be expressed as functions of the degrees of freedom of the system shown in equation 4.1 through simple geometrical consideration. Such relationships are non-linear; however they have been linearized around the static equilibrium position, using a Taylor Polynomial approximation truncated at the first order. The linearization process is justified by the small nonlinear components reported by Tarabini et al. [87] and allowed a simpler mathematical description of the problem, hence a reduction of the computation time and effort.

The elastic and dissipative energy of the systems can be expressed as equations 4.3 and 4.4 respectively show:

$$U = \frac{1}{2}\sum_{n=a}^{h} k_n \Delta_n^2, \tag{4.3}$$

$$D = \frac{1}{2}\sum_{n=a}^{h} c_n \dot{\Delta}_n^2 \tag{4.4}$$

Where Δ_n and $\dot{\Delta}_n$ are, in order, the deformation of the n-th elastic parameter and its time derivative. These quantities too can be expressed as functions of the degrees of freedom of the system through simple geometrical considerations. These functions also have been linearized.

The equations of motion of the system can be computed from the quantities described above through the Lagrange Equation, as equation 4.5 shows, and then expressed in the matrix form, in equation 4.6:

$$\frac{d}{dt}\left(\frac{\partial E}{\partial \underline{\dot{v}}}\right) - \frac{\partial E}{\partial \underline{v}} + \frac{\partial U}{\partial \underline{v}} + \frac{\partial D}{\partial \underline{\dot{v}}} = \underline{0} \tag{4.5}$$

$$[M]\underline{\ddot{v}} + [C]\underline{\dot{v}} + [K]\underline{v} = \underline{0} \tag{4.6}$$

Knowing that the last degree of freedom of the system, y_{in}, is constrained, it is possible to divide the elements of the matrices shown in equation 4.6 accordingly:

$$[M] = \begin{bmatrix} [M_{FF}] & [M_{FC}] \\ [M_{CF}] & [M_{CC}] \end{bmatrix} \tag{4.7}$$

$$[C] = \begin{bmatrix} [C_{FF}] & [C_{FC}] \\ [C_{CF}] & [C_{CC}] \end{bmatrix} \tag{4.8}$$

$$[K] = \begin{bmatrix} [K_{FF}] & [K_{FC}] \\ [K_{CF}] & [K_{CC}] \end{bmatrix} \tag{4.9}$$

Considering this division of the matrices, it is possible to rearrange equation 4.6 as equation 4.10:

$$[M_{FF}]\underline{\ddot{v}}_{dof} + [C_{FF}]\underline{\dot{v}}_{dof} + [K_{FF}]\underline{v}_{dof} = -\left([M_{FC}]\underline{\ddot{v}}_{in} + [C_{FC}]\underline{\dot{v}}_{in} + [K_{FC}]\underline{v}_{in}\right). \tag{4.10}$$

Under the hypothesis of sinusoidal displacement input, the vibration transmissibility between the constrained degree of freedom and the free degrees of freedom, called T_{dof}, can be therefore computed as a function of the angular frequency Ω, as equation 4.11 shows:

$$T_{dof}(\Omega) = \frac{\underline{v}_{dof}}{\underline{v}_{in}} = \frac{-\left(-\Omega^2[M_{FC}] + i\Omega[C_{FC}] + [K_{FC}]\right)}{\left(-\Omega^2[M_{FF}] + i\Omega[C_{FF}] + [K_{FF}]\right)} \tag{4.11}$$

where "*i*" is the imaginary unit.

The transmissibility functions used in the optimization of the parameters of the model can be then computed as the linear combination of the transmissibility functions computed through equations 4.11 for the degrees of freedom. The weights of the linear combinations are the terms coming from the linearization of the geometric relationships between degrees of freedom and the points in which the transmissibility functions must be computed, shown here in equations 4.12 – 4.16.

$$y_1 = y_a - l_3 \cdot \cos(\theta_2) - l_2 \cdot \cos(\theta_3) + l_1 \cdot \sin(\theta_4) \tag{4.12}$$

$$y_2 = y_a - l_3 \cdot \cos(\theta_2) - l_2 \cdot \cos(\theta_3) \tag{4.13}$$

$$y_3 = y_a - l_3 \cdot \cos(\theta_2) \tag{4.14}$$

$$y_4 = y_a - \frac{l_4}{2} \cdot \cos(\theta_1) \tag{4.15}$$

$$y_5 = y_a \tag{4.16}$$

The equations describing the relationship between the independent degrees of freedom of the system and the motion of the points of the systems in the fixed reference system x-y have been linearized around the static equilibrium position.

The theoretical transmissibility function obtained from the model are parametric, as the numerical values of the elastic and viscous properties of the lumped elements are unknown. An optimization process was used to obtain these values. This process was articulated in two steps. The first step involved a genetic algorithm, and the values resulting from the first step were used as initial values for the second step, which involved a nonlinear least-squares solver. Both steps were carried out using functions available in MATLAB R2017b, respectively "*ga*" and "*lsqcurvefit*". Both methods shared the same function to be minimized, called "*e*", which is shown in equation 4.17.

$$e = \sqrt{\sqrt{w_{am} \cdot \left(\sum_{f=2}^{20} \left| \left(\widetilde{am}(f) - am(f) \right)^2 \right| \right)} + \sqrt{w_T \cdot \left(\sum_{i=1}^{5} \left(\sum_{f=10}^{100} \left| \left(\tilde{T}_i(f) - T_i(f) \right)^2 \right| \right) \right)}} \tag{4.17}$$

The above function "*e*" represents the average reconstruction error in a least square sense, of both transmissibility and apparent mass. The apparent mass is considered only in the frequency range between 2 Hz and 20 Hz and the transmissibility functions are considered only in the frequency range between 10 Hz and 100 Hz. Both kind of functions are considered at steps of 1 Hz. Only a portion of the measured frequency range is considered because the dispersion of the data increases at higher frequencies, therefore decreasing their reliability in this optimization process. w_{am} and w_T are the weights associated to the reconstruction errors of those functions. Such weights are necessary as only 19 points are available for the apparent mass, while 455 points are available for the transmissibility

functions. Therefore, if no weight were used, the apparent mass would have a minimal role in the computation of the optimal values. To give to both kind of functions the same weight, w_{am} is set to be equal to 1/19, while w_T is set to be equal to 1/455. The initial values of the parameters used for the optimization using the genetic algorithm procedure were randomized. Different consecutive runs of the optimization procedure were implemented to ensure the convergence. The lower boundary of the parameters was set to be equal to 0 at this stage, while the upper boundary for the parameters was set to be equal to 10^7. For the second optimization stage, the lower boundary for the parameters was set to be equal to half of the starting value, while the upper boundary was set to be equal to three halves of the starting value. The mean quadratic reconstruction error, called ε, was computed for each function of interest (five transmissibility and normalized apparent mass) according to equation 4.18:

$$\varepsilon = \sqrt{\frac{1}{N}\sum_{f=f_{min}}^{f_{MAX}} \left|\tilde{F}(f) - F(f)\right|^2} \tag{4.18}$$

where $\tilde{F}$ is one of the experimentally measured functions, F is the corresponding function computed through the model using the optimized parameters, f is the frequency, ranging from the minimum f_{min} to the maximum f_{max}, evaluated in a N number of points. Given that the functions are imaginary, the parameter ε was computed for both modulus and phase of each function.

The same optimization process has been applied on the transmissibility and apparent mass curves measured for each subject, instead than on the curves averaged between all the subjects [88]. The average stiffness and damping values obtained for all the subject have then been computed and compared with the ones obtained from the average functions.

Additionally, the optimization process has been repeated by changing the weight used to compute the optimization function. This second optimization process only considered the transmissibility functions. Therefore, w_{am} is set to be equal to 0, while w_T is set to be equal to 1.

4.3.2 Results

Table 25 contains the numerical values of the parameters obtained through the optimization process.

Table 25: Stiffness (k_i) and damping(c_i) values resulting from the optimization process are presented with their relative units of measurement

Parameter	Unit	Numerical value
k_a	$N.m^{-1}$	$1{,}06 \cdot 10^{6}$
k_b	$N.rad^{-1}$	$2{,}60 \cdot 10^{1}$
k_c	$N.rad^{-1}$	$2{,}16 \cdot 10^{2}$
k_d	$N.m^{-1}$	$2{,}63 \cdot 10^{4}$
k_e	$N.m^{-1}$	$2{,}78 \cdot 10^{5}$
k_f	$N.m^{-1}$	$1{,}00 \cdot 10^{6}$
k_g	$N.m^{-1}$	$2{,}30 \cdot 10^{4}$
k_h	$N.m^{-1}$	$8{,}4 \cdot 10^{4}$
c_a	$Ns.m^{-1}$	$6{,}52000 \cdot 10^{5}$
c_b	$Ns.rad^{-1}$	0,20
c_c	$Ns.rad^{-1}$	$3{,}43 \cdot 10^{6}$
c_d	$Ns.m^{-1}$	$1{,}50 \cdot 10^{3}$
c_e	$Ns.m^{-1}$	$4{,}17 \cdot 10^{2}$
c_f	$Ns.m^{-1}$	0,20
c_g	$Ns.m^{-1}$	$4{,}82 \cdot 10^{3}$
c_h	$Ns.m^{-1}$	$1{,}78 \cdot 10^{3}$

Through the parameters previously listed, the mean reconstruction quadratic error "ε", computed as in equation 4.18 is equal to 0.3 ± 0.1 for the modulus and 0.3 ± 0.3 rad for the phase (mean and standard deviation computed across the six functions). Figure 65 contains the mean reconstruction quadratic error "ε" associated to each function and shows the comparison between the transmissibility and normalized apparent mass functions computed by applying the optimized stiffness and damping parameters values to the model, and the curves obtained experimentally. The curves obtained experimentally are expressed in terms of average curve and uncertainty bands, computed as the standard deviation of the curves for each frequency, multiplied by two. As it is possible to see, most of the modelled curves are contained in the uncertainty bands of the experimental data. The main exceptions are the moduli of the transmissibility functions of the ankle and of the rear foot. For those functions, the model underestimates the measured values for the frequency range from 10 Hz to 15 Hz. Moreover, the modelled apparent mass is able to describe the main resonance at the measured frequency, which is 5 Hz; however, the peak in the modulus is close to the minimum

boundary of the uncertainty band. The phase of the reconstructed apparent mass function is also close to the upper uncertainty boundary in the frequency range between 5 Hz and 8 Hz.

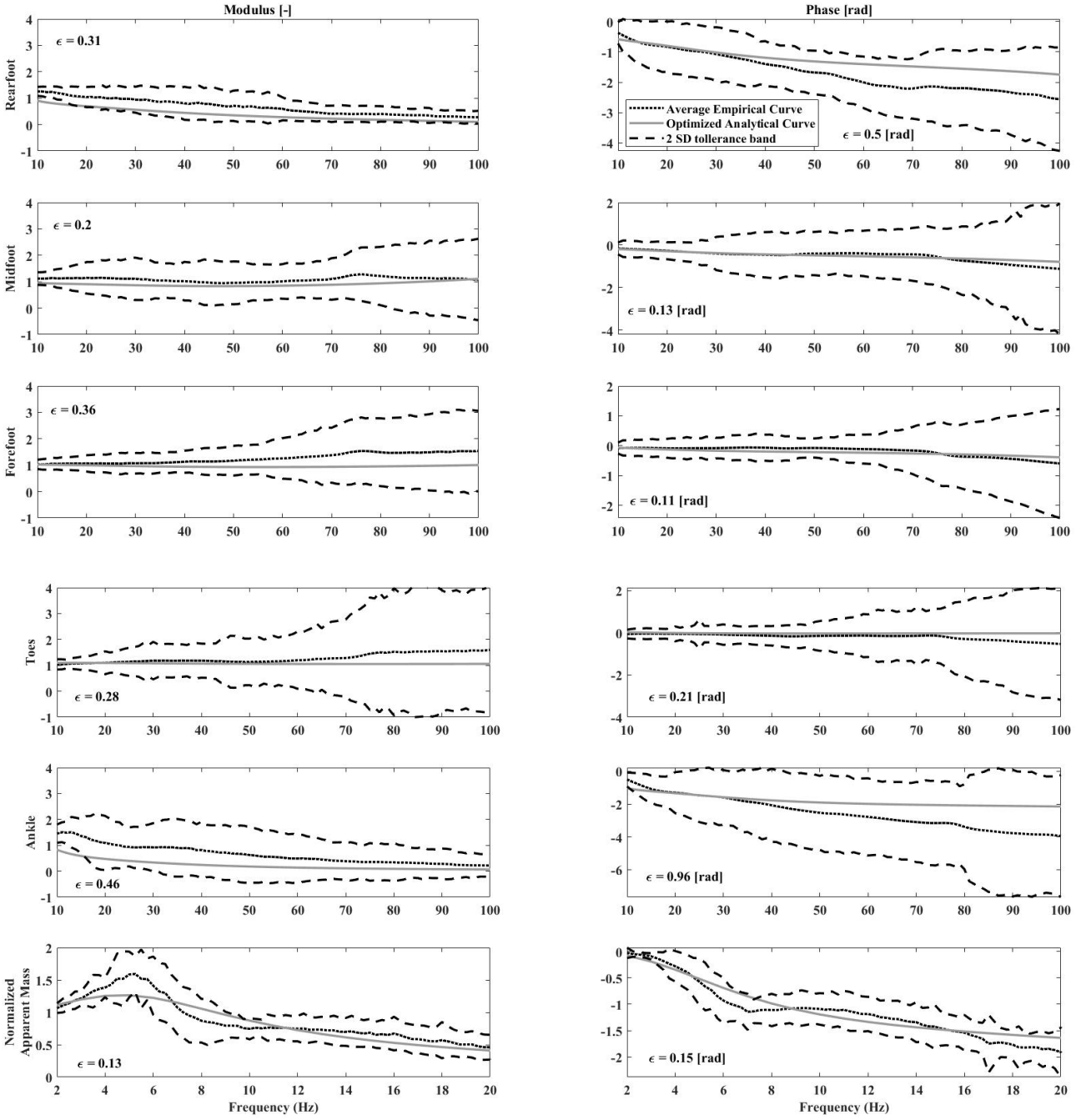

Figure 65: comparison between the transmissibility functions and normalized apparent mass, computed by applying the optimized values to the lumped-parameters mechanical model, and the experimental ones (average and uncertainty expressed as ± 2 SD), in terms of modulus and phase

Table 26 compares the mean quadratic reconstruction error obtained by optimizing the model using the average experimental curves, and by optimizing the model for each subject, and averaging the obtained values of the parameters. As it is possible to see, the results are mixed. In fact, one method

do not provide consistently a lower error than the other. In particular, the mean quadratic reconstruction error of the apparent mass obtained by optimizing the model using the average experimental function is about 35% of the one obtained by optimizing the curves measured for each subject.

Table 26: Comparison between the mean quadratic reconstruction error resulting from the optimization of the averaged curves, and the one resulting from the optimization of the curves measured for each subject

Mean quadratic reconstruction error ε						
	Heel	Forefoot	Tip toes	Midfoot	Ankle	Apparent mass
single subject optimization	0,06	0,10	0,23	0,23	0,07	0,31
multiple subject optimization	0,01	0,30	0,45	0,45	0,02	0,11

Table 27 contains the second set of numerical values of the parameters obtained through the optimization process.

Table 27: Stiffness (k_i) and damping (c_i) values resulting from the second optimization process are presented with their relative units of measurement

Parameter	Unit	Numerical value
k_a	$N.m^{-1}$	$1,5 \cdot 10^{2}$
k_b	$N.rad^{-1}$	$5,6 \cdot 10^{1}$
k_c	$N.rad^{-1}$	4,7
k_d	$N.m^{-1}$	$3,4 \cdot 10^{3}$
k_e	$N.m^{-1}$	$9,6 \cdot 10^{3}$
k_f	$N.m^{-1}$	$1,5 \cdot 10^{5}$
k_g	$N.m^{-1}$	$3,3 \cdot 10^{2}$
k_h	$N.m^{-1}$	$1,0 \cdot 10^{7}$
c_a	$Ns.m^{-1}$	3,4
c_b	$Ns.rad^{-1}$	0,2
c_c	$Ns.rad^{-1}$	0,3
c_d	$Ns.m^{-1}$	$2,6 \cdot 10^{1}$
c_e	$Ns.m^{-1}$	$4,2 \cdot 10^{1}$
c_f	$Ns.m^{-1}$	0,0
c_g	$Ns.m^{-1}$	$1,1 \cdot 10^{2}$

c_h	$Ns.m^{-1}$	$8{,}4 \cdot 10^5$

Through the parameters previously listed, the mean reconstruction quadratic error "ε", computed as in equation 4.18 is equal to 0.12 ± 0.07 for the modulus and 0.20 ± 0.14 rad for the phase (mean and standard deviation computed across the five transmissibility functions). Figure 66 contains the mean reconstruction quadratic error "ε" associated to each function and shows the comparison between the transmissibility functions computed by applying the optimized stiffness and damping parameters values to the model, and the curves obtained experimentally.

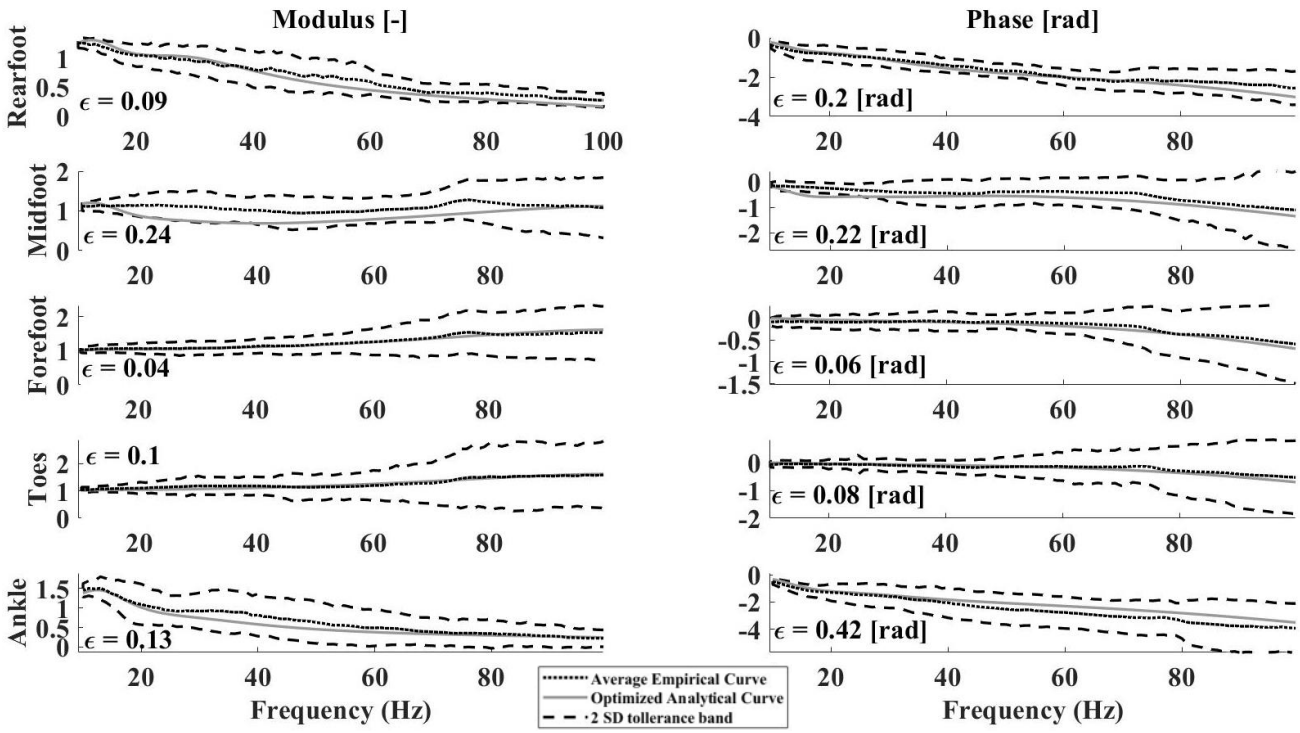

Figure 66: comparison between the transmissibility functions, computed by applying the second set optimized values to the lumped-parameters mechanical model, and the experimental ones (average and uncertainty expressed as ± 2 SD), in terms of modulus and phase

4.4 Sensitivity Analysis

4.4.1 Method

A sensitivity analysis was implemented to evaluate the effect of uncertainty on the optimized stiffness and damping parameters of the model on the resulting functions. The sensitivity analysis is based on the Monte Carlo method. It was hypothesised that each parameter belongs to a normal distribution with mean equal to the optimized value of the parameter and standard deviation equal to 20% of that same value. One hundred different sets, independent from each other, have been randomly generated, and used to compute the resulting apparent mass and transmissibility functions.

The parameter "COV" was used to assess the outcome of this test. Such parameter is computed for each function F at different frequencies, f, as equation 4.19 shows:

$$COV_F(f) = 100 \cdot \frac{\sigma_F(f)}{F(f)} \tag{4.19}$$

where $F(f)$ if the value of the function F evaluated at the frequency f using the optimized parameters, and $\sigma_F(f)$ is the standard deviation of the values of the same function F resulting from the 100 different sets of parameters, computed at frequency f. Such frequencies are 20, 40, 60, 80 and 100 Hz for the transmissibility and 4, 8, 12, 16 and 20 Hz for the apparent mass.

4.4.2 Results

Figure 67 shows the comparison between the experimental transmissibility and apparent mass functions, expressed as mean curves and an uncertainty band equal to the standard deviation obtained at each frequency multiplied by two, and 100 curves computed by extracting the parameters from normal distribution with mean equal to the ptimized parameter and standard deviation equal to 20%

of that value. As it is possible to see, the variability in the modelled curves resulting from such perturbation is lower than the experimental intersubject variability.

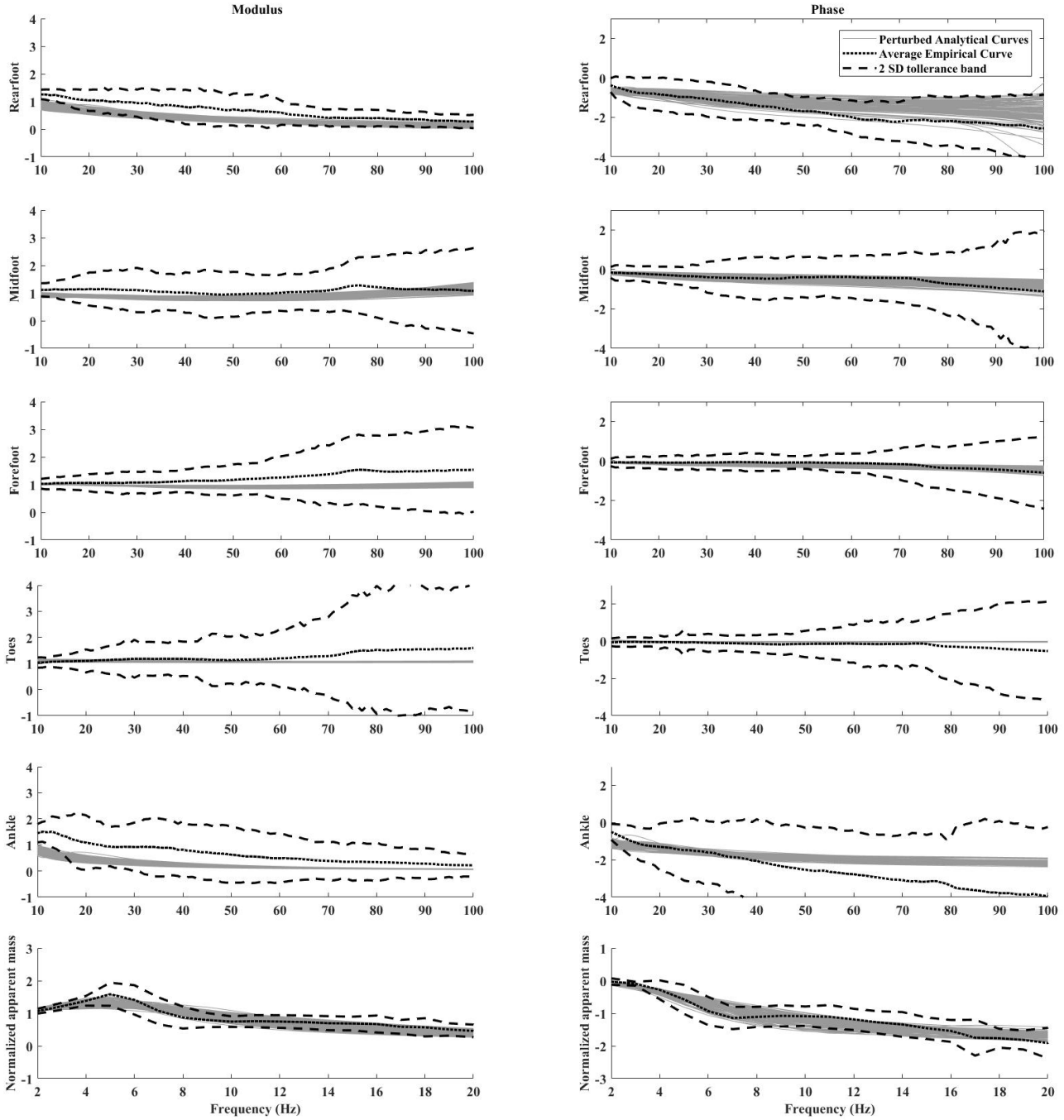

Figure 67: comparison between the variability of the transmissibility functions and normalized apparent mass, computed by applying the perturbed values to the lumped-parameters mechanical model, and the experimental ones (average and uncertainty expressed as ± 2 SD), in terms of modulus and phase

Figure 68 shows the comparison between the parameter COV computed as for equation 4.19 for the experimental curves and for the 100 different curves obtained through the Monte Carlo method

for the sensitivity analysis. The effect of variability of the parameters of the model is more relevant for the moduli than for the phases, for the reconstructed transmissibility functions, in fact the COV for the moduli, expressed as mean ± standard deviation, is 9,2±8,9; while for the phases is 22,8±14. Regarding the apparent mass, the variability of the parameters of model has a comparable effect on both the modulus and the phase. In fact, the COV, again expressed as mean ± standard deviation, is 11,8±4,8 for the modulus; while for the phase is 10,5±5,5. The COV computed for the moduli and the phases of the measured transmissibility functions is always higher than the one computed for the moduli of the perturbed analytical transmissibility functions, as previously shown. Regarding the variability of the apparent mass, the COV of the modulus of the measured apparent mass is 11,7±5,0; therefore, it is compatible with the modelled variability. The COV of the phase of the measured apparent mass is higher than the COV of the phase of the modelled function.

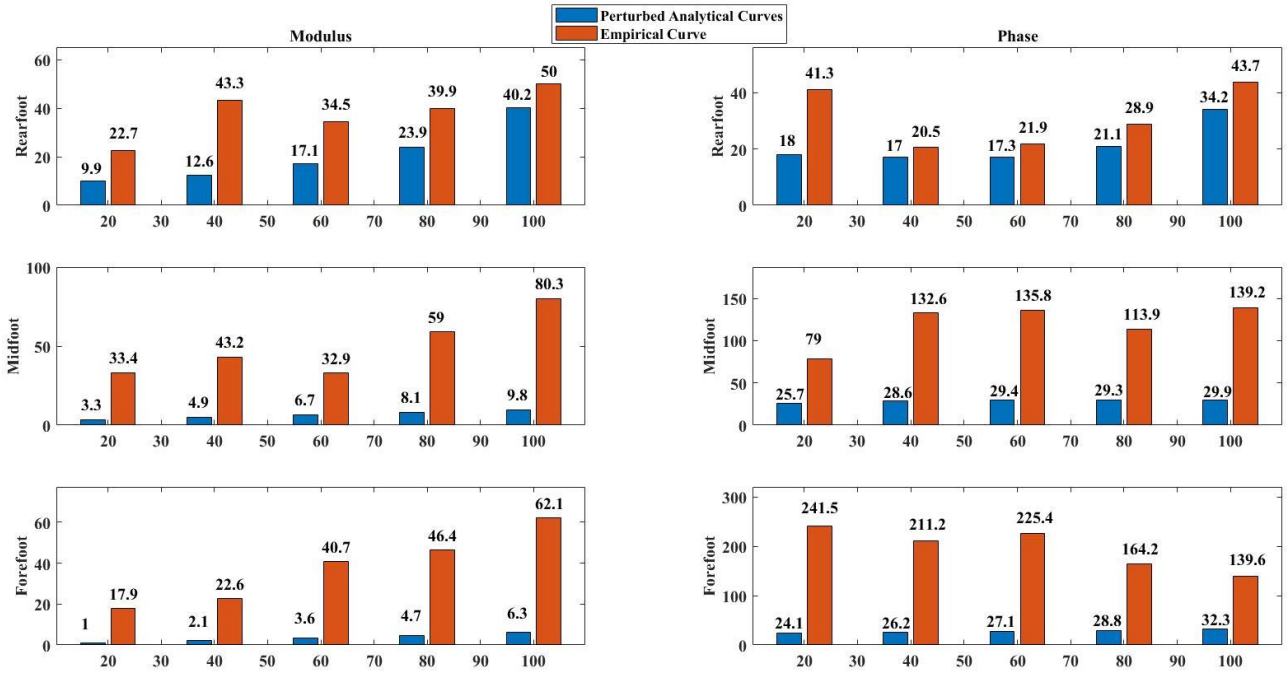

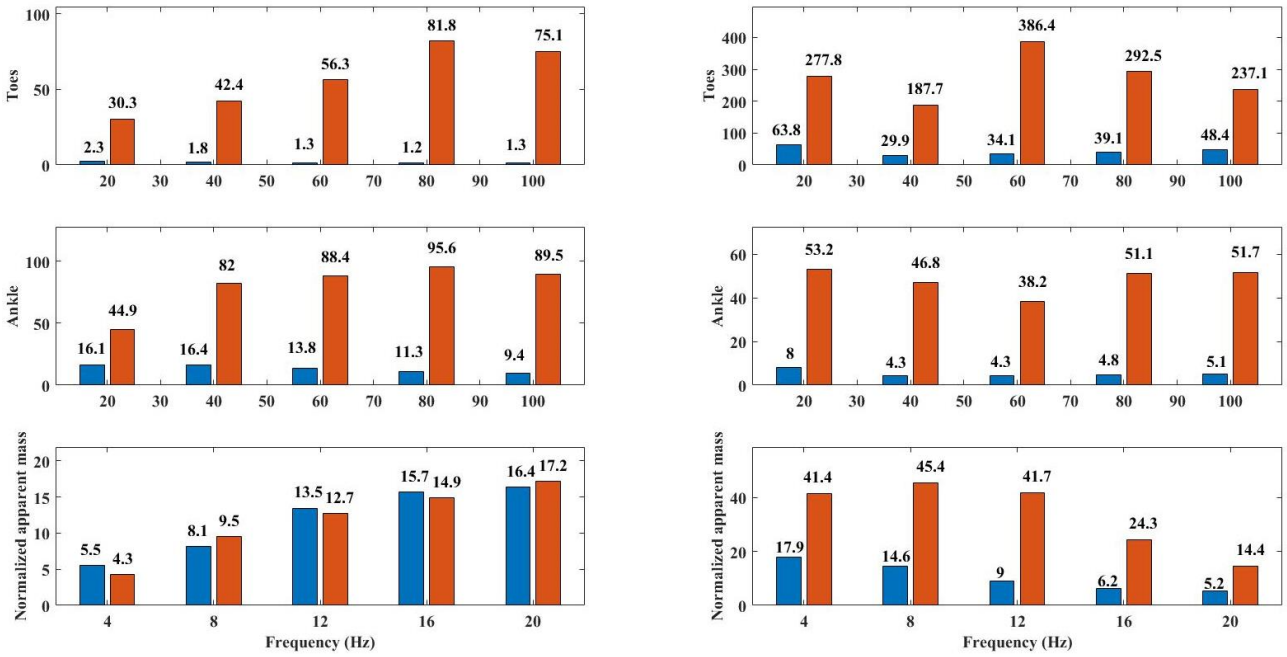

Figure 68: comparison between the experimental variability and the effect of variability of the parameters of the model on transmissibility and apparent mass functions

4.5 Discussion

As the results of the optimization process show, the proposed model reproduces the general behaviour of the Foot-Ankle System, in terms of vertical vibration transmissibility. Moreover, the model is also able to reproduce the vertical apparent mass of a standing person. The same optimization process has been applied to the curves measured for each subject, however the results obtained in this way are not consistently better than the other. Therefore, it is not possible to say that one method is to be favoured. A larger data set will be necessary to solve this modelling issue. The sensitivity analysis implemented through the Monte Carlo method also confirm the robustness of the proposed model, as an uncertainty of 20% added to the value of the parameters resulted in a variability of the modelled functions lower than the experimental variability. The model can be therefore used to investigate the effect of various materials to be used as insoles on the transmissibility at the foot. This can be done by adding the mechanical stiffness and damping properties of such materials to the model, by interposing three other springs and dampers elements between the ground and the elements “g”, “f” and “e”. Zadpoor et al. [36] showed the shortcomings of using passive lumped-parameters models to represent the response of the human body to mechanical stimuli; however their work is applied to modelling the response of the whole body, and in dynamic conditions (i.e. while running), under the hypothesis that the main muscles act to minimize the vibration transmitted to the head. For this reason, it is possible to say that the approach proposed can be still valid for modelling the response of the

extremities of the lower limbs to mechanical vibration, in static conditions. While the effect of the main muscles chains of the human body may not be as relevant for this application, the mechanical properties of the skin may play a major role, as they become more relevant at increasing frequencies, as shown by Lundström [89]. This relevance is reflected in the dispersion of the data increasing as the frequency increases, both in the empirical and in the perturbed analytical curves.

Regarding the numerical values of the stiffness and damping parameters, it is important to state that they are the result of a mathematical optimization problem. The outcome of this optimization process is influenced by the optimization function, as to be expected. In fact, the values obtained change when the apparent mass function is considered or not. Moreover, the initial upper and lower boundaries for such optimization variables were set to be wide apart, to let the genetic algorithm explore a wide range of values and obtain the minimum error possible. Moreover, the lumped parameters model, although more complex than the other similar models proposed in literature, is still composed of a finite number of elements, whose number is still not comparable with the number of anatomical features composing a human foot. For these reasons, even though the inertial properties of the rigid bodies were taken from literature values of the corresponding anatomical districts, it is not possible to state that the numerical values of the optimized parameters are representative of the mechanical properties of a given anatomical feature, as other authors proposed.

The proposed model is limited in its use by the optimization process itself, as the parameters have been computed for a specific objective. For this reason, the model is not guaranteed to reproduce the response of the foot in different conditions than a standing person standing upright in a neutral posture, subjected to vertical whole-body vibration. In fact, different postures have a non-negligible influence on the vibration transmissibility, as shown by Goggins et al. [81]. Changing the objective function of the optimization process, aiming at representing the transmissibility and apparent mass functions according to different postures would likely results in different values of the stiffness and damping parameters, however this would not change the validity of the approach. Another limitation to be faced is that the model is only defined in a plane. For this reason, it cannot consider the pronation-supination angle of the ankle. This may be relevant, as Sanchis-Sales et al. [90] linked such angle to the stiffness of the ankle joint.

Conclusion and Future Developments

Conclusion

This dissertation focused on enhancing the knowledge on foot-transmitted whole-body vibration. The first part described the design and development of the machine able to generate the mechanical stimulus through which investigate the human response to triaxial vibration. The machine is based on the kinematic of the linear delta robot with vertical actuators. The vertical motion of the actuators is provided by three brushless electrical motors coupled with ball screws, which are then connected to the moving platform through three custom-made preloaded cardan joints. The tests executed on the shaker prove that it can generate pseudo-random noise along the three mutually perpendicular spatial axes simultaneously, with flat spectral amplitude in the frequency range from 1 Hz to 80 Hz. Inside that frequency range, the root mean squared error between the imposed signal and the signal measured at the centre of the platform, averaged across the three axis is 6,9 mm/s^2 and 5,5 mm/s^2 for the unloaded and loaded case respectively. This proves that the machine can be used to impose a signal through which it would be possible to test the response of the human body to multiaxial mechanical vibrations.

The application of the proposed machine, however, is limited to pseudo-random noise generation, as the sinusoidal waves are affected by harmonic distortion. The resonance frequency of the machine, close to the desired working bandwidth, was at the basis of the harmonic distortion. Another proven drawback of the delta robot is the partial rotation of the moving platform, which causes cross talk between the axes. To solve these problems, it is possible to propose two corrective measures, to further develop the capabilities of the machine. The first one is the decrease of the inertia of the moving parts. The second one is the increase of the stiffness of the system. Thanks to the validated FEM model, it is possible to say that the compliance of the housing of the commercial ball screws is the main component of the overall low stiffness.

Two actions are already planned to improve the shaker performances: the first one is to replace the existing aluminium platform with a composite one; the second one is to apply strain gauges to the links of the machine to be able to directly measure the apparent mass. The expected mass of new platform is 2,4 kg, for a total mass reduction of 14,4 kg. This reduction of the inertia of the moving parts will increase both the dynamic capabilities of the machine and its bandwidth (the expected first natural frequency of the moving parts after this change is 40 Hz). The second improvement, i.e. the

application of strain gauges to the links of the robot, will enable the indirect measurements of the forces applied at the centre of the moving platform. Strain gauges (in full bridge configuration) will be applied to each link to measure the axial strain and to derive the forces in three directions; preliminary investigations have shown that the expected uncertainty is 10 N. Modifications of the geometry of the links, to increase the sensitivity of the system and reduce the uncertainty, are under evaluation.

A new method to obtain a direct mathematical link between the inverse of the conditioning number of the linear delta robot with vertical actuators and the sizes of the variables defining its kinematics was proposed. The method is based on the discretization of the space of the design variables and the direct computation of the performance index. The surfaces obtained can be then divided into contour lines. Those contour lines can be then modelled as families of curves, whose parameters are functions of the performance index itself. The results obtained can be used to obtain the region of the design space that satisfy a boundary imposed on the performance index, or to directly obtain the minimum dimensions of the robot that satisfy a given boundary on the inverse of the conditioning number. The method was implemented on a given performance index, and a given kinematic configuration; however, the same method can be extended to other indexes and configurations, if the dimensions are all consistent with each other.

The second part of the thesis focused on the development of a 2-D lumped-parameter mechanical model of the foot-ankle system. The stiffness and damping of Kelvin Voight elements have been optimized to reproduce the vibration transmissibility measured at five different locations on the foot (frequency range from 10 to 100 Hz) and the apparent mass (frequency range from 1 to 20 Hz). The modelled transmissibility fits inside the experimental variability of the measured curves. The model, therefore, can be used to estimate the effect of different corrective measures proposed to attenuate the vibration transmissibility at the extremities of the lower limbs.

Annex 1

Drafts of the custom parts produced for the Linear Delta Shaker

This annex includes the drafts of the most relevant parts that were designed and produced specifically for this application, so to make the experiments previously described repeatable. The parts were produced by Todeschini Mario s.r.l. (Via Carlo Porta 38, 23861, Cesana Brianza, LC, Italia), which also supported the drawing process.

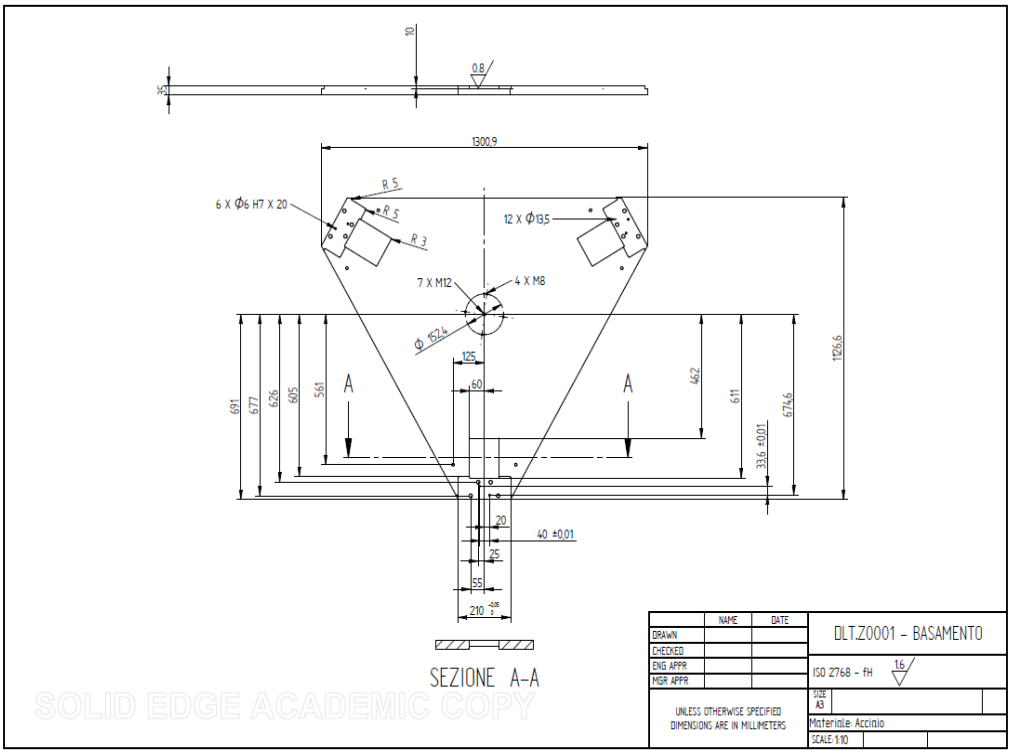

Figure A 1: draft of the base of the proposed Delta Shaker

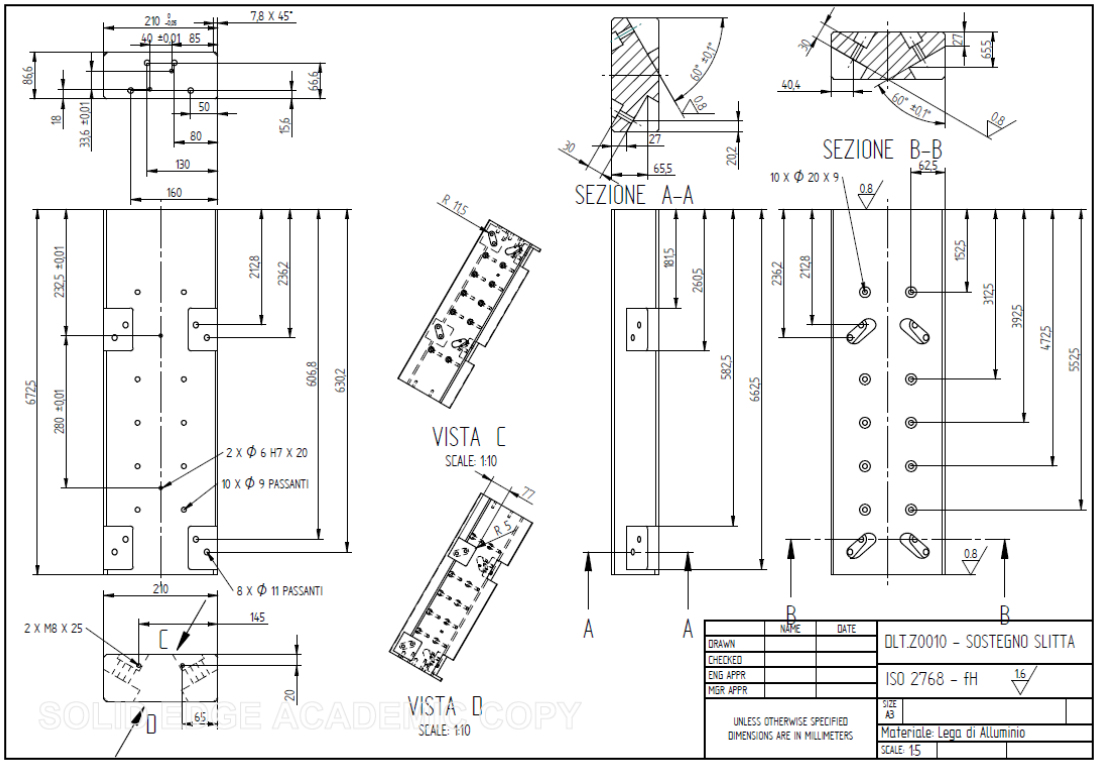

Figure A 2: Draft of the columns holding the ball screw assembly of the proposed Delta Shaker

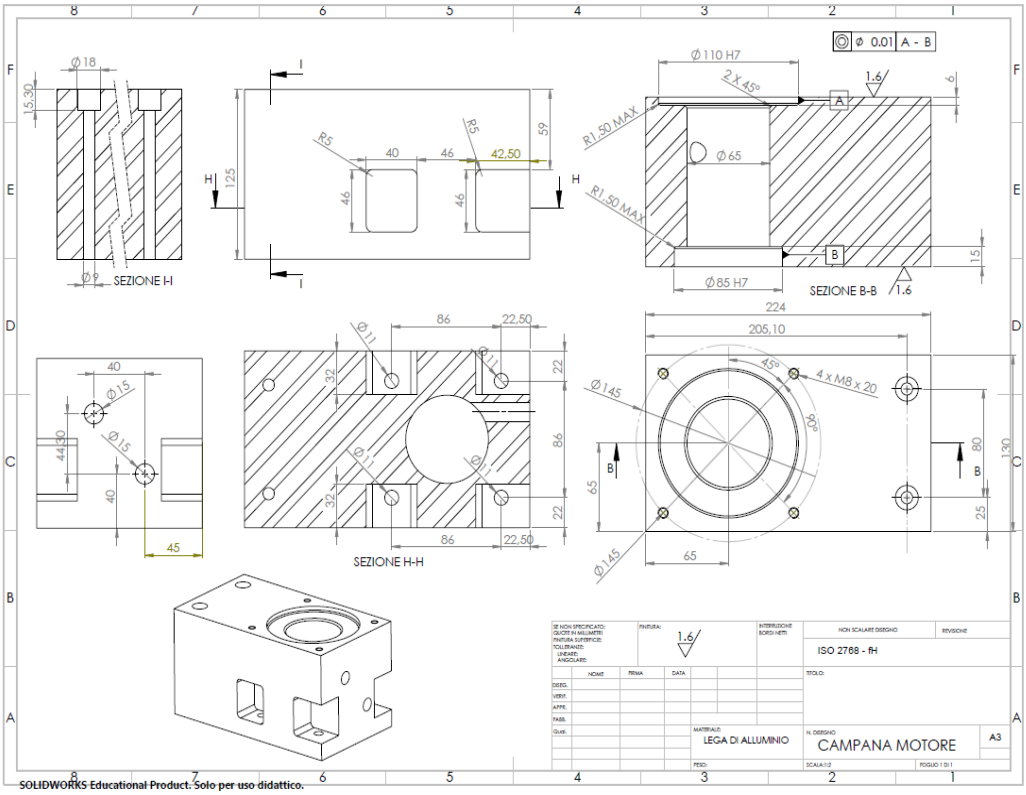

Figure A 3: Draft of the block connecting the electrical motor to the ball screw assembly of the proposed Delta Shaker

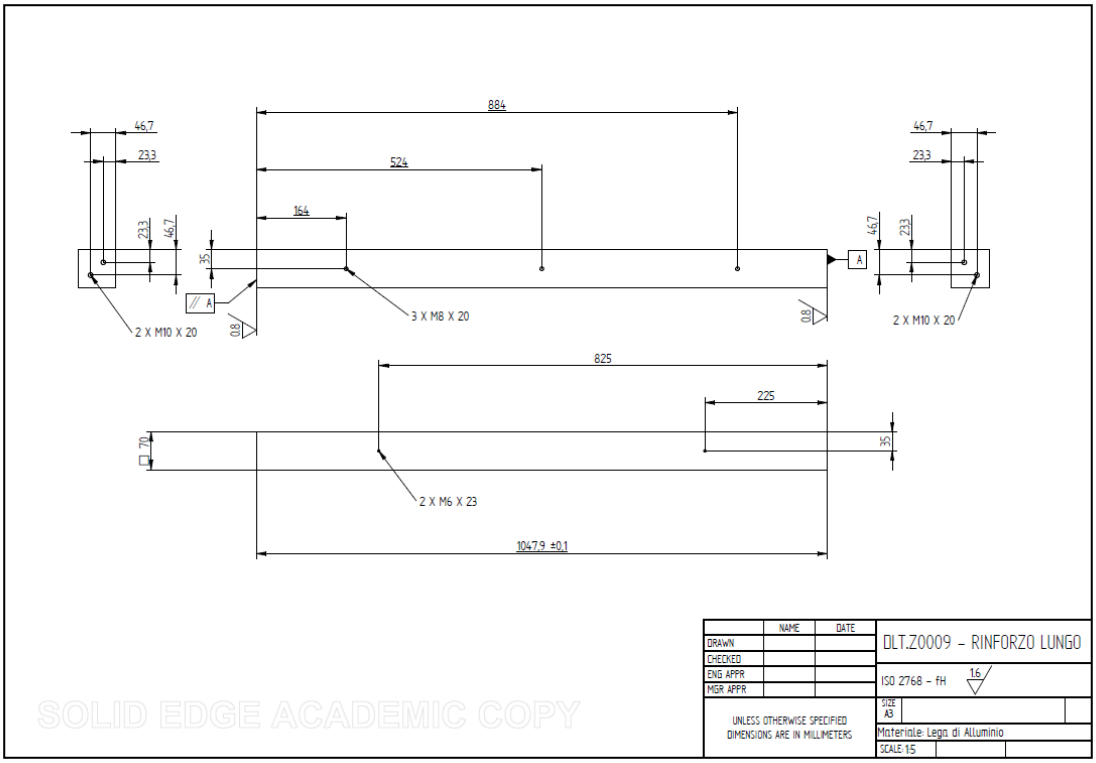

Figure A 4: Draft of the horizontal bars connecting the vertical columns of the proposed Delta Shaker

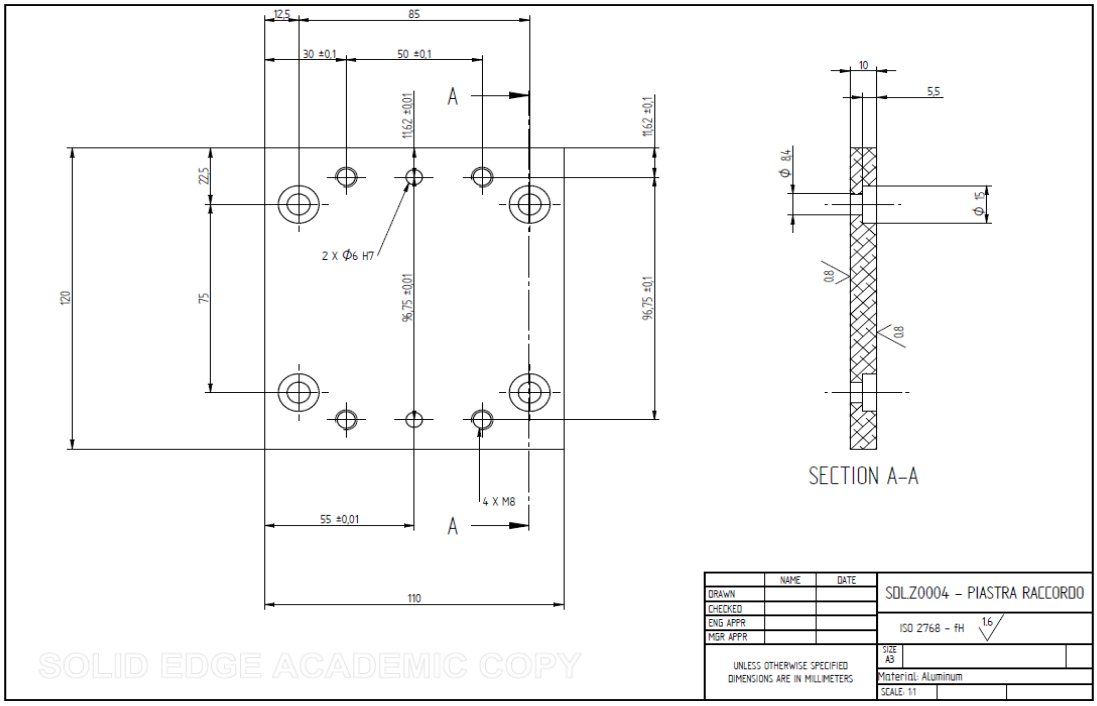

Figure A 5: Draft of the junction plate connecting the ball screws actuators to the cardan joint of the proposed Delta Shaker

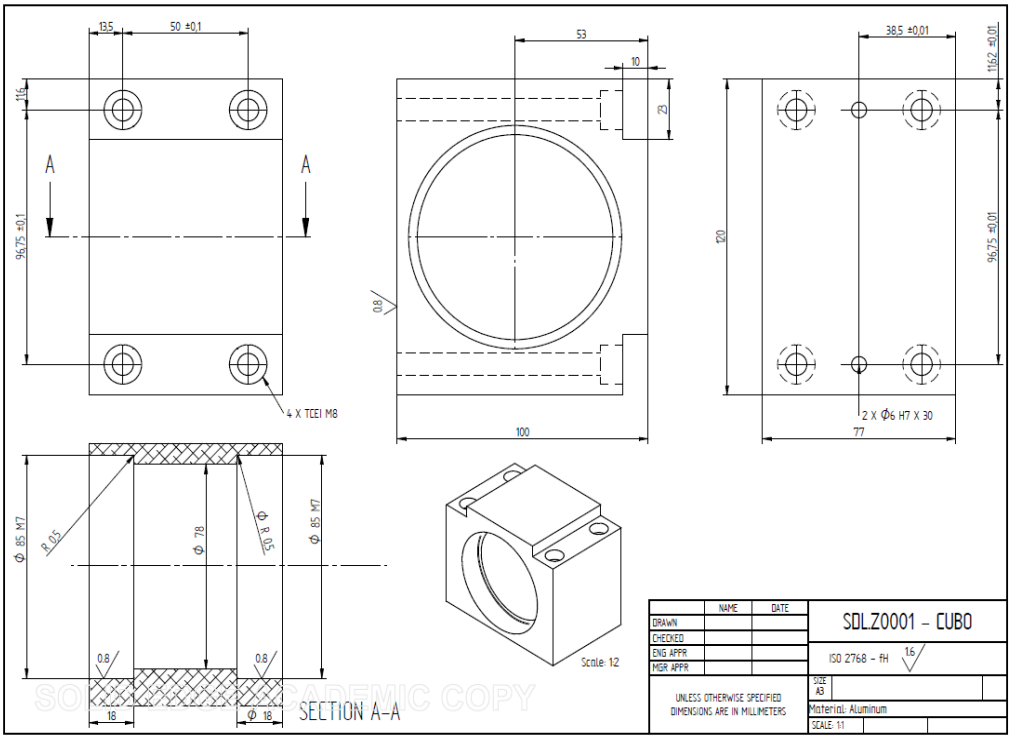

Figure A 6: Draft of the main bearings block of the cardan joint of the proposed Delta Shaker

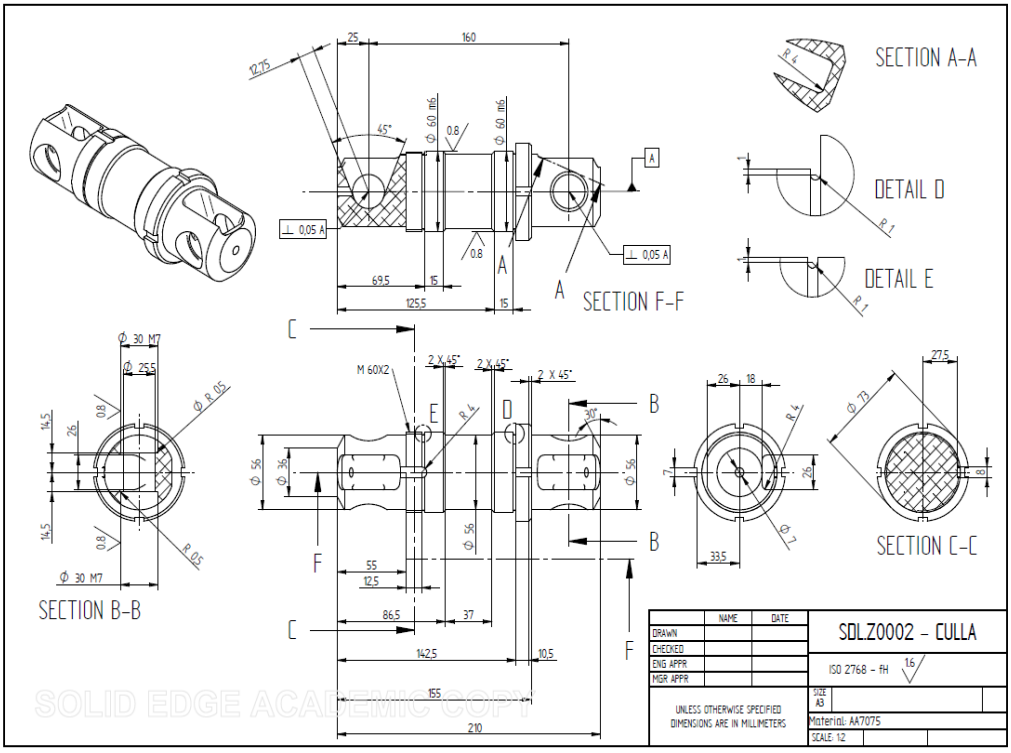

Figure A 7: Draft of the main rotating element of the cardan joint of the proposed Delta Shaker, which it is also containing the two housings for the bearings allowing the rotation of the links

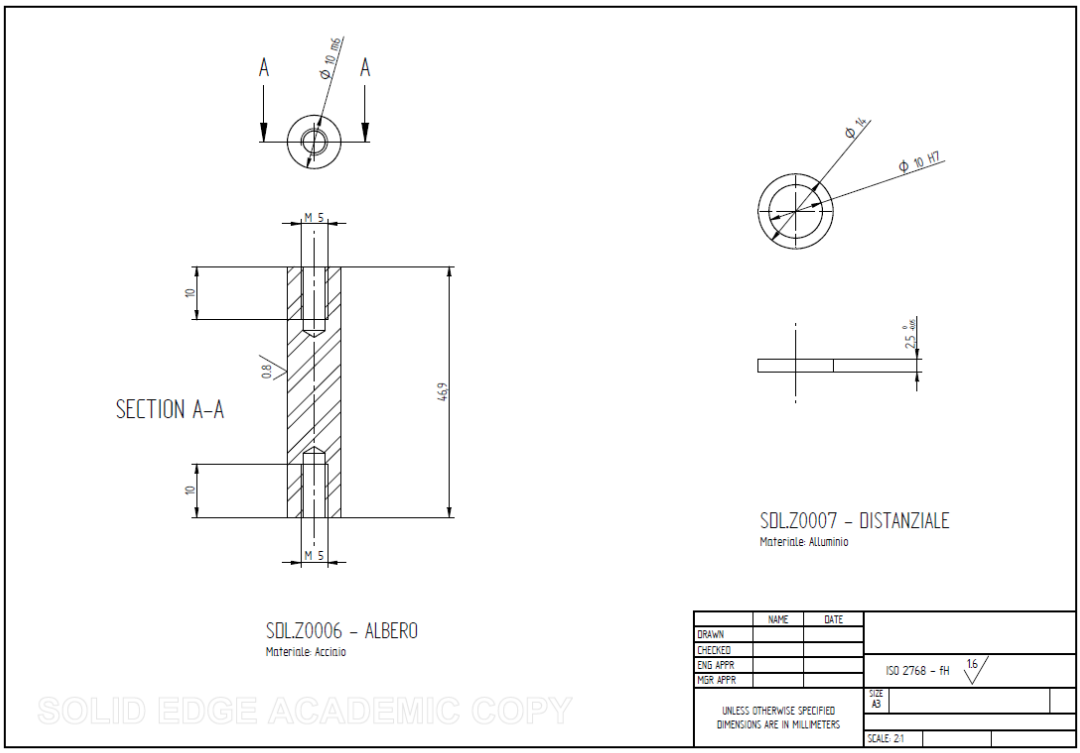

Figure A 8: Draft of the elements allowing applying a preload on the angular contact ball bearing of the links of the proposed Delta Shaker

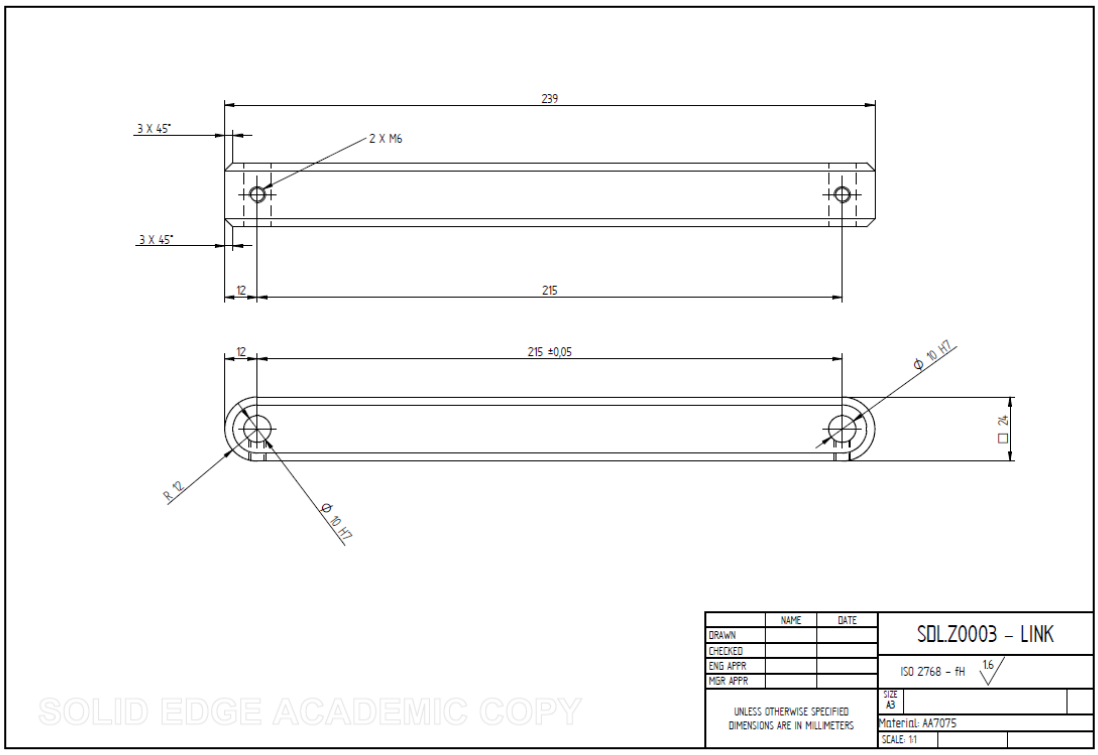

Figure A 9: Draft of the links of the proposed Delta Shaker

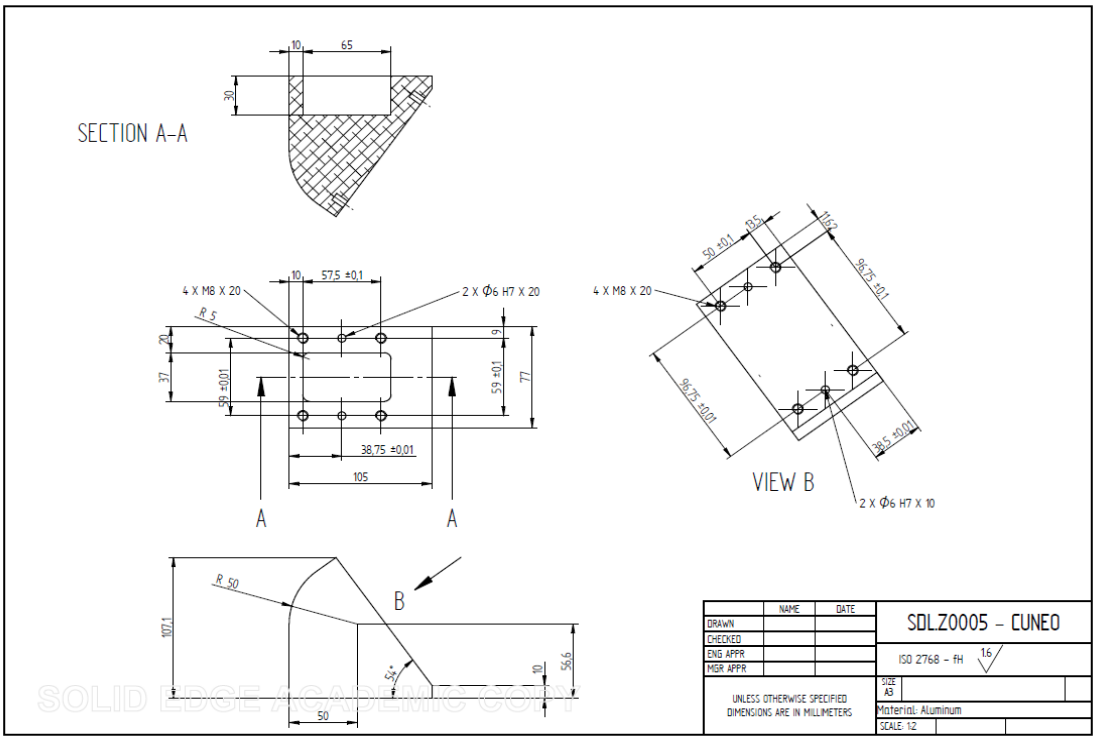

Figure A 10: draft of the elements connecting the preloaded cardan joints to the moving platform of the proposed Delta Shaker

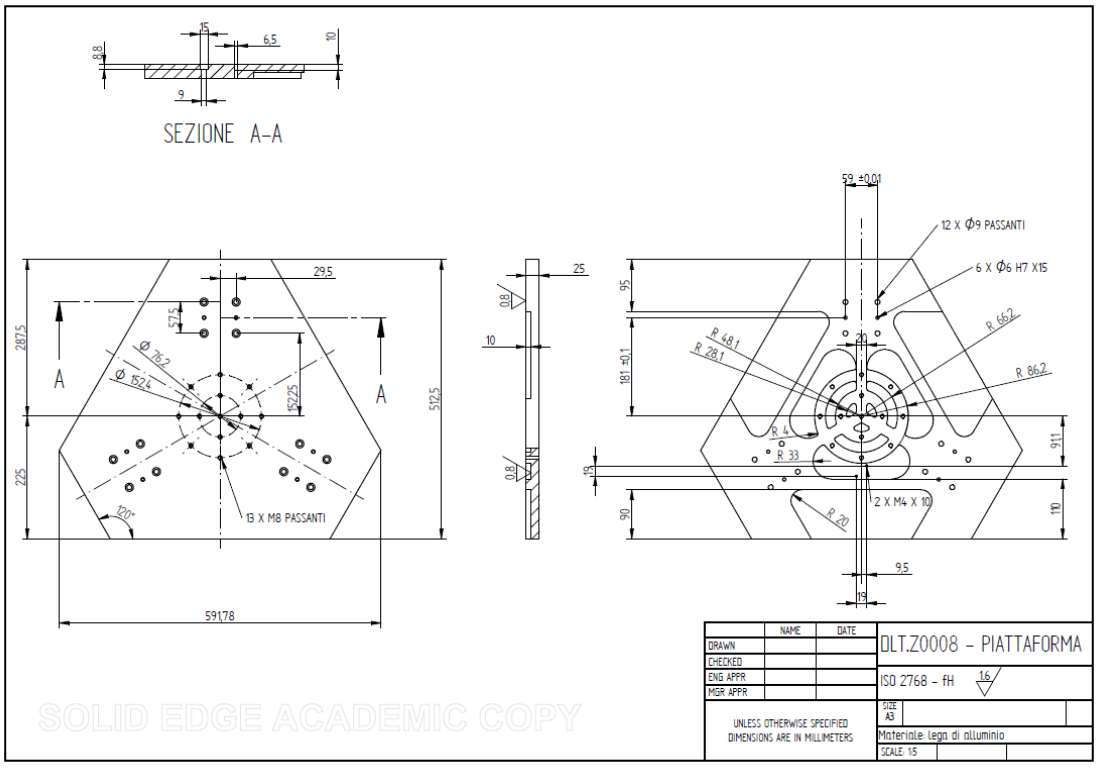

Figure A 11: draft of the moving platform of the proposed Delta Shaker

Annex 2

Equations to compute the three singular values of the Jacobian matrix of a linear delta robot with vertical actuators

This annex includes the MATLAB code through which it is possible to write the equations of the three singular values of the Jacobian matrix of a linear delta robot with vertical actuators, as explained in chapter 2.1.2.

```
clc
close all
clear

%% Variables declaration
Px = sym('Px'); %posizion of the end effector along the x
direction
Py = sym('Py'); %posizion of the end effector along the y
direction
b_s = sym('b_s'); %difference between the radius of the base
and the radius of the moving platform
l = sym('l'); %length of the link
lambda = sym('lambda'); %eigenvalues

%% Jacobian matrix assembly
J11 = (Px+b_s)/sqrt(l^2-((Px+b_s)^2+(Py)^2));
J12 = (Py)/sqrt(l^2-((Px+b_s)^2+(Py)^2));

J21 = (Px-((b_s)/2))/sqrt(l^2-((Px-
(0.5*(b_s)))^2+(Py+(sqrt(3)*0.5*(b_s)))^2));
J22 = (Py+(sqrt(3)*0.5*(b_s)))/sqrt(l^2-((Px-
(0.5*(b_s)))^2+(Py+(sqrt(3)*0.5*(b_s)))^2));

J31 = (Px-((b_s)/2))/sqrt(l^2-((Px-(0.5*(b_s)))^2+(Py-
(sqrt(3)*0.5*(b_s)))^2));
J32 = (Py-(sqrt(3)*0.5*(b_s)))/sqrt(l^2-((Px-
(0.5*(b_s)))^2+(Py-(sqrt(3)*0.5*(b_s)))^2));

J_row1 = [J11, J12, sym(1)];
J_row2 = [J21, J22, sym(1)];
J_row3 = [J31, J32, sym(1)];

J = [J_row1; J_row2; J_row3];

J_sq = J.'*J;
```

```
%% Singular values computation
J_a = J_sq-lambda*eye(3);

eigenvalues_polynomial = J_a(1,1)*(J_a(2,2)*J_a(3,3)-
J_a(3,2)*J_a(2,3))-J_a(2,1)*(J_a(1,2)*J_a(3,3)-
J_a(1,3)*J_a(3,2))+J_a(3,1)*(J_a(1,2)*J_a(2,3)-
J_a(1,3)*J_a(2,2));

coefficients = coeffs(eigenvalues_polynomial,lambda);

coefficients = coefficients/coefficients(4);

a = coefficients(4);
b = coefficients(3);
c = coefficients(2);
d = coefficients(1);

p = c - (b^2)/3;
q = 2*(b/3)^3 - (b*c)/3 + d;

%solution of the 3-rd degree polynomial
delta = (q/2)^2+(p/3)^3;

Teta = atan(sqrt((-delta))/(-q/2));

y1 = 2*sqrt(-p/3)*cos(Teta/3);
y2 = 2*sqrt(-p/3)*cos((Teta+2*pi)/3);
y3 = 2*sqrt(-p/3)*cos((Teta+4*pi)/3);

x1 = y1-b/3;
x2 = y2-b/3;
x3 = y3-b/3;

%singular valuesa
SV_ID1 = sqrt(x1);
SV_ID2 = sqrt(x2);
SV_ID3 = sqrt(x3);
```

Annex 3

Equations to compute the inverse of the inverse of the conditioning number of a planar linear delta robot with two vertical actuators

This annex includes the MATLAB code through which it is possible to write the equations of the inverse of the inverse of the conditioning number of a planar linear delta robot with two vertical actuators, as explained in chapter 2.1.2.

```
clc
close all
clear

%% Variables declaration
Px = sym('Px'); %posizion of the end effector along the x
direction
s = sym('b_s'); %half of the distance between the actuators
l = sym('l'); %length of the links
lambda = sym('lambda'); %eigenvalues

%% Jacobian matrix assembly
J11 = (Px+s)/sqrt(l^2-((Px+s)^2));
J21 = (Px-s)/sqrt(l^2-((Px-s)^2));

J_row1 = [J11, sym(1)];
J_row2 = [J21, sym(1)];

J = [J_row1; J_row2];

J_sq = J.'*J;

%% Singular values computation
J_a = J_sq-lambda*eye(2);

eigenvalues_polynomial = J_a(1,1)*J_a(2,2)-J_a(2,1)*J_a(1,2);

coefficients = coeffs(eigenvalues_polynomial,lambda);

coefficients = coefficients/coefficients(3);

a = coefficients(3);
b = coefficients(2);
c = coefficients(1);

%solution of the 2-nd degree polynomial
```

```
delta = (b)^2-4*a*c;

x1 = (-b+sqrt(delta))/(2*a);
x2 = (-b-sqrt(delta))/(2*a);

%singular values
SV_ID1 = sqrt(x1);
SV_ID2 = sqrt(x2);

%inverse of the conditioning number
ICN = SV_ID2/SV_ID1;
```

References

[1] N. Wei *et al*, "Optimal frequency/time combination of whole-body vibration training for improving muscle size and strength of people with age-related muscle loss (sarcopenia): A randomized controlled trial," *Geriatrics & Gerontology International,* vol. 17, *(10),* pp. 1412-1420, 2017.

[2] C. Bosco *et al*, "Hormonal responses to whole-body vibration in men," *Eur. J. Appl. Physiol.*, vol. 81, *(6),* pp. 449-454, 2000.

[3] M. Zago *et al*, "Whole-body vibration training in obese subjects: A systematic review," *PloS One,* vol. 13, *(9),* pp. e0202866, 2018.

[4] M. Weber-Rajek *et al*, "Whole-body vibration exercise in postmenopausal osteoporosis," *Prz Menopauzalny,* vol. 14, *(1),* pp. 41-47, Mar, 2015.

[5] D. C. Sá-Caputo *et al*, "Systematic review of whole body vibration exercises in the treatment of cerebral palsy: Brief report," *Developmental Neurorehabilitation,* vol. 19, *(5),* pp. 327-333, 2016.

[6] Y. Osawa and Y. Oguma, "Effects of combining whole-body vibration with exercise on the consequences of detraining on muscle performance in untrained adults," *The Journal of Strength & Conditioning Research,* vol. 27, *(4),* pp. 1074-1082, 2013.

[7] D. E. Adamo, B. J. Martin and P. W. Johnson, "Vibration-induced muscle fatigue, a possible contribution to musculoskeletal injury," *Eur. J. Appl. Physiol.*, vol. 88, *(1-2),* pp. 134-140, 2002.

[8] M. Bovenzi and C. Hulshof, "An updated review of epidemiologic studies on the relationship between exposure to whole-body vibration and low back pain (1986–1997)," *Int. Arch. Occup. Environ. Health,* vol. 72, *(6),* pp. 351-365, 1999.

[9] International Standards Organisation, "Evaluation of Human Exposure to Whole-body Vibration. Part 1-General Requirements. ISO2631. 1," 1997.

[10] "Directive 2002/44/EC," *Official Journal of the European Communities,* 2002.

[11] M. J. Griffin, "Minimum health and safety requirements for workers exposed to hand-transmitted vibration and whole-body vibration in the European Union; a review," *Occup. Environ. Med.*, vol. 61, *(5),* pp. 387-397, May, 2004.

[12] D. R. Smith and P. A. Leggat, "Whole-Body Vibration," *Prof. Saf.*, vol. 50, *(7),* pp. 35, 2005.

[13] M. Bovenzi, M. Schust and M. Mauro, "An overview of low back pain and occupational exposures to whole-body vibration and mechanical shocks," *Med. Lav.*, vol. 108, *(6),* pp. 419-433, 2017.

[14] L. Burström, T. Nilsson and J. Wahlström, "Whole-body vibration and the risk of low back pain and sciatica: a systematic review and meta-analysis," *Int. Arch. Occup. Environ. Health,* vol. 88, *(4),* pp. 403-418, 2015.

[15] H. Seidel, R. Bluethner and B. Hinz, "Effects of sinusoidal whole-body vibration on the lumbar spine: the stress-strain relationship," *Int. Arch. Occup. Environ. Health,* vol. 57, *(3),* pp. 207-223, 1986.

[16] L. BurstrÃ¶m, T. Nilsson and J. WahlstrÃ¶m, "Whole-body vibration and the risk of low back pain and sciatica: a systematic review and meta-analysis," *Int. Arch. Occup. Environ. Health,* vol. 88, *(4),* pp. 403-418, 2015.

[17] P. Bongers *et al*, "Back pain and exposure to whole body vibration in helicopter pilots," *Ergonomics,* vol. 33, *(8),* pp. 1007-1026, 1990.

[18] L. Clay, S. Milosavljevic and C. Trask, "Predicting whole body vibration exposure from occupational quad bike use in farmers," *Safety,* vol. 1, *(1),* pp. 71-83, 2015.

[19] X. Zeng *et al*, "Predicting whole-body vibration exposure in Canadian prairie farmers," *Annals of Work Exposures and Health,* vol. 61, *(5),* pp. 554-565, 2017.

[20] B. B. Mandal and V. D. Manwar, "Prevalence of musculoskeletal disorders among heavy earth moving machinery operators exposed to whole-body vibration in opencast mining," *International Journal of Community Medicine and Public Health,* vol. 4, *(5),* pp. 1566-1572, 2017.

[21] L. Burström *et al*, "Musculoskeletal symptoms and exposure to whole-body vibration among open-pit mine workers in the Arctic," *Int. J. Occup. Med. Environ. Health,* vol. 30, *(4),* pp. 553-564, 2017.

[22] J. Szymańska, "Dentist's hand symptoms and high-frequency vibration," *Ann. Agric. Environ. Med.,* vol. 8, pp. 7-10, 2001.

[23] M. Futatsuka *et al*, "Hand arm vibration syndrome among quarry workers in Vietnam," *Journal of Occupational Health,* vol. 47, *(2),* pp. 165-170, 2005.

[24] M. Bovenzi *et al*, "Hand-arm vibration syndrome and upper limb disorders associated with forestry work," *Med. Lav.,* vol. 95, *(4),* pp. 282-296, Jul-Aug, 2004.

[25] T. A. Su *et al*, "Hand-arm vibration syndrome among a group of construction workers in Malaysia," *Occup. Environ. Med.,* vol. 68, *(1),* pp. 58-63, Jan, 2011.

[26] B. Noel, "Pathophysiology and classification of the vibration white finger," *Journal of the Peripheral Nervous System,* vol. 5, *(4),* pp. 242-242, 2000.

[27] A. J. Brammer, W. Taylor and G. Lundborg, "Sensorineural stages of the hand-arm vibration syndrome," *Scand. J. Work Environ. Health,* pp. 279-283, 1987.

[28] M. Bovenzi, "Exposure-response relationship in the hand-arm vibration syndrome: an overview of current epidemiology research," *Int. Arch. Occup. Environ. Health,* vol. 71, *(8),* pp. 509-519, 1998.

[29] T. Nilsson, J. Wahlstrom and L. Burstrom, "Hand-arm vibration and the risk of vascular and neurological diseases-A systematic review and meta-analysis," *PLoS One,* vol. 12, *(7),* pp. e0180795, Jul 13, 2017.

[30] International Standards Organisation, "Mechanical vibration - Measurement and evaluation of human exposure to hand-transmitted vibration - Part 1: General requirements (ISO 5349-1:2001)," 2001.

[31] Y. Tominaga, "New frequency weighting of hand-arm vibration," *Ind. Health,* vol. 43, *(3),* pp. 509-515, 2005.

[32] A. Thompson *et al*, "Vibration-white foot: a case report," *Occupational Medicine*, vol. 60, *(7)*, pp. 572-574, 2010.

[33] M. Leduc *et al*, "Examination of vibration characteristics, and reported musculoskeletal discomfort for workers exposed to vibration via the feet," *Journal of Low Frequency Noise, Vibration and Active Control*, vol. 30, *(3)*, pp. 197-206, 2011.

[34] T. Eger *et al*, "Vibration induced white-feet: overview and field study of vibration exposure and reported symptoms in workers," *Work*, vol. 47, *(1)*, pp. 101-110, 2014.

[35] A. A. Nikooyan and A. A. Zadpoor, "Mass–spring–damper modelling of the human body to study running and hopping–an overview," *Proc. Inst. Mech. Eng. Part H J. Eng. Med.*, vol. 225, *(12)*, pp. 1121-1135, 2011.

[36] A. A. Zadpoor and A. A. Nikooyan, "Modeling muscle activity to study the effects of footwear on the impact forces and vibrations of the human body during running," *J. Biomech.*, vol. 43, *(2)*, pp. 186-193, 2010.

[37] J. Z. Wu *et al*, "Finite element analysis of the penetrations of shear and normal vibrations into the soft tissues in a fingertip," *Med. Eng. Phys.*, vol. 29, *(6)*, pp. 718-727, 2007.

[38] S. P. Pattnaik, *Development of Analytical Models to Study Musculoskeletal and Vascular Damage Leading to Hand-Arm Vibration Syndrome*, 2011.

[39] Y. Hua, P. Lemerle and J. Ganghoffer, "A two scale modeling and computational framework for vibration-induced Raynaud syndrome," *Journal of the Mechanical Behavior of Biomedical Materials*, vol. 71, pp. 320-328, 2017.

[40] C. Noël, "A three-dimensional visco-hyperelastic FE model for simulating the mechanical dynamic response of preloaded phalanges," *Med. Eng. Phys.*, vol. 61, pp. 41-50, 2018.

[41] Y. Matsumoto and M. Griffin, "Mathematical models for the apparent masses of standing subjects exposed to vertical whole-body vibration," *J. Sound Vibrat.*, vol. 260, *(3)*, pp. 431-451, 2003.

[42] N. Nawayseh and M. J. Griffin, "A model of the vertical apparent mass and the fore-and-aft cross-axis apparent mass of the human body during vertical whole-body vibration," *J. Sound Vibrat.*, vol. 319, *(1-2)*, pp. 719-730, 2009.

[43] G. Subashi, Y. Matsumoto and M. Griffin, "Modelling resonances of the standing body exposed to vertical whole-body vibration: Effects of posture," *J. Sound Vibrat.*, vol. 317, *(1-2)*, pp. 400-418, 2008.

[44] W. Abbas *et al*, "Optimal seat and suspension design for a half-car with driver model using genetic algorithm," *Intelligent Control and Automation*, vol. 4, *(02)*, pp. 199, 2013.

[45] M. S. Nagamani, S. S. Rao and S. Adinarayana, "Minimization of human body responses due to automobile vibrations in quarter car and half car models using PID controller," *SSRG International Journal of Mechanical Engineering (SSRG-IJME)*, 2017.

[46] P. Marcotte, J. Boutin and J. Jasinski, "Development of a hand–arm mechanical analogue for evaluating chipping hammer vibration emission values," *J. Sound Vibrat.*, vol. 329, *(10)*, pp. 1968-1980, 2010.

[47] Z. Yue and J. Mester, "A model analysis of internal loads, energetics, and effects of wobbling mass during the whole-body vibration," *J. Biomech.*, vol. 35, *(5)*, pp. 639-647, 2002.

[48] M. Fritz, "An improved biomechanical model for simulating the strain of the hand-arm system under vibration stress," *J. Biomech.*, vol. 24, *(12)*, pp. 1165-1171, 1991.

[49] P. Boileau, S. Rakheja and X. Wu, "A body mass dependent mechanical impedance model for applications in vibration seat testing," *J. Sound Vibrat.*, vol. 253, *(1)*, pp. 243-264, 2002.

[50] W. Liu and B. M. Nigg, "A mechanical model to determine the influence of masses and mass distribution on the impact force during running," *J. Biomech.*, vol. 33, *(2)*, pp. 219-224, 2000.

[51] A. Simkin and I. Leichter, "Role of the calcaneal inclination in the energy storage capacity of the human foot—a biomechanical model," *Medical and Biological Engineering and Computing*, vol. 28, *(2)*, pp. 149-152, 1990.

[52] R. Ker *et al*, "The spring in the arch of the human foot," *Nature*, vol. 325, *(6100)*, pp. 147, 1987.

[53] A. Gefen, "The in vivo elastic properties of the plantar fascia during the contact phase of walking," *Foot & Ankle International*, vol. 24, *(3)*, pp. 238-244, 2003.

[54] W. Kim and A. S. Voloshin, "Role of plantar fascia in the load bearing capacity of the human foot," *J. Biomech.*, vol. 28, *(9)*, pp. 1025-1033, 1995.

[55] N. Mansfield, "Impedance methods for assessment of the biomechanical response of the seated person to whole-body vibration," *Ind. Health*, vol. 43, pp. 378-389, 2005.

[56] N. Nawayseh and M. Griffin, "Non-linear dual-axis biodynamic response to vertical whole-body vibration," *J. Sound Vibrat.*, vol. 268, *(3)*, pp. 503-523, 2003.

[57] M. Tarabini *et al*, "Setup for the measurement of apparent mass matrix of standing subjects," *IEEE Transactions on Instrumentation and Measurement*, vol. 65, *(8)*, pp. 1856-1864, 2016.

[58] Z. Pandilov and V. Dukovski, "COMPARISON OF THE CHARACTERISTICS BETWEEN SERIAL AND PARALLEL ROBOTS." *Acta Technica Corvininesis-Bulletin of Engineering*, vol. 7, *(1)*, 2014.

[59] J. Merlet, "Parallel manipulators: state of the art and perspectives," *Adv. Rob.*, vol. 8, *(6)*, pp. 589-596, 1993.

[60] Y. Patel and P. George, "Parallel manipulators applications—a survey," *Modern Mechanical Engineering*, vol. 2, *(03)*, pp. 57, 2012.

[61] Y. Wan *et al*, "A survey on the parallel robot optimization," in *2008 Second International Symposium on Intelligent Information Technology Application*, 2008, pp. 655-659.

[62] R. E. Stamper, L. Tsai and G. C. Walsh, "Optimization of a three DOF translational platform for well-conditioned workspace," in *Proceedings of International Conference on Robotics and Automation*, 1997, pp. 3250-3255.

[63] X. Liu *et al*, "A New Approach to the Design of a DELTA Robot with a Desired Workspace," *Journal of Intelligent and Robotic Systems*, vol. 39, *(2)*, pp. 209-225, 2004.

[64] K. C. Olds, "Global indices for kinematic and force transmission performance in parallel robots," *IEEE Transactions on Robotics*, vol. 31, *(2)*, pp. 494-500, 2015.

[65] E. Courteille, D. Deblaise and P. Maurine, "Design optimization of a delta-like parallel robot through global stiffness performance evaluation," in *2009 IEEE/RSJ International Conference on Intelligent Robots and Systems*, 2009, pp. 5159-5166.

[66] H. Giberti, L. Sbaglia and M. Silvestri, "Mechatronic design for an extrusion-based additive manufacturing machine," *Machines*, vol. 5, *(4)*, pp. 29, 2017.

[67] M. Stock and K. Miller, "Optimal kinematic design of spatial parallel manipulators: application to linear delta robot," *Journal of Mechanical Design*, vol. 125, *(2)*, pp. 292-301, 2003.

[68] R. Clavel, "A fast robot with parallel geometry," in *Proc. Int. Symposium on Industrial Robots*, 1988, pp. 91-100.

[69] R. Clavel, *Device for the Movement and Positioning of an Element in Space*, 1990.

[70] M. Bouri and R. Clavel, "The linear delta: Developments and applications," in *Robotics (ISR), 2010 41st International Symposium on and 2010 6th German Conference on Robotics (ROBOTIK)*, 2010, pp. 1-8.

[71] P. Marzaroli *et al*, "Design and Testing of a 3-DOF Robot for Studying the Human Response to Vibration," *Machines*, vol. 7, *(4)*, pp. 67, 2019.

[72] H. Giberti, S. Cinquemani and G. Legnani, "Effetti delle caratteristiche meccaniche della trasmissione sulla scelta del motoriduttore," in *XIX Congresso dell'Associazione Italiana Di Meccanica Teorica E Applicata (AIMETA 2009)*, 2009, pp. 1-9.

[73] J. Merlet, "Jacobian, manipulability, condition number, and accuracy of parallel robots," *Journal of Mechanical Design*, vol. 128, *(1)*, pp. 199-206, 2006.

[74] M. Tarabini *et al*, "Apparent mass matrix of standing subjects exposed to multi-axial whole-body vibration," *Ergonomics*, vol. 59, *(8)*, pp. 1038-1049, 2016.

[75] H. Giberti, S. Cinquemani and G. Legnani, "Effects of transmission mechanical characteristics on the choice of a motor-reducer," *Mechatronics*, vol. 20, *(5)*, pp. 604-610, 2010.

[76] M. ELGEZIRY, "Modelling the dynamic behaviour of 3D shakers for testing the human response to vibration," 2018.

[77] A. ALBANETTI LUCIANO, "Model and test of a 3-DOF shaker for the study of human response to multiaxial vibrations," 2018.

[78] M. Pastor, M. Binda and T. Harčarik, "Modal assurance criterion," *Procedia Engineering*, vol. 48, pp. 543-548, 2012.

[79] A. Presas *et al*, "Accurate determination of the frequency response function of submerged and confined structures by using PZT-patches," *Sensors*, vol. 17, *(3)*, pp. 660, 2017.

[80] ALBERTO FONTANIERI, "Lightweight Optimization of a Multiaxial Shaker and Design of a Force Measurement System for the Apparent Mass Evaluation." , Italy, 2019.

[81] K. A. Goggins *et al*, "Biomechanical response of the human foot when standing in a natural position while exposed to vertical vibration from 10–200 Hz," *Ergonomics*, vol. 62, *(5)*, pp. 644-656, 2019.

[82] M. Tarabini *et al*, "Apparent mass distribution at the feet of standing subjects exposed to whole-body vibration," *Ergonomics*, vol. 56, *(5)*, pp. 842-855, 2013.

[83] D. Chadefaux *et al*, "Development of a two-dimensional dynamic model of the foot-ankle system exposed to vibration," *J. Biomech.*, pp. 109547, 2019.

[84] R. E. Isman, V. T. Inman and P. Poor, "Anthropometric studies of the human foot and ankle," *Bull. Prosthet. Res.*, vol. 11, *(97)*, pp. 129, 1969.

[85] Y. Lee, G. Lin and M. J. Wang, "Evaluating gender differences in foot dimensions," *For A Ll*, 2011.

[86] V. M. Zatsiorsky and V. M. Zaciorskij, *Kinetics of Human Motion.* Human Kinetics, 2002.

[87] M. Tarabini *et al*, "Analysis of non-linear response of the human body to vertical whole-body vibration," *Ergonomics*, vol. 57, *(11)*, pp. 1711-1723, 2014.

[88] S. MAUGERI, "Modelling the response of the human feet to vertical whole-body vibration," 2019.

[89] R. Lundström, *Vibration Exposure of the Glabrous Skin of the Human Hand*, 1985.

[90] E. Sanchis-Sales *et al*, "Effect of static foot posture on the dynamic stiffness of foot joints during walking," *Gait Posture*, vol. 62, pp. 241-246, 2018.